p. 123

AN ANALYTICAL AND EXPERIMENTAL STUDY TO INVESTIGATE FLUTTER SUPPRESSION VIA PIEZOELECTRIC ACTUATION

JENNIFER HEEG

A Thesis Submitted to the School of Engineering and Applied Science of the George Washington University in Partial Fulfillment of the Requirements for the Degree of Master of Science August 1991 Thesis Directed by Vladislav Klein Professor of Engineering and Applied Science.

Table of Contents

ABSTRACT

The objective of this research was to analytically and experimentally study the capabilities of adaptive material plate actuators for suppressing flutter. The validity of analytical modeling techniques for piezoelectric materials was also to be investigated. Piezoelectrics are materials which are characterized by their ability to produce voltage when subjected to a mechanical strain. The converse piezoelectric effect can be utilized to actuate a structure by applying a voltage. For this investigation, a two degree of freedom wind tunnel model was designed, analyzed and tested. The model consisted of a rigid airfoil and a flexible mount system which permitted a translational and a rotational degree of freedom. It was designed such that flutter was encountered within the testing envelope of the wind tunnel. Actuators, made of piezoelectric material were afixed to leaf springs of the mount system. Each degree of freedom was controlled by a separate leaf spring. Command signals, applied to the piezoelectric actuators, exerted control over the damping and stiffness properties. A mathematical aeroservoelastic model was constructed using finite element methods, laminated plate theory, and aeroelastic analysis tools. Plant characteristics were determined from this model and verified by open loop experimental tests. A flutter suppression control law was designed and implemented on a digital control computer. Closed loop flutter testing was conducted. The experimental results represent the first time that adaptive materials have been used to actively suppress flutter. It demonstrates that small, carefully-placed actuating plates can be used effectively to control aeroelastic response.

ACKNOWLEDGEMENTS

The author wishes to acknowledge the many individuals who have made this work possible. The list is extensive due to the many systems required to make an experiment work and the many facets of an aeroservoelastic analysis which must be investigated for a successful model to be developed. Fortunately, this project was undertaken without the realization that so many things would have to be worked out. There were so many show stoppers along the way that to have been able to compile a list at the beginning, with no knowledge of how to solve any of them, they might have been enough to discourage me altogether. I wish to begin by acknowledging the support and confidence of Dr. Tom Noll. Without his encouragement, this effort would not have culminated in success.

The following people helped to make this work possible. I won't regale you with their specific contributions. I just want them to know that I appreciate their help. For their technical advice, support, and handiwork, I wish to thank

Kenneth Dudley
Wayne Matthews
Richard Young
Renee Lake
H. Jack Dunn
Robert Scott
Jay Moen
M.E. Hales
Richard Macauley
Jer-Nan Juang
Thomas Zeiler
Bob Miserentino
Woodrow Whitlow
Michael Gilbert
Boyd Perry, III
Roger Amick
Rex Meadors
Chuck McLish
Sylvie Lefebvre
Vern Metcalf
Bob Doggett
Michele Malenfant
Mike Riley
Tony Pototzky
Sheri Hoadley
Janice Bayer
Tom Moore
Professor Terrence A. Weisshaar
David Rosser

and the rest of the ASEB and SDyD people at NASA Langley who were of immense help throughout this project.

For their general support, interest, and help in making *Flutter Suppression: the Movie*, I wish to thank Karen E. Fischer and Randolph H. Cabell.

LIST OF FIGURES

LIST OF TABLES

LIST OF SYMBOLS

c .....Chord

d_{31} .....Electromechanical coupling coefficient, in-plane response to voltage in poled direction

d_{32} .....Electromechanical coupling coefficient, in-plane response to voltage in poled direction

d_{33} .....Electromechanical coupling coefficient, response in the direction of applied voltage corresponding to the poling axis

d_{15} .....Electromechanical coupling coefficient, shearing response to voltage applied perpendicular to the poling axis

f .....Natural frequency in cycles per second (Hertz)

k .....Stiffness of a single degree of freedom

m .....Mass

m_0 .....Mass per unit area

n .....Number of elapsed cycles

$\bar{q}$ .....Dynamic Pressure

q_{xi}, q_{yi}, q_{zi} .....Generalized coordinates corresponding to mode shape displacement vectors in the x,y, and z directions, respectively

s .....Laplace variable

t .....Thickness of the piezoelectric plate

t .....Time

u .....Control vector in the state space equations

v .....Velocity

u, v, w .....Component displacements in the x,y, and z directions respectively

x, y, z .....Component directions

x_0, y_0, z_0 .....Location of the 0th point within the x,y,z frame

x_1 .....Amplitude of the first cycle

x_n .....Amplitude of the nth cycle

z .....Distance from the midplane to a point on the structure

$\bar{z}$ .....Distance from the midplane of the plunge spring tine to the bonded face of the piezoelectric plate

A .....Area

E .....Young's modulus

E .....Applied voltage per thickness

F_1 .....Term arising from potential energy, defined in equation

F_2 .....Term arising from potential energy, defined in equation, strain actuator term

F_3 .....Term arising from kinetic energy, defined in equation

G.F. .....Gage factor
G_{12} .....Shear modulus
I_{yy} .....Inertia about the pitch axis
R .....Electric flux density
R .....Transfer function
T .....Kinetic energy
U .....Potential energy
v .....Applied voltage
v_{max} .....Maximum voltage which may be applied to the actuator

β .....Scale factor for combining the aerodynamic and structural control modes
γ .....Piezoelectric actuation constant
γ_{xy} .....Shear strain in the x-y plane
δ .....Logarithmic decrement
ε .....Strain vector
ε_{xx} .....Normal strain in the x-direction
ε_{yy} .....Normal strain in the y-direction
κ .....Curvature
λ .....Eigenvalue
ν .....Poisson's ratio
ρ .....Destiny
σ .....Stress vector
σ_x .....Normal stress in the x-direction
σ_y .....Normal stress in the y-direction
τ_{xy} .....Shear stress in the x-y plane
ζ .....Damping ratio
ω .....Natural frequency

Matrices / Vectors

A .....State matrix
A .....Extensional stiffness matrix
$[\hat{A}_0]$ .....Constant terms of the rational function approximation to the generalized aerodynamic forces
$[\hat{A}_1]$ .....Coefficients of the first derivative terms of the rational function approximation to the generalized aerodynamic forces

$[\hat{A}_2]$ .....Coefficients of the second derivative terms of the rational function approximation to the generalized aerodynamic forces

B .....State space control matrix

B .....Coupling stiffness matrix

D .....Generalized damping matrix

D .....Bending stiffness matrix

[d] .....Electromechanical coupling matrix

[G] .....Stiffness matrix

K .....Generalized stiffness matrix

M .....Generalized mass matrix

$\mathbf{M}_\Lambda$ .....Moment due to strain actuation

$\mathbf{N}_\Lambda$ .....Force due to strain actuation

Q .....Generalized forces due to the aerodynamics

$\hat{Q}$ .....Rational function approximations to the aerodynamic generalized forces

[S] .....Compliance matrix

$\{u\}$ .....Displacement vector with components u, v, and w

u .....Control vector

x_{f1}, x_{f2} .....States associated with the flexible modes and their derivatives

x .....State vector

y .....Output vector

$[\beta]$ .....Permittivity matrix

ε .....Strain vector

$[\in]$ .....Impermittivity matrix

σ .....Stress vector

Γ .....Actuating matrix

Φ_{uu} .....Autospectrum of input

Φ_{uy} .....Cross-spectrum of input with output

$\Psi_{xi}, \Psi_{yi}, \Psi_{zi}$ .....Mode shape displacement vectors for node point i in the x, y, and z directions, respectively

$[\Psi]$ .....Mode shape displacement matrix

Subscripts

a .....Associated with the aerodynamics

f .....Associated with the flexible modes

i,j .....Denote the ith and jth node point, mode, or element

p .....Associated with the controls or piezoelectrics

pl .....Associated with the plunge degree of freedom
s .....Associated with the structure
x, y, and z
.....Denote quantities in the x-, y-, and z-directions, respectively
L, M and N
.....Denote the limits in the x-, y- and z-directions, respectively
θ .....Associated with the pitching degree of freedom
Λ .....Associated with the strain actuation
0 .....Associated with the midplane
1, 2, 3...
.....Used in association with the electromechanical coupling coefficients,
Otherwise used to denote mode shapes, potential and kinetic energy factors, state vectors, etc.

Operators, etc

dA .....Dummy variable of integration over the area
dV .....Dummy variable of integration over the volume
D , $[D]$
.....Derivative operator matrix
$[]^T$ .....Transpose
~ .....Placed over a matrix, denotes that both the structural and aerodynamic effects are included
^ .....Placed over the aerodynamic matrices to indicate that a rational function approximation has been made
– .....Placed over a matrix, denotes that it is the physical matrix and not the generalized one (i.e. It has not yet been pre and post multiplied by the mode shapes)
$\dot{}$
.....Derivation with respect to time

CHAPTER 1 INTRODUCTION

Flutter, a dynamic interaction between the structure and the aerodynamics which results in divergent and destructive oscillations of motion, has been observed and documented on aircraft since the era of controlled flight began.[1.1] Historically, passive approaches such as increasing structural stiffness, mass balancing or modifying geometry have been utilized to suppress this hazardous phenomenon. These solutions result in increased cost and decreased performance. During the past twenty years, there has been considerable research to develop active flutter suppression concepts which use conventional leading and trailing edge aerodynamic control surfaces.[1.1, 1.2, 1.3, 1.4, 1.5] Active flutter suppression is not a common practice in today's aerospace industry or military due to several concerns. Because of the catastrophic nature of flutter, a failure of the system could affect flight safety. Therefore system redundancy, reliability and maintainability are critical issues to be addressed. To a lesser extent, the control surface authority available to maneuver the aircraft with the simultaneous implementation of active flutter suppression is also a concern. To alleviate these concerns, alternatives to utilizing the aerodynamic control surfaces for active flutter suppression are being studied.

The use of secondary controllers made of adaptive material is one such concept. There are several classifications of adaptive materials including piezoelectrics, electrostrictors, shape memory alloys, and magnetostrictors. A detailed account of the properties, benefits and

drawbacks of each type can be found in Reference 1.6. This study focused exclusively on the use of piezoelectric materials, which were chosen based on their favorably wide control bandwidth, favorable material properties and the availability of results from past investigations using these materials. Piezoelectricity is the ability of a material to develop an electrical charge when subjected to a mechanical strain. The converse piezoelectric effect, simply the development of mechanical strain when subjected to an electrical field, can be utilized to actuate a structure. A local strain is produced in the structure which induces forces and moments. By judicious arrangement of piezoelectric plates, the correct reaction of the structure required to inhibit flutter can be produced. Many recent research efforts have utilized adaptive plate actuators for various applications[1.6 through 1.17] and just recently for flutter suppression.[1.8]

Results available from aeroelastic applications of piezoceramics are very limited. Static aeroelasticity has been the subject of investigations by Ehlers and Weisshaar.[1.6, 1.15, 1.16] They conducted analytical studies on laminated composite wings with embedded actuators, looking at pure torsional, and bending deformations. They reported that through feedback to embedded adaptive material layers, the divergence speed is altered, implying also that lift effectiveness is influenced. The augmentation or replacement of conventional aerodynamic control surfaces with strain actuation for aeroelastic control has been the focus of an analytical investigation of a typical section by Lazarus, Crawley and Lin.[1.17] They found that strain actuation via piezoelectric elements may provide a viable and effective alternative to articulated control surfaces for controlling aeroelastic response. Investigation of flutter suppression for lifting surfaces has been done by Scott.[1.8] This analytical study looked at high speeds and low aspect ratio wings. Full state feedback was employed to control chordwise bending.

The purpose of this work was to investigate flutter suppression using piezoelectric plates as actuators. Analyses and experiments which demonstrate this capability will be presented. Based on preliminary analyses and an understanding of the actuating mechanisms involved, a rigid wing wind tunnel model and flexible mount system were designed for use in this investigation. Chapter 2 presents a background on piezoelectric materials, some previously-examined actuating applications and analysis used in the design of the test article. The content of Chapter 3 familiarizes the reader with the details of the test article and the experimental test set up. Additionally, the wind tunnel facility, instrumentation, and control computer are discussed. In Chapter 4, the detailed development of the aeroservoelastic equations of motion is presented. The theoretical equations are first derived, followed by the methods of implementation. Active flutter suppression requires design of a control law which will favorably alter the aeroelastic response. To design a control law, the characteristics of the uncontrolled or open loop system must first be investigated. Chapter 5 presents the results of analytical studies based on the open loop aeroservoelastic equations, the design of the control law, and results from closed loop studies. Chapter 6 presents experimental results and compares them with the analytical predictions. System identification test results are discussed as well as the open and closed loop flutter results.

CHAPTER 2 PIEZOELECTRIC MATERIALS & TEST ARTICLE DESIGN

2.1 PIEZOELECTRIC MATERIALS

A material which, when subjected to a mechanical load, accumulates an electric charge is said to have piezoelectric properties. Conversely, the material, when subjected to an applied electrical field will induce strain. The polarity of the applied electrical field determines whether the strain is compressive or tensile. There are crystals, polymers and ceramics which have been invented or discovered which exhibit piezoelectric characteristics. Ferroelectric materials, a subcategory of piezoelectrics, can be produced from certain types of ceramics and polymers by applying a large electrical field across them. This induces an orientation of the ions such that the positive and negative poles of the individual ions are aligned with the applied field, denoted the 3-direction.

There are many natural crystalline substances, quartz among them, which exhibit piezoelectric characteristics. Applications of such crystals date to pre-World War I when they were used for depth sounding.[2.1] The discovery of these crystals spawned investigations into manufacturing materials which would produce electromechanical coupling. Polymers and ceramics are the two modern materials which are used.

Polymers have low stiffness (Young's modulus) properties. Thus, they tend to be very flexible and well-suited for sensor applications. Ceramics have higher stiffness properties and are well-suited for actuator applications. However, ceramics tend to be very brittle and this fragility is one drawback which must be addressed before they could be used in

beyond-research applications. Lead Zirconate Titinate (PZT), a piezoceramic, was chosen for this investigation. PZT material properties are detailed in Reference 2.2.

The poling process of ferroelectric materials reorients the dipoles such that there is a net polarization along the axis of applied voltage, denoted the 3-direction. The orientation remains after the inducing field is removed. Using these materials requires a voltage to be subsequently applied through electrodes on opposite faces of the material. The most common configuration, (figure 2.1), is to place the electrodes on the faces parallel to the poled axis and to apply the voltage in the same direction as the original inducing field. The material deforms both through the thickness, denoted the d33 effect, (figure 2.2), and in in-plane directions, denoted the d31 or d32 effect, (figure 2.3). Applying a voltage field oriented in one direction induces in-plane expansion; applying it in the other direction induces in-plane contraction. To define the electromechanical effects, the first subscript denotes the direction of the applied voltage and the second subscript denotes the direction of the deformation. Due to transverse isotropy, there is no distinction between vectors lying in any plane perpendicular to the poling axis for PZT. To complete the description of the deformations achievable with this material, figure 2.4 shows the electrodes placed on faces parallel to the poling axis (i.e. in the 1-direction). This induces a shearing strain within the piezoelectric, as the positively poled side of the piezoceramic strains toward the negatively charged electrode and the negatively poled side strains oppositely.

The in-plane expansion and contraction of the material may be utilized by bonding actuating plates to either side of a center shim, (figure 2.5). One is expanded and one is contracted; the net result is a bending displacement much greater than the length deformation of either of the two layers. This configuration, which takes advantage of the Poisson-like d_{31} effect, is referred to as a bimorph or a bender element. It will serve as the primary actuator mechanization for the investigation described herein.

The behavior of piezoelectric properties has been treated in this work with linear relationships. This assumption is valid for low voltages applied and small deformations. The nonlinearities and nonidealities of these materials have been well-documented by References 1.6, 1.7 and 1.9. Several nonideal properties which have been found to have significance are the amplitude dependence of the field-strain relationship, creep which induces a frequency dependent behavior, mechanical strain, and depoling. These issues are not directly addressed here, however, efforts have been exerted to avoid known problems. The amplitude of the control signal voltage was low, avoiding depoling and maintaining the linear strain-field relation. The frequency of flutter was approximately 10 Hz, thus avoiding the creep phenomenon. The plates were also placed on a region where the mechanical strain at rest was very small.

2.2 APPLICATIONS

Piezoelectric materials do not discriminate between sensing and actuating applications. Piezoelectric devices used as sensors emit voltages when subjected to a mechanical load; sensor applications will not be discussed further. In an actuating application, the converse piezoelectric effect is utilized as the actuators deform in response to a control signal or applied voltage. The mention of actuators brings to mind hydraulics, pistons, etc. A broader perspective is required. When commanded, actuators move things. The use of adaptive materials in this manner has lassoed engineering interest from various areas. The following section provides an overview of the many interesting investigations being conducted.

In the area of rotocraft, two distinctly different actuator configurations have been examined for higher harmonic control.[1.9, 1.10] The first used directionally attached plates to

torsionally activate blade sections and actuate a trailing edge flap. The magnitude of flapping vibrations was significantly reduced using active feedback. The second utilized a push-pull configuration of bender elements. Another actuating application, detailed in Reference 1.10, is the active damping of truss members for large space structure applications. This study used commercially available actuators which utilize the d_{33} effect (the expansion direction coincides with the direction of polarization) to limit the vibration amplitude and settling time of transients induced by dynamic perturbations to the structure such as crew motion. In the acoustics field recent work[1.12] has focused on reducing cabin noise through destructive interference produced by distributed piezoelectic plates. Separate Finite Impulse Response filters were constructed to control an acoustic resonance and a structural mode occurring 25% above the acoustic resonance. Reference 1.13 used piezoelectric plates in a bimorph configuration on an Aluminum beam in conjunction with an adaptive LMS controller to attenuate vibrations with frequencies above 300 Hz. Reference 1.14 details experiments and analyses of a composite beam with distributed embedded actuators controlling structural modes from 11 to 150 Hz. Through active feedback of velocity, structural damping increases of an order of magnitude were obtained.

2.3 TEST ARTICLE DESIGN

The test article includes a rigid wing and a flexible mount system. The design of the test article was accomplished through an iterative procedure and parametric studies. There are three driving factors in the design: the model had to flutter within the wind tunnel envelope, had to fit inside the wind tunnel with certain margins of safety and had to have flat surfaces on which piezoelectric actuating plates could be mounted. It was decided a priori that a flexible mount system would reside outside of the wind tunnel and provide the degrees of freedom for a rigid wing; it would be free to plunge and pitch.

A flowchart , (figure 2.6), illustrates the model design procedure used to arrive at the mount system and wing design. The first step is to generate a wing model with geometric properties compatible with the wind tunnel limitations. Secondly, stiffness properties of the mount system must be chosen. An analytical model is constructed using aerodynamics which were calculated assuming that the modes were plunge and pitch. Assuming uncoupled modes which results in a non-diagonal mass matrix, a flutter analysis is performed on the configuration. If flutter occurs well within the tunnel envelope then a mount system is designed which will have the stiffness properties identified in the previous step. Otherwise, an iteration is made to redesign the wing or reassign the mount system properties. Once a configuration with desirable flutter characteristics has been determined, beam theory equations are utilized to explore the possible combinations of spring tine thickness, width, length and material to arrive at an approximate configuration. A finite element model is constructed of the mount system and wing; a second flutter analysis is performed to verify the model. This flutter analysis uses the mode shapes, frequencies, and mass matrix calculated using the finite element model. If the natural frequencies and flutter results are reasonable, then the question is asked as to whether the design is buildable.

Bearing in mind geometric limitations imposed by the tunnel which will be further elucidated in the next chapter, an initial chord length of 2 inches was chosen. This allowed for safe clearance when the model was plunging an inch and pitching to 45 degrees. The wing span was 4 inches, corresponding to 80% of the entire height of the tunnel test section. The mass properties were specified as those of an isotropic steel plate with the pitch pivot at the midchord. The mount system stiffnesses for plunging and pitching degrees of freedom were initially chosen such that the natural frequencies were at 9 and 18 Hz, respectively.

Sensitivity studies were performed on a baseline model by varying each of 9 design parameters independently and noting the changes in flutter velocity and frequency. Figures 2.7 through 2.10 show the resulting trends for variations of the static unbalance, frequency ratio, pitch pivot location, and structural damping. The values on the plots for variation with static unbalance, pitch pivot location and structural damping have been normalized independently of the others. The flutter velocities on a given plot are divided by the flutter velocity corresponding to the lowest value of the parameter being varied. The flutter frequencies were normalized in the same manner. Thus, on each plot, the value of left-most point will be 1.0 and apply to both the flutter velocity and frequency. Figure 2.7 shows that as the static unbalance increased, the flutter velocity will decrease. This is indicative of the additional mass coupling influencing modal coalescence. The frequency trend for the same variation shows an increasing frequency. This indicates that the higher frequency mode might play a more significant role in the flutter mechanism as the static unbalance term of the mass matrix grows. Figure 2.8 shows the flutter velocity trend as the ratio of frequencies is varied. The ratio of frequencies is defined by the plunge frequency divided by the pitch frequency. Two sets of data are plotted in figure 2.8. The first set is for various plunging frequencies divided by the baseline value of the pitching frequency, 19 Hz. The graph shows that as the ratio of the frequencies gets larger, the flutter speed decreases. The second set of data is for the baseline value of the plunging frequency, 8 Hz, divided by various values of pitching frequency. The trend is also for flutter velocity to decrease as this ratio increases. Note that the increasing ratio represents the distance between the natural frequencies decreasing. The plot of the pitch pivot location, (figure 2.9), indicates that as the pivot point is moved towards the trailing edge of the airfoil, the flutter velocity is lowered. Recalling that for these variations the center of gravity was located at the midchord, or 1.0, locations aft of 1.0 are for statically unstable wings. Long before flutter, divergence will have occured. Figure 2.10 shows the change in flutter velocity and frequency as the structural damping is increased simultaneously in both the

plunge and the pitch modes. The trends show that the velocity increases, as expected, since the eigenvalues at zero airspeed will be further from the instability point (i.e. the modes are more stable). The trend is not linear, but for low values, each percent of additional structural damping raises the velocity by roughly a percent. The frequency of flutter is shown to decrease as structural damping is added. The addition of structural damping lowers values of damped frequencies and brings them closer together, predictably lowering the flutter frequency. Basing changes to the design on the trends seen in these parametric variations, the number of iterations required in arriving at a final configuration are greatly reduced.

The final configuration is shown in figure 2.11. Details are discussed in the following chapter. The baseline case examined and described above was modified in several respects: the primary wing structure was constructed with Aluminum, providing the lower mass and inertia characteristics called for; the shape was changed to a blunted diamond with a flat midchord; the wing was extended in the chordwise direction with a balsa wood addition, moving the center of lift aft to approximately the same location as the pivot point; and mass ballast was added to the trailing edge to lower the bending and torsion frequencies and most importantly provide increased coupling between the plunging and pitching modes.

In addition to these alterations, the design of the hardware had several iterations. Because of the model's small size there were many complicating factors. The degree to which idealities, such as cantilevered boundary conditions, could be achieved also necessitated several design iterations.

CHAPTER 3 EXPERIMENTAL CONFIGURATION

The description of the experimental configuration has been broken into three parts. A description of the test hardware is first presented; the digital computer description follows. A final section details the connections among the test hardware components and includes the digital computer's role.

3.1 EXPERIMENTAL APPARATUS

The hardware involved in this wind tunnel test is described in three sections: the wind tunnel, the test article, and the instrumentation.

3.1.1 Wind Tunnel

The Flutter Research and Experiment Device (FRED) shown in figure 3.1, is an open circuit table top wind tunnel with a maximum operating velocity of 85 miles per hour (approximately 1500 inches per second). The test section is six inches by six inches, and is constructed of plexiglass for model viewing. The flow is pulled through the tunnel by a 2 horsepower motor and smoothed by a single honeycomb screen at the beginning of the contraction duct. Models are mounted from the removable ceiling of the test section.

3.1.2 Test Article

The wind tunnel model consists of two components: a flexible mount system and a rigid wing. A third important aspect of the test article is the incorporation of the actuators. The physical system has two distinct modes. When no mass coupling was present, the lower frequency mode was a plunge mode- translation in one plane. The higher frequency mode was a rotation about the wing pitch axis. The wing was designed such that the modes would be coupled by virtue of the mass distribution and also to generate no net lift at zero angle of attack and to have no tendency to load up as velocity is increased.

3.1.2.1 Mount System

The mount system, (figure 2.11), has two degrees of freedom - plunge and pitch. The apparatus is exterior to the wind tunnel and suspends the airfoil by two pins through slots in the test section ceiling.

The plunge mechanism consists of two spring steel plates or tines separated by .75 inches and clamped at both ends to maintain this distance. This provides the pure plunging motion of a beam with guided boundary conditions instead of the flapping motion associated with a cantilevered beam. The pitch mechanism is a single spring tine connected to the wing at the leading edge and at the .2353 chord location, where there is a bearing-like mechanism which allows for free rotation. This configuration provides the airfoil with pitch stiffness and a pitch axis. The two mechanisms are joined together as shown in figure 3.2. The forward end of the pitch mechanism is fixed relative to the plunge springs by mounting the pitch pivot pin to the lower clamping block of the plunge mechanism.

The mount system was designed such that each degree of freedom could be controlled as independently as possible from the other mode. Additionally, each degree of freedom is

controlled by leaf springs, which provide flat surfaces on which sheets of piezoelectric ceramics can be afixed.

3.1.2.2 Wing

The wing, depicted in figure 3.3, consists of three sections: an aluminum primary structure, a balsa wood extension, and an aluminum mass ballast. The primary wing structure is formed from one eighth inch thick isotropic aluminum with a diamond cross-section and blunted leading and trailing edges and midchord section. It has a chord of 2 inches, with the pitch pivot at the midchord. The balsa wood extension overlays the aft half of the primary structure and extends the chord length to 4.25 inches. The trailing edge of this section was coated with aluminum to provide a mass ballast. The mass of the entire wing is .090 lbm and has an inertia about the pitch axis of .134 lbm-square inches. All three sections extend the full span of the wing, which is 4 inches. Table 3.1 gives the measured mass and location of the center of gravity for each portion of the wing. Based on measured dimensions, mass and distance to the pitch point, inertias for the component parts were calculated; the results are given in Table 3.2.

$$I_{cg} = \frac{1}{12}(\text{mass})x(\text{width})^2 \tag{3.1}$$

$$I_{pivot} = (\text{mass})x(\text{distance})^2 + I_{cg} \tag{3.2}$$

3.1.2.3 Piezoelectric Actuators

Four sets of piezoelectric ceramic plates were installed to actuate the test article. Two plates are bonded to opposing sides of the plunge spring tine, with their poles both oriented towards the steel, to form an actuator. The plates are electrically isolated from the steel by the bonding layers. Small copper tabs afixed beneath the plates during the bonding process

serve as the means of applying voltages to the bonded-side electrodes. Only one set of actuating plates, located near the root of one plunge tine was used as a feedback controller.

3.1.3 Instrumentation

3.1.3.1 Strain Gages

A strain gage bridge was mounted near the base of the right plunge spring tine, with two gages on either side of the tine. The gages, which had an overall gage factor of 2.075, were configured to measure the cantilever bending strain. The bridge was powered by a +/- 5 volt power supply. The strain was computed by taking the ratio of the output voltage to the input voltage and dividing by the gage factor.

$$\varepsilon = \frac{V_{output}}{V_{input} G.F.} \tag{3.3}$$

The output voltage from the strain gage was amplified by 100 before being sent to the digital computer.

3.1.3.2 Accelerometer

An Endevco piezoelectric accelerometer was used in this experiment. It was powered by an external 4 milliamp current source. A variable gain amplifier was used with gains of 1, 10 and 100. The output was calibrated at 9.98 millivolts per g.

3.1.3.3 Velocimeter

A Kurz 443M air velocity meter gave visual readouts of the test section airspeed. This is a hot film anemometer with an analog display in meters per second. The probe was inserted into the flow just behind the model in the test section. Thus, in order to accurately measure

the velocity, the model must be moved to the stops to eliminate blockage and the influence of airfoil oscillations on the reading.

3.1.3.4 Operational Amplifier

An Apex Microtechnology P83A operational amplifier was used to boost the input voltage to the piezoelectric actuators. The signal source or input voltage was amplified by a factor of 25, with a limit on the output voltage equal to the power supply voltage, which in this experiment was +/- 80 volts. The schematic in figure 3.4 shows the connections to the power supply, signal source and piezoelectric plates.

3.2 DIGITAL CONTROLLER / DATA ACQUISITION SYSTEM

The control laws are implemented using a personal computer, with a 80386 processor and 80387 co-processor running a real time Unix operating system. The control laws are programmed in the C-language and use floating point arithmetic for all control law calculations. The data acquisition system uses 12 bit analog-to-digital converters with a sample rate up to 500 Hz for a gain feedback single input / single output control law.[3.1]

3.3 EXPERIMENTAL TEST SETUP

The wind tunnel and model had three sensor systems: a strain gage bridge, a linear accelerometer and a hot wire anemometer. The first two were recorded by the digital controller. Strain, measured by a strain gage bridge mounted at the base of a plunge spring tine served as the feedback signal for the control law. The accelerometer served as a roving measurement, being placed where applicable for different experiments. During zero airspeed testing, it was located on the airfoil, however, during flutter testing it was installed on the clamping block. Both the strain and the acceleration were amplified by 100 before

being sent to the analog-to-digital converters. The output voltage of the controller was sent to an operational amplifier having a gain of 25 and a limit on the output voltage of 80 volts. This limited the usable range of output values from the controller to +/- 3.2 volts. The amplified voltage was then applied across each of the piezoelectric elements. A block diagram of the closed loop system with active feedback is presented in figure 3.5. Only the signals employed in the feedback scheme are shown.

CHAPTER 4 ANALYTICAL MODELING

The aeroelastic model has been developed assuming natural modes of vibration as the generalized coordinates utilizing classical techniques available to the aeroelastic community. The exception to this statement is in the treatment of the piezoelectric elements. The equations are thus developed here in a manner that is easily utilized for computation of the actuating forces due to the piezoelectric plates. The fact that they are plates leads to the use of laminated plate theory to model their behavior.

This chapter will address first the constitutive relations for an electromechanical structure. Aeroelastic equations of motion will then be developed using laminated plate theory. The actuating forces are next scrutinized. The fourth section of this chapter deals with the actual procedures used in generating and assembling each of these pieces of the open loop plant. It details the software and the inputs and outputs to each program. Section 5 shows the modeling of the control computer dynamics. The final section details scaling the data for units and amplifiers along with the incorporation of experimentally-determined correction factors.

4.1 CONSTITUTIVE RELATIONS FOR ELECTROMECHANICAL SYSTEMS

The modeling of piezoelectrical systems requires consideration of both mechanical and electrical behavior. Coupling between mechanical stresses and electrical fields is analytically represented by constitutive relationships which contain both the electrical

quantities and the mechanical quantities. These equations are often likened to the constitutive relationships applicable to mechanical systems under temperature loads. A temperature distribution applied to a structure generates thermal strains. The same behavioral model can be used to discuss piezoelectricity, where the electrical field applied is analogous to the change in temperature. The thermal expansion coefficients are replaced by the electromechanical coupling coefficients.[2]

Mechanical stresses and strains are related through a 6 by 6 compliance matrix in the generalized Hooke's law. The constitutive relations for a linear elastic material with three mutually perpendicular planes of elastic symmetry have 9 independent entries in the compliance matrix. Classic laminated plate theory [4.1] is to be used in developing the equations, so only the in-plane stresses and strains are considered, reducing the independent elements to 4, as shown in the following equation.

$$\begin{Bmatrix} \varepsilon_{xx} \\ \varepsilon_{yy} \\ \gamma_{xy} \end{Bmatrix} = \begin{bmatrix} \frac{1}{E_1} & -\frac{\nu_{21}}{E_2} & 0 \\ -\frac{\nu_{12}}{E_1} & \frac{1}{E_2} & 0 \\ 0 & 0 & \frac{1}{G_{12}} \end{bmatrix} \begin{Bmatrix} \sigma_x \\ \sigma_y \\ \tau_{xy} \end{Bmatrix} \tag{4.1}$$

which can be expressed as

$$\varepsilon = [S]\,\sigma \tag{4.2}$$

The strain vector, ε, and the stress vector, σ, are related by the compliance matrix, S. An alternate method of expressing this relationship is through a stiffness, G, matrix.

$$\sigma = [G]\varepsilon \tag{4.3}$$

The electrical quantities (flux density, R, and voltage per thickness, $\boldsymbol{E}$) are related by the dielectric equations through permittivity, β, and impermittivity, ϵ, matrices.[1.7]

$$\boldsymbol{E} = [\beta]R \tag{4.3}$$

$$R = [\epsilon]\boldsymbol{E} \tag{4.4}$$

where

$$\boldsymbol{E} = \frac{\boldsymbol{V}}{t} \tag{4.5}$$

For piezoelectric systems, the coupling of the two fields is accomplished by the introduction of the strain/charge matrix.

$$\varepsilon = [S]\ \sigma + [d]^T \boldsymbol{E} \tag{4.6}$$

The nonzero terms for a PZT plate with poling in the 3-direction are:

$$[d] = \begin{bmatrix} 0 & 0 & 0 & 0 & d_{15} & 0 \\ 0 & 0 & 0 & d_{24} & 0 & 0 \\ d_{31} & d_{32} & d_{33} & 0 & 0 & 0 \end{bmatrix} \tag{4.7}$$

Once again, using classic laminated plate theory, this matrix reduces to a 3 by 3:

$$[d] = \begin{bmatrix} 0 & 0 & d_{15} \\ 0 & 0 & 0 \\ d_{31} & d_{32} & 0 \end{bmatrix} \tag{4.8}$$

Because the electrodes are on the faces of the plate perpendicular to the poling direction, the only voltage which can be applied is in the 3-direction. Therefore,

$$\boldsymbol{E} = \begin{Bmatrix} 0 \\ 0 \\ \boldsymbol{E}_3 \end{Bmatrix} \tag{4.9}$$

Defining Λ as the actuation strain vector leads to

$$\Lambda = \begin{Bmatrix} \Lambda_1 \\ \Lambda_2 \\ \Lambda_3 \end{Bmatrix} = [d]^T \boldsymbol{E} = \begin{Bmatrix} d_{31} \\ d_{32} \\ 0 \end{Bmatrix} \boldsymbol{E}_3 \tag{4.10}$$

Solving equation 4.6 for the stress vector, and defining G as the inverse of the compliance matrix,

$$\sigma = [G](\varepsilon - \Lambda) \tag{4.11}$$

where

$$[G] = \begin{bmatrix} \frac{E_1}{1-\nu_{12}\nu_{21}} & \frac{\nu_{21}E_2}{1-\nu_{12}\nu_{21}} & 0 \\ \frac{\nu_{12}E_2}{1-\nu_{12}\nu_{21}} & \frac{E_2}{1-\nu_{12}\nu_{21}} & 0 \\ 0 & 0 & G_{12} \end{bmatrix} \tag{4.12}$$

Note that the laminar plate model neglects any influence of the d_{33} or the d_{15} coefficients.

4.2 EQUATIONS OF MOTION FOR AEROELASTIC SYSTEMS UTILIZING LAMINATED PLATE THEORY

Lagrange's equations of motion require the derivation of expressions for potential and kinetic energy as function of generalized coordinates. The aeroelastic modeling was performed using the orthogonal or undamped modes of vibration as the generalized coordinates.

Plate displacements can be expressed in terms of these coordinates:

$$u(x,y,z,t) = \sum_{i=1}^{L} \Psi_{xi}(x,y,z) q_{xi}(t) \tag{4.13}$$

$$v(x,y,z,t) = \sum_{i=1}^{M} \Psi_{yi}(x,y,z) q_{yi}(t) \tag{4.14}$$

$$w(x,y,z,t) = \sum_{i=1}^{N} \Psi_{zi}(x,y,z) q_{zi}(t) \tag{4.15}$$

$\Psi_{(x,y,z)i}$ are the mode shape vectors in the x, y, and z directions, respectively, and $q_{(x,y,z)i}(t)$ are time dependent generalized coordinates . The x-translation, u, of the system at the (x_0, y_0, z_0) location is expressed as:

$$u(x_0, y_0, z_0) = \Psi_{x1}(x_0, y_0, z_0)q_{x1} + \Psi_{x2}(x_0, y_0, z_0)q_{x2} + \cdots \quad (4.16)$$

In matrix notations, the translational degrees of freedom can be written

$$\begin{Bmatrix} u \\ v \\ w \end{Bmatrix} = [\Psi]q \quad , \quad (4.17)$$

where

$$[\Psi] = \begin{bmatrix} [\Psi_{x1}\ \Psi_{x2}\cdots\Psi_{xL}] & 0 & 0 \\ 0 & [\Psi_{y1}\ \Psi_{y2}\cdots\Psi_{yM}] & 0 \\ 0 & 0 & [\Psi_{z1}\ \Psi_{z2}\cdots\Psi_{zN}] \end{bmatrix} \quad (4.18)$$

and

$$q^T = \{q_{x1}\ q_{x2}\cdots q_{xL} : q_{y1}\ q_{y2}\cdots q_{yM} : q_{z1}\ q_{z2}\cdots q_{zN}\}. \quad (4.19)$$

The potential energy of the system is defined

$$U = \tfrac{1}{2}\iiint_{\text{Volume}} \{\varepsilon\}^T\{\sigma\}dV \quad (4.20)$$

The constitutive equations provide the relationship between the stress and strain:

$$\sigma = G(\varepsilon - \Lambda) \quad (4.21)$$

The total strain, ε, can be calculated based on midplane strain, ε_0 , and curvature, κ. The longitudinal and lateral strains and the shear strain are defined:

$$\varepsilon_{xx} = \frac{\partial u}{\partial x} \quad (4.22)$$

$$\varepsilon_{yy} = \frac{\partial v}{\partial y} \quad (4.23)$$

$$\gamma_{xy} = \frac{\partial u}{\partial y} + \frac{\partial v}{\partial x} \quad (4.24)$$

For a plate, the displacements are related to quantities at the midplane (midplane denoted by the subscript , 0);

$$u = u_0 - z\frac{\partial w_0}{\partial x} \tag{4.25}$$

$$v = v_0 - z\frac{\partial w_0}{\partial y} \tag{4.26}$$

$$w = w_0 \tag{4.27}$$

which allows the plate strains to be expressed as

$$\varepsilon_{xx} = \frac{\partial u_0}{\partial x} - z\frac{\partial^2 w_0}{\partial x^2} \tag{4.28}$$

$$\varepsilon_{yy} = \frac{\partial v_0}{\partial y} - z\frac{\partial^2 w_0}{\partial^2 y} \tag{4.29}$$

$$\gamma_{xy} = \frac{\partial u_0}{\partial y} + \frac{\partial v_0}{\partial x} - 2z\frac{\partial^2 w_0}{\partial x \partial y} \tag{4.30}$$

or

$$\varepsilon_{xx} = \varepsilon_{xx_0} + z\kappa_x \tag{4.31}$$

$$\varepsilon_{yy} = \varepsilon_{yy_0} + z\kappa_y \tag{4.32}$$

$$\gamma_{xy} = \gamma_{xy_0} + z\kappa_{xy} \tag{4.33}$$

where the following definitions are made:

$$\varepsilon_{xx_0} = \frac{\partial u_0}{\partial x}$$

$$\varepsilon_{yy_0} = \frac{\partial v_0}{\partial y}$$

$$\gamma_{xy} = \frac{\partial u_0}{\partial y} + \frac{\partial v_0}{\partial x} \tag{4.34 a, b, c}$$

$$\kappa_x = -\frac{\partial^2 w_0}{\partial x^2}$$

$$\kappa_y = -\frac{\partial^2 w_0}{\partial y^2}$$

$$\kappa_{xy} = -2\frac{\partial^2 w_0}{\partial x\, \partial y} \tag{4.35 a, b, c}$$

Strain, expressed as

$$\varepsilon = \varepsilon_0 + z\kappa \tag{4.36}$$

is substituted into the constitutive equations to provide

$$\sigma = G(\varepsilon_0 + z\kappa - \Lambda). \tag{4.37}$$

The potential energy now becomes:

$$U = \frac{1}{2}\iiint_{Volume} (\varepsilon_0 + z\kappa)^T G(\varepsilon_0 + z\kappa - \Lambda) dV \tag{4.38}$$

$$= \frac{1}{2}\iiint_{Volume} (\varepsilon_0 + z\kappa)^T G(\varepsilon_0 + z\kappa) dV - \frac{1}{2}\iiint_{Volume} (\varepsilon_0 + z\kappa)^T G\{\Lambda\} dV \tag{4.39}$$

Note that the midplane strain and the curvature are independent of z. Thus,

$$\iiint_{Volume} dV = \iint_{Area} \int_{Thickness} dz \quad dA \tag{4.40}$$

The potential energy can then be calculated

$$U = \frac{1}{2}\iint_{Area} \varepsilon_0{}^T \left[\int_{Thickness} G \quad dz\right] \varepsilon_0 + \varepsilon_0{}^T \left[\int_{Thickness} Gz \quad dz\right] \kappa + \kappa^T \left[\int_{Thickness} Gz \quad dz\right] \varepsilon_0 + \kappa^T \left[\int_{Thickness} Gz^2 \; dz\right] \kappa \quad dA$$

$$-\frac{1}{2}\iint_{Area} \varepsilon_0{}^T \left[\int_{Thickness} G\Lambda \; dz\right] + \kappa^T \left[\int_{Thickness} Gz\Lambda \quad dz\right] dA \tag{4.41}$$

Defining the integrals through the thickness:

$$\mathbf{A} = \int_{Thickness} G \quad dz \tag{4.42}$$

$$\mathbf{B} = \int_{Thickness} Gz \quad dz \tag{4.43}$$

$$\mathbf{D} = \int_{Thickness} Gz^2 \; dz \tag{4.44}$$

$$\mathbf{N}_\Lambda = \int_{Thickness} G\Lambda \; dz \tag{4.45}$$

$$\mathbf{M}_{\Lambda} = \int_{\text{Thickness}} \mathrm{Gz}\Lambda \; dz \tag{4.46}$$

The A, B and D matrices are called extensional, coupling and bending stiffnesses, respectively.

The potential energy, expressed in terms of these integrals is written

$$U = \frac{1}{2}\iint_{\text{Area}} \varepsilon_0{}^{T}A\varepsilon_0 + \varepsilon_0{}^{T}B\kappa + \kappa^{T}B\varepsilon_0 + \kappa^{T}D\kappa \; dA$$
$$-\frac{1}{2}\iint_{\text{Area}} \varepsilon_0{}^{T}N_{\Lambda} + \kappa^{T}M_{\Lambda} \; dA \tag{4.47}$$

or

$$U = \frac{1}{2}\iint_{\text{Area}} \{\varepsilon_0{}^{T} \quad \kappa^{T}\}\begin{bmatrix} A & B \\ B & D \end{bmatrix}\begin{Bmatrix} \varepsilon_0 \\ \kappa \end{Bmatrix} dA - \frac{1}{2}\iint_{\text{Area}} \{\varepsilon_0{}^{T} \quad \kappa^{T}\}\begin{Bmatrix} N_{\Lambda} \\ M_{\Lambda} \end{Bmatrix} dA \tag{4.48}$$

Referring back to the strain and curvature functions in terms of displacements, an operator, D , is defined such that

$$\begin{Bmatrix} \varepsilon_0 \\ \kappa \end{Bmatrix} = [D]\begin{Bmatrix} u_0 \\ v_0 \\ w_0 \end{Bmatrix}, \tag{4.49}$$

where

$$[D]^{T} = \begin{bmatrix} \frac{\partial}{\partial x} & 0 & \frac{\partial}{\partial y} & 0 & 0 & 0 \\ 0 & \frac{\partial}{\partial y} & \frac{\partial}{\partial x} & 0 & 0 & 0 \\ 0 & 0 & 0 & -\frac{\partial^2}{\partial x^2} & -\frac{\partial^2}{\partial y^2} & -2\frac{\partial^2}{\partial x \partial y} \end{bmatrix} \tag{4.50}$$

The general relation from midplane displacements to displacements at a distance, z, from the midplane is easily derived. However, if the displacements are given for the midplane,

as is the case for plate element results of a finite element model, there is a one-to-one correspondence. The subscripts on the displacement vector are thus dropped.

Recalling the expression for the displacements in terms of generalized coordinates allows the midplane strain and curvature to be expressed

$$\begin{Bmatrix} \varepsilon_0 \\ \kappa \end{Bmatrix} = [D][\Psi]q(t) \tag{4.51}$$

Substituting this expression into the potential energy expression,

$$U = \frac{1}{2}\iint_{Area} q^T \Psi^T D^T \begin{bmatrix} A & B \\ B & D \end{bmatrix} D\Psi q dA - \frac{1}{2}\iint_{Area} q^T \Psi^T D^T \begin{Bmatrix} N_\Lambda \\ M_\Lambda \end{Bmatrix} dA \tag{4.52}$$

or, moving the generalized coordinate outside of the integrals

$$U = \tfrac{1}{2} q^T F_1 q - \tfrac{1}{2} q^T F_2, \tag{4.53}$$

where

$$F_1 = \iint_{Area} [D\Psi]^T \begin{bmatrix} A & B \\ B & D \end{bmatrix} [D\Psi] dA \tag{4.54}$$

$$F_2 = \iint_{Area} [D\Psi]^T \begin{Bmatrix} N_\Lambda \\ M_\Lambda \end{Bmatrix} dA \tag{4.55}$$

F_1 is the generalized structural stiffness matrix, K_s.

The kinetic energy development follows a similar path. By definition, kinetic energy, T, is

$$T = \tfrac{1}{2} \iiint_{Volume} \rho \{\dot{u}\}^T \{\dot{u}\} dV, \tag{4.56}$$

where

$$\{u\} = \begin{Bmatrix} u \\ v \\ w \end{Bmatrix} \tag{4.57}$$

From equation 4.17, the displacement vector is expressed by the mode shapes multiplied by the generalized coordinates. The mode shapes are independent of time, so that the expression for the time derivative of displacement is

$$\{\dot{u}\} = [\Psi]\{\dot{q}\} \tag{4.58}$$

where $\dot{(\ )}$ represents the derivative with respect to time. The kinetic energy is then written

$$T = \tfrac{1}{2} \iiint_{\text{Volume}} \rho \dot{q}^T \Psi^T \Psi \dot{q} dV \tag{4.59}$$

Moving the generalized coordinates outside of the integral, the expression becomes

$$= \tfrac{1}{2} \dot{q}^T \iiint_{\text{Volume}} \rho \Psi^T \Psi dV \dot{q} \tag{4.60}$$

or

$$T = \tfrac{1}{2} \dot{q}^T F_3 \dot{q} \tag{4.61}$$

where

$$F_3 = \iiint_{\text{Volume}} \rho \Psi^T \Psi dV \tag{4.62}$$

The triple integral over the volume can be expressed as the double integral over the area of the integral over the thickness. Assuming that the mode shapes are constant through the thickness, the mass per unit area, m_0, can be defined as the integral of the density through the thickness. The expression for F_3 is recognized as the generalized structural mass matrix.

$$M_S = F_3 = \iint_{\text{Area}} m_0 \Psi^T \Psi dA \tag{4.63}$$

In formulating the Lagrangian equations of motion, the conservative forces of the system are contained in the potential and kinetic energy expressions.[4.2] The nonconservative forces, namely the aerodynamics, are represented by generalized forces, Q_i.

$$\frac{d}{dt}\left(\frac{\partial T}{\partial q_i}\right)-\frac{\partial T}{\partial q_i}+\frac{\partial U}{\partial q_i}+\frac{\partial D}{\partial \dot{q}_i}=Q_i \tag{4.64}$$

Using the previously-derived energy expressions, the Lagrange equations become

$$F_3\ddot{q}+\frac{\partial D}{\partial \dot{q}_i}+F_1 q=Q_i+F_2 \tag{4.65}$$

which can be transformed to the Laplace domain and rewritten as

$$\left(M_s s^2+D_s s+K_s\right)\{q_f\}+\bar{q}\left[Q_f \vdots Q_p\right]\begin{Bmatrix} q_f \\ q_p \end{Bmatrix}=F_2 \tag{4.66}$$

which is the classical second order aeroelastic equation formulation with the exception of the term on the right hand side. F_2 is the force generated by the actuating strain, which arose from the addition to the potential energy expression. It appeared because a mechanical stress was being produced by a nonmechanical strain. In the aeroelastic problem, Lagrange's equations are written as a balance of mechanical energy.

In order to transform the aerodynamics into the Laplace domain, it was necessary to apply a second order rational function approximation to the aerodynamics.[4.3] These approximations to the flexible forces and control forces are described as

$$Q_f \cong \hat{Q}_f=\left[\hat{A}_0\right]_f+\left[\hat{A}_1\right]_f s\left(\frac{c}{2v}\right)+\left[\hat{A}_2\right]_f s^2\left(\frac{c}{2v}\right)^2 \tag{4.67}$$

$$Q_p \cong \hat{Q}_p=\left[\hat{A}_0\right]_p+\left[\hat{A}_1\right]_p s\left(\frac{c}{2v}\right)+\left[\hat{A}_2\right]_p s^2\left(\frac{c}{2v}\right)^2 \tag{4.68}$$

Neglecting the inertial and damping terms generated by the control surface aerodynamics, the equations of motion are written

$$\left(\tilde{M}\, s^2 + \tilde{D}\, s + \tilde{K}\right)\{q_f\} = F_2 - \bar{q}\left[\hat{A}_0\right]_p \{q_p\} \tag{4.69}$$

where

$$\tilde{K} = K_s + \bar{q}\left[\hat{A}_0\right]_f, \tag{4.70}$$

$$\tilde{D} = D_s + \bar{q}\left(\frac{c}{2v}\right)\left[\hat{A}_1\right]_f \tag{4.71}$$

$$\tilde{M} = M_s + \bar{q}\left(\frac{c}{2v}\right)^2\left[\hat{A}_2\right]_f \tag{4.72}$$

Defining the vectors

$$x_{f_1} = \{q_f\} \tag{4.73}$$

$$x_{f_2} = s\{q_f\} \tag{4.74}$$

these equations can be readily converted to first order form.[4.4]

$$s\begin{Bmatrix} x_{f_1} \\ x_{f_2} \end{Bmatrix} = \begin{bmatrix} 0 & I \\ -\tilde{M}^{-1}\tilde{K} & -\tilde{M}^{-1}\tilde{D} \end{bmatrix}\begin{Bmatrix} x_{f_1} \\ x_{f_2} \end{Bmatrix} + \begin{Bmatrix} 0 \\ -\tilde{M}^{-1}F_2 \end{Bmatrix} - \begin{Bmatrix} 0 \\ -\tilde{M}^{-1}\bar{q}\left[\hat{A}_0\right]_p \end{Bmatrix}\{q_p\} \tag{4.75}$$

4.3 ANALYTICAL MODELING OF THE PIEZOELECTRIC ACTUATOR

The equations derived in the previous section consist of components that are calculated by standard methods, with the exception of the force due to the piezoelectric actuators, F_2. This section presents a more detailed look at the calculation of this matrix as well as the approximations used to implement the calculations.

From equation 4.55, the force is given as

$$F_2 = \iint_{\text{Area}} [D\Psi]^T \begin{Bmatrix} N_\Lambda \\ M_\Lambda \end{Bmatrix} dA$$

The rows of the force and moment due to strain actuation can be specified

$$N_\Lambda = \begin{Bmatrix} N_{\Lambda_1} \\ N_{\Lambda_2} \\ N_{\Lambda_3} \end{Bmatrix}, \tag{4.76}$$

$$M_\Lambda = \begin{Bmatrix} M_{\Lambda_1} \\ M_{\Lambda_2} \\ M_{\Lambda_3} \end{Bmatrix}. \tag{4.77}$$

The definitions of the operator and modal matrices are recalled from equations

$$[D\Psi] = \begin{bmatrix} \frac{\partial}{\partial x} & 0 & 0 \\ 0 & \frac{\partial}{\partial y} & 0 \\ \frac{\partial}{\partial y} & \frac{\partial}{\partial x} & 0 \\ 0 & 0 & -\frac{\partial^2}{\partial x^2} \\ 0 & 0 & -\frac{\partial^2}{\partial y^2} \\ 0 & 0 & -2\frac{\partial^2}{\partial x \partial y} \end{bmatrix} \begin{bmatrix} [\Psi_{x_1}] & 0 & 0 \\ 0 & [\Psi_{y_1}] & 0 \\ 0 & 0 & [\Psi_{z_1}] \end{bmatrix} \tag{4.78}$$

Consider only the out of plane displacements, (i.e. Ψ_{x_1} and Ψ_{y_1} are zero), the matrix dimension shrinks to

$$[D\Psi]^T = \begin{bmatrix} 0 & 0 & 0 & -\frac{\partial^2 \Psi_z}{\partial x^2} & -\frac{\partial^2 \Psi_z}{\partial y^2} & -2\frac{\partial^2 \Psi_z}{\partial x \partial y} \end{bmatrix} \tag{4.79}$$

The design of the flexible mount system gave special consideration to preventing the plunge spring tines from deforming in torsion. The piezoelectric plates are oriented along the spring tines which deform primary in the y-direction (i.e. creating moments about the x-axis). Therefore any derivative taken with respect to x will be considered negligible, leaving

$$[D\Psi]^T = \begin{bmatrix} 0 & 0 & 0 & 0 & -\frac{\partial^2 \Psi_z}{\partial y^2} & 0 \end{bmatrix} \tag{4.80}$$

Thus,

$$F_2 = \int_{Area} \left(-\frac{\partial^2 \Psi_z}{\partial y^2} \right) M_{\Lambda_2} dA \tag{4.81}$$

The piezoelectrically-induced moment was derived in equation 4.46:

$$M_\Lambda = \int_{Thickness} Gz\Lambda \; dz$$

The second row, corresponding to M_{Λ_2}, is

$$M_{\Lambda_2} = \int_{Thickness} \begin{bmatrix} \frac{\nu_{12} E_2}{1-\nu_{12}\nu_{21}} & \frac{E_2}{1-\nu_{12}\nu_{21}} & 0 \end{bmatrix} \begin{Bmatrix} \Lambda_1 \\ \Lambda_2 \\ 0 \end{Bmatrix} zdz \tag{4.82}$$

Recalling from the discussion of constitutive relations,

$$\begin{Bmatrix} \Lambda_1 \\ \Lambda_2 \\ 0 \end{Bmatrix} = \begin{Bmatrix} 1 \\ 1 \\ 0 \end{Bmatrix} d_{31} \frac{V_3}{t} \tag{4.83}$$

Then

$$M_{\Lambda_2} = \int_{Thickness} \left(\frac{\nu_{12}+1}{1-\nu_{12}\nu_{21}} \right) E_2 d_{31} \frac{1}{t} V_3 \, zdz \tag{3.84}$$

Defining

$$\gamma = \left(\frac{\nu_{12}+1}{1-\nu_{12}\nu_{21}} \right) E_2 d_{31} \frac{1}{t} \tag{4.85}$$

provides

$$M_{\Lambda_2} = \int_{Thickness} \gamma V_3 \, zdz \tag{4.86}$$

The scalar, γ, consists of geometric and material properties. For any isotropic lamina, γ is independent of the location, z, so it may be taken outside of the integral. The structure is

considered to consist of several layers composed of different materials. The integral over the thickness is decomposed into several parts.

$$\mathbf{M}_{\Lambda_2} = \left(\gamma_1 \int_{\text{Layer1}} z\,dz + \gamma_2 \int_{\text{Layer2}} z\,dz + \gamma_3 \int_{\text{Layer3}} z\,dz + \gamma_4 \int_{\text{Layer4}} z\,dz + \gamma_5 \int_{\text{Layer5}} z\,dz \right) V_3 \tag{4.87}$$

where the layer geometry is defined in figure 4.1.

γ is a function of the electromechanical coupling coefficient, d_{31}. Neither steel nor the bonding compound exhibit any coupling behavior so for layers 2,3, and 4, the coupling coefficients are all zero. As long as oppositely oriented voltages are applied to the top and bottom plates, they are geometrically and electrically similar such that the integrals through the layers are equal. Therefore,

$$\mathbf{M}_{\Lambda_2} = 2\gamma_1 V_3 \int_{\bar{z}}^{\bar{z}+t} z\,dz \tag{4.88}$$

After solving the integral,

$$\mathbf{M}_{\Lambda_2} = \gamma_1 V_3 \left(2\bar{z}t + t^2\right), \tag{4.89}$$

and

$$F_2 = \iint_{\text{Area}} -\frac{\partial^2 \Psi_z}{\partial y^2} \gamma_1 V_3 \left(2\bar{z}t + t^2\right) dA \tag{4.90}$$

To implement the actuator equation, numerical integration must be performed. The integral equation is approximated as a summation over the node points of a discretized structural model.[4.6]

$$\iint_{\text{Area}} [\ ]\,dA = \sum_{j=1}^{\text{nnodes}} [\ ]_j\ A_j \tag{4.91}$$

where A_j is the surface area associated with each node.

$$F_2 = \sum_{j=1}^{nnodes} \gamma_1 \left(2\bar{z}t + t^2\right)\left(-\frac{\partial^2 \Psi_z}{\partial y^2}\right)_j A_j V_3 \tag{4.92}$$

There are two modes used in the analysis, so

$$F_2 = \gamma_1 \left(2\bar{z}t + t^2\right)\begin{Bmatrix} \sum_{j=1}^{nnodes}\left(-\frac{\partial^2 \Psi_{z1}}{\partial y^2}\right)_j A_j \\ \sum_{j=1}^{nnodes}\left(-\frac{\partial^2 \Psi_{z2}}{\partial y^2}\right)_j A_j \end{Bmatrix} V_3 \tag{4.93}$$

$$F_2 = \begin{Bmatrix} \Gamma_1 \\ \Gamma_2 \end{Bmatrix} d_{31} V_3 \tag{4.94}$$

where Γ_i is associated with the ith mode.

$$\Gamma_i = (2\bar{z} + t)\left(\frac{\nu_{12} + 1}{1 - \nu_{12}\nu_{21}}\right) E_2 \sum_{j=1}^{nnodes}\left(-\frac{\partial^2 \Psi_{zi}}{\partial y^2}\right)_j A_j \tag{4.95}$$

The aeroservoelastic equations of motion are thus

$$s\begin{Bmatrix} x_{f_1} \\ x_{f_2} \end{Bmatrix} = \begin{bmatrix} 0 & I \\ -\tilde{M}^{-1}\tilde{K} & -\tilde{M}^{-1}\tilde{D} \end{bmatrix}\begin{Bmatrix} x_{f_1} \\ x_{f_2} \end{Bmatrix} + \begin{Bmatrix} 0 \\ -\tilde{M}^{-1}(\Gamma d_{31} - \bar{q}\left[\hat{A}_0\right]_p \beta) \end{Bmatrix} V_3 \tag{4.96}$$

where

$$\beta = \frac{1}{V_{max}} \tag{4.97}$$

In traditional controls notation[4.6],

$$\dot{\mathbf{x}} = \mathbf{A}\mathbf{x} + \mathbf{B}\mathbf{u} \tag{4.98}$$

4.4 MODEL CONSTRUCTION

The equations derived in the previous sections were implemented using various software packages. This section will describe the following specific modeling steps. The analytical structural model was discretized; a finite element model was constructed and analyzed. An

aerodynamic model was generated by discretizing the wing. Generalized aerodynamic forces were calculated using lifting surface theory. To implement the aerodynamic forces in state space form they were approximated using rational functions. The actuator and sensor matrices, B and C, were computed using finite difference techniques.

4.4.1 Finite Element Model

A finite element model[4.7] of the wind tunnel wing and the two degree of freedom mount system, (figure 4.2), was constructed and analyzed using MSC NASTRAN[4.8]. The model developed represented the primary airfoil with solid elements; the wing extension and mass ballast were represented with concentrated mass elements. The spring tines were modeled with plate elements. A torsional spring was added at the pivot point to better represent the experimentally-determined pitch frequency.

Observing the physical system in motion indicated that the plunge spring tines had clamped or guided boundary conditions. The full finite element model closely predicted the plunge frequency when this boundary condition was enforced. Further observation of the motion indicated that the pitch spring boundary condition at the pitch pivot point was stiffer than a cantilever, while the other end of the tine looked cantilevered.[4.9] The exaggerated sketch of figure 4.3 depicts this phenomenon. Using experimental frequencies and calculated inertias, spring stiffness constants were computed for three wing configurations: the primary airfoil structure alone, one with the balsa wood wing extension and one also containing a .007 lbm mass ballast. From the average stiffness value, the cantilevered stiffness of the existing finite element model was subtracted. The resulting stiffness was included in the finite element model by means of an explicitly modeled spring at the pitch pivot point.

The locations on the spring tines where piezoelectric plates were bonded were defined as composite plates, where the layers of piezoelectric ceramic utilized temperature-dependent material property capabilities of the code. The parallel constitutive relations of thermal-mechanical and electro-mechanical systems allowed the voltage applied to the ceramics to be represented by an applied temperature field.

4.4.2 Aerodynamics

Unsteady aerodynamics were calculated using the Doublet-Lattice Method[4.10] as implemented in the Aeroelastic Vehicle Analysis (AVA) conglomeration of computer codes.[4.11]

The Doublet-Lattice Method is a panel method for solving the integral equation relating the normal wash and the aerodynamic loading for lifting surfaces in subsonic flow. Discrete lifting elements, consisting of an oscillatory doublet line and a horseshoe vortex, approximate the loading. The steady flow effects are represented by the vortex; the doublet represents the incremental effects of oscillatory, unsteady, motion.

AVA uses the modal displacement vectors to calculate the generalized aerodynamic forces (GAFs) at discrete reduced frequencies. The program output is a table for each reduced frequency, where the columns of the table correspond to modal and control deflections, while the rows correspond to modal pressures or forces. Because the airfoil is rigid over the airspeed range of interest, the displacements are input at six points along the leading and trailing edges of the primary wing section. The aerodynamic model has 5 chordwise boxes and 10 spanwise boxes for a total of 50. The GAFs were calculated at Mach .05 for 8 values of reduced frequency ranging from .001 to 2.0.

4.4.3 Rational Function Approximations for the Aerodynamics

The aerodynamics produced by the Doublet-Lattice code are transcendental functions of reduced frequency. In order to incorporate them into the state space equations of motion, they must be approximated by rational functions of the Laplace variable, s.[4.3] Equations 4.67 and 4.68 illustrate the second order approximations made. The Integration of Structures, Aerodynamics and Controls (ISAC) conglomeration of codes[4.12] was used to perform these approximations and generate the resultant s-plane GAFs. The objective of the fit is to determine the coefficients such that the approximation best fits the tabular data in a least-squares sense subject to a set of linear equality constraints which are imposed upon the coefficients. The constraints imposed for this model are the approximations will exactly match the tabular values at zero reduced frequency for each of the modes. Figure 4.4 shows the GAF's plotted as a function of reduced frequency and the results of the approximation.

4.4.4 Finite Difference Program for Generating Structural Influence Matrix of the Actuators

The actuators have two influences in the equations of motion. The first, traditionally represented influence, is the effect on the aerodynamics. The actuator moves the wing, causing an aerodynamic interaction. The control mode aerodynamic forces were generated by applying simulated voltages within the finite element code and using these displacements as input mode shapes to the Doublet-Lattice aerodynamic portion of AVA. The structural influence matrix, which was denoted Γ, in Section 3 of this chapter, is calculated by a finite difference program. This code calculates the second derivative at the center of each of the structural elements by using the displacements two node points from both sides of the element. The only elements which are included in this calculation are those which are

laminated with the piezoelectric plates. Each of the actuating plates located near the root of the plunge springs consists of 6 elements, each of which are .25 inches in length and 1 inch wide. The actuators nearer the clamping block are shorter and have only 4 elements to model them. The displacements are assumed to be constant across the width of the spring tine, so only one row of displacements along the length are used in the calculations.

4.4.5 Finite Difference Program for Modeling the Strain Gage

Strain gages configured to measure cantilever bending are also governed by the behavior of the second derivative of the motion, taken with respect to the length-wise coordinate.[4.13] The same basic program used in calculating the actuator influence matrix was modified to calculate the strain gage coefficients. The second derivative was calculated at locations near the root of the plunge spring and multiplied by the spring tine thickness to predict the strain on the surface.

4.4.6 Generating the State Space Equations of Motion

Assembly of the equations of motion was done using MATRIXX, a commercially-available software package from Integrated Systems Incorporated.[4.14] The continuous, open loop model was generated in first order form. The procedure, given in Table 4.1, shows the details of the A and B matrix calculations and the C matrix for strain gage measurements. These matrices are then discretized using the appropriate sample rate.

4.5 MODELING THE CONTROL COMPUTER DYNAMICS

The influences of the zero order hold and one time step delay on the closed loop system were examined using Matlab, a commercially available software package from The Math

Works Incorporated.[4.15] The influence of the sample rate was also determined. MATRIXX implicitly models both the zero order hold and a one sample delay automatically when the discretization command is used.

Illustrated in figure 4.5 for a gain feedback control law, the control computer introduces its own dynamics into the feedback path. The digital controller implementation scheme shifts the output data by one sample and applies a zero order hold. The frequency response of the digital controller is different for different sample rates. By using a sample rate which emulates analog derivative feedback near the frequency of control interest allows the system to simulate derivative feedback, despite having only displacement measurements.[4.16] The current control law utilizes the dynamics of the implementation scheme, requiring only gain feedback. The frequencies of concern lie between 7.9 and 11.1 Hertz. Figure 4.5 shows that for a 20 Hz sample rate, the phase is -270 degrees, or +90 degrees at 10 Hz. Thus, the phase characteristics simulate a derivative in the frequency range of interest.

4.6 SCALING AND CORRECTION FACTORS

The experimental setup contains amplifiers, discretizations, etc, which must be included in the analytical model if a controller design is to be applied to the physical system. The strain produced on the model is measured by gages which produce voltages. These voltage levels are insufficient for the digital controller to discern. Thus, an amplifier with a gain of 100 is introduced into the strain path. It must also be kept in mind that the strain is not actually fed back, but a voltage proportional to strain. Any control law generated must account for this factor. The feedforward path, from the control computer to the piezoelectrics also contains an amplifier, which multiplies the input by 25. This gain is included in the computation of the control matrix, B.

The equations generated contain errors due to inability of theory to predict physical phenomena, shortcomings in methods used, neglected terms, and nonidealities of the physical model. The computation of the strain gage values by a finite difference technique had an error of 30% at zero frequency. Because the differencing was performed on plate elements very near the clamped boundary condition, it was determined that the values yielded were inaccurate. The strain gage equations, were scaled by 1.3 to account for this. Zero frequency gains were also computed experimentally for the transfer function from the piezoelectric voltage to the strain gage output. They were off by 20%. This was anticipated due to the unmodeled bonding layer. The control matrix was multiplied by 1.2 in an attempt to correct for this difference.

CHAPTER 5 ANALYSES

Analyses were performed utilizing the aeroservoelastic equations of motion derived and developed in Chapter 4. The finite element model was utilized not only to construct the structural matrices but to assist in several studies. Aeroelastic analysis was performed to predict the open loop flutter speed and frequency and to identify the flutter mechanism. Control law design and closed loop analyses were performed using the discretized form of the equations.

5.1 FINITE ELEMENT ANALYSES

The finite element model served several purposes: 1) the structural matrices were generated; 2) by performing a normal modes analysis, natural frequencies and mode shapes were calculated; 3) a parametric study was performed to design the mass ballast; 4) parameter variations were performed to determine the placement of the actuating plates necessary to obtain the maximum control effect and 5) by incorporating the piezoelectric actuating plates in the finite element model, control surface deflection modes required for the aeroelastic equations were generated.

The presence of the piezoelectric elements on the spring tines makes the calculation of the mass and stiffness characteristics not necessarily straightforward. Approximate values for mass and stiffness properties were calculated based on beam theory equations which neglect any stiffening due to the piezoelectric elements. The plunge spring was modeled with a cantilevered boundary condition while the pitch spring stiffness was computed for cantilevered and then guided boundary conditions. The frequency predictions are presented

in Table 5.1. Finite element results are also presented for various pitch boundary conditions with and without piezoelectric plates incorporated. The pitch spring boundary condition was enforced first as a cantilever and second as a combination of cantilever and guided boundary conditions. The result of the combined system lies between the beam theory predictions of the idealized cantilever and guided beams. The finite element model was augmented with the piezoelectric actuators and reanalyzed. The plunge frequency increased by 15%; there was little influence on the pitch mode, which was modeled using the combined cantilever and guided boundary condition.

Normal mode analyses[5.1] were performed to generate natural frequencies and mode shapes. An eigenvalue analysis was performed to solve the undamped system:

$$\left[\overline{K}_s - \lambda_i \overline{M}_s\right]\{\Psi_i\} = 0 \tag{5.1}$$

The natural frequencies were calculated

$$f_i(\text{Hz}) = \frac{1}{2\pi}\sqrt{\lambda_i} \tag{5.2}$$

The resulting undamped mode shapes, $\{\Psi_i\}$, are orthogonal and, like any eigenvectors, can be arbitrarily scaled. It is a common practice in aeroelastic modeling to scale them such that a unit generalized structural mass matrix is generated.

$$M_s = [\Psi]^{-1}\overline{M}_s[\Psi] = [I] \tag{5.3}$$

The vibration mode shapes are shown in Figure 5.1; the first mode, designated plunge due to the dominance of translational motion, was predicted at a frequency of 7.8 Hz. The second mode, which is characterized by the pitching of the airfoil relative to the mount system, has a natural frequency of 10.9 Hz.

The natural frequencies of the system are dependent upon the mass distribution:

$$\omega_{pl} \propto \sqrt{\frac{k_{pl}}{m}} \tag{5.4}$$

$$\omega_\theta \propto \sqrt{\frac{k_\theta}{I_{yy}}} \qquad (5.5)$$

The total mass of all components supported by the plunge spring tines, m, is used in the calculation of the plunge frequency. The inertia used in the calculation of the pitch frequency is the inertia of the entire wing about the pitch axis. The mass ballast is located far enough from the axis of rotation that it provides a significant contribution to the inertia. The flutter speed has been shown in Chapter 2 to be sensitive to frequency separation. Thus, the flutter characteristics can be adjusted by slight modifications to the mass ballast. Table 5.2 compares the analytical predictions of the natural frequencies for mass ballasts from 0.005 lbm to 0.017 lbm. It also shows the frequencies for the primary wing unballasted and also with only the balsa wood wing extension.

A study was performed to determine the optimal placement of the actuating plates. Using one inch long piezoelectric segments, a pair of actuators was analytically placed at different locations on the plunge spring tines. Table 5.3 shows the displacement generated at the "free" end as a function of the actuator location. The actuators should be placed in regions of high strain. Both investigations indicate that the plates should be placed near either end of the clamped spring tine. A similar investigation for the pitch spring indicated that, if actuators were placed on it, they should be located as near the cantilever end as possible.

A temperature field was used to simulate a voltage applied across the piezoelectric elements. The last two items of the purpose statement are accomplished through this mechanism. To calculate a deflection mode for the control, a modal response to a unit input to the control surface must be generated. Oppositely charged voltages were applied to each side of the actuator, (figure 5.2). The top plate is in contraction in the horizontal or in-plane direction, while the bottom plate is in expansion in the same direction. By using the resultant

displacement vector as a mode shape in the aerodynamic analysis, the modal components of the aerodynamic influence of the control are calculated.

5.2 AEROELASTIC ANALYSIS

Flutter analysis of the model was conducted by analyzing the open loop aeroelastic equations of motion at a given density for various velocities.[5.2] As the velocity changes, the relative influence of the aerodynamic and structural contributions to the inertial, damping, and stiffness characteristics of the system change. The velocity root locus plot of Figure 5.3 shows some of the open loop flutter characteristics. The plot traces the roots of the system as the airspeed is increased. The horizontal axis is the real part, while the vertical axis is the imaginary part. The imaginary axis represents the point of neutral stability or zero damping, where theoretically responses will neither converge nor diverge. Flutter, defined as an oscillatory divergence, is represented on a root locus plot by an eigenvalue crossing this axis into the right half plane.

The figure predicts the behavior of the plunge and pitch modes for sea level density. The frequencies of the two modes migrate towards one another as the aerodynamics couple the two modes. When the frequencies are close together, the modes interact with one another and the system is driven unstable, shown by the plunge mode eigenvalue crossing into the right half plane. The predicted flutter mechanism involves the coalescence of the plunge and pitch modes at a velocity of 560 inches per second and at a frequency of 9.1 Hz.

An alternate method of expressing the same data is to plot the frequencies and the damping ratio as functions of velocity. This method will be discussed later in the comparison of analysis and experiment.

For flutter to occur, both degrees of freedom must be present. Figures 5.4 and 5.5 illustrate the behavior of the system if only one of the modes is present. Either mode by itself has a tendency to become more highly damped as the velocity is increased. The plunge mode, however, shows a static divergence tendency, (frequency approaching zero), and will diverge for a velocity above the wind tunnel limit.

5.3 CONTROL LAW DESIGN & CLOSED LOOP ANALYSIS

Control laws designs for flutter suppression are varied in complexity. Energy methods, including optimal control have been utilized.[1.1, 1.2, 1.3] This approach leads to higher order controllers, which may be necessary for controlling very complex systems. Reference 1.4 utilized classical control methods braced with parameter variations to identify and compensate for weaknesses of the control law. This design was implemented on a free-to-roll wind tunnel model which encompassed both symmetric and antisymmetric flutter modes. Because of the simplicity of the test article considered in this study, a two degree of freedom system, the aeroelastic phenomenon should be controllable through a simple feedback law. Gain feedback[3.6] utilizing the dynamics of the discretization process, is investigated. The strain-proportional voltage is the input to the control law. The signal is discretized by a 20 Hz sampler and then multiplied by the feedback gain. Digital to analog converters hold the output data until the end of the sample period. The output signal is then updated. This value is held until the end of the next sample period, when new output data is available. References 4.6 and 5.3 provide more detailed explanations of the digital-to-analog conversion, called a zero order hold. The dynamics of the control law computer are further investigated in Chapter 5; their influence has been included in the following analyses.

Control law design is traditionally performed in the continuous domain. Because the control law computer dynamics were an integral part of this design, however, the discrete domain model was utilized in this investigation. Figure 5.6 shows the continuous complex plane, (s-plane), and the discrete complex plane, (z-plane). These illustrations aid in understanding the system behavior as the discrete system eigenvalues change. On a diagram of discrete system eigenvalues, the stability condition corresponds to the location of the roots relative to the unit circle. Roots located outside of the unit circle correspond to instabilities, that is, the imaginary axis of the continuous complex plane, maps to the unit circle of the discrete complex plane.

Design models were constructed from the aeroservoelastic equations of motion developed in Chapter 3. Because these equations contain velocity-dependent terms, models were created at several distinct velocities. The equations representing the system at the open loop flutter condition, determined to be 580 inches per second, was the initial design model. The continuous model was discretized with a 20 Hz sample rate. A gain root locus, constructed by varying the gain from 0 to 120 is shown in figure 5.7. Each eigenvalue trace begins at the open loop system values which correspond to a feedback gain of zero. One pair of roots shown in figure 5.7 is unstable for the open loop case because this velocity corresponds to the open loop flutter condition. The flutter mode eigenvalues stabilize for small feedback gains, since they migrate inside the unit circle almost immediately. As the gain increases, the eigenvalues continue to migrate in a stable manner for a feedback gains up to 108, where one destabilizes again.

The stability criterion can be expressed as a limit on the magnitude of the eigenvalues. The magnitude of the largest eigenvalue must be less than 1.0 for the system to be stable. Figure 5.8 shows the value of the maximum magnitude of the eigenvalues plotted against feedback gain. The design model, 580 inches per second, is stabilized for gains higher

than 14 but less than 108. As the gain is increased from 0 to approximately 45, the system becomes more stable; additional gain does not decrease the eigenvalue magnitude. This model, however, represents the system at only one airspeed. The same figure shows the variation with gain for several airspeeds. With barely a puff of air on the model, 1 inch per second, the model is open loop stable. As the gain increases, there is very little change in the eigenvalue magnitude until the gain reaches 102. The magnitude increases and the system is driven unstable for gains of 104 and above. The maximum airspeed for which gain feedback will stabilize the system was found to be 1300 inches per second. As indicated in the figure, gains of between 103 and 108 will stabilize the system at this airspeed. If physically attainable and no stability margins are required, 103 is the optimal gain. Practical limitations on the gain, however, will not allow a gain of this magnitude to be implemented.

Saturation places limits on the implementable feedback gain. In a traditional aircraft control scheme, aerodynamic saturation of the control surfaces as they stall or the limits of hydraulic actuators restrict the gains. In this experiment, the piezoelectric actuators are capable of handling more voltage than the operational amplifier is capable of producing. This then becomes the weak link. The amplifier has an output limit of 80 volts. It amplifies input voltages by 25. Thus, the maximum input voltage is 3.2 volts.

$$\text{maximum gain} * \text{maximum strain response} \leq 3.2 \text{ volts} \qquad (5.6)$$

The open loop strain response has a maximum measured voltage of .08 volts for wind tunnel conditions just below flutter. This would limit the gain to 40. Based on experimental observations, the limit on the gain was refined to 33. The trend illustrated in figure 5.8 indicates that the gain should be as large as possible, but below 104, to stabilize the system over the largest velocity range.

Using the largest allowable feedback gain, 33, a velocity root locus was constructed. Figure 5.9 shows the traces of the eigenvalues as the velocity is increased from 0 to 700. As with the gain root locus, a stable system has eigenvalues all lying within the unit circle. The flutter mode is initially stabilized and then slowly begins to migrate back toward the unit circle. The root crosses the stability boundary, predicting closed loop flutter at 648 inches per second. The previous graph, (figure 5.8), shows the variation of maximum eigenvalue magnitude as a function of gain for this velocity. The influence of increasing velocity can also be seen on this graph by examining the dashed vertical line representing a feedback gain of 33. At 1 inch per second, the eigenvalue is just below the stability point, 1.0. The next velocity plotted is the open loop flutter speed, 580 inches per second. The eigenvalue magnitude has decreased indicating the stabilizing effect of the feedback. Moving to the next velocity plotted in the figure, 648 inches per second, the trace intersects the stability boundary. Recall that this is the closed loop flutter speed. Higher velocities, represented only by the 1300 inches per second plot, indicate a substantially increased magnitude or instability.

A comparison between the open and closed loop eigenvalue magnitudes for increasing velocities is presented in figure 5.10. The effect of the gain feedback is shown to separate the natural frequencies as the aerodynamic influence grows (i.e. the velocity gets larger increasing the magnitude of the aerodynamic contributions to the mass, damping and stiffness matrices). The initial flutter studies, performed in the design phase of the project, indicated that separation of the zero airspeed natural frequencies, or undamped natural frequencies would have the effect of delaying the onset of flutter, (figure 2.13).

5.4 RESULTS SUMMARY

The finite element results indicated that the piezoelectric plates should be placed near the ends of the spring tines. The natural frequencies predicted were 7.8 and 10.9 Hz. The results of the open loop aeroelastic analysis indicate the flutter onset at 560 inches per second. Utilizing gain feedback, with a gain of 33, and control law computer dynamics imparted by a 20 Hz sample rate, the closed loop flutter speed is predicted to improve by 15.7%.

CHAPTER 6 EXPERIMENTS

Experiments were performed at various points during this project. Static testing was performed on the model to check and determine gains within the open loop system. This was a very useful test due to the many component parts which were necessary to conduct the sensing and actuating. System identification testing was performed using several techniques to extract modal frequencies, dampings, transfer functions and general system behavior. Open and closed loop flutter tests were conducted and the results compared to one another as well as to analytical predictions.

6.1 STATIC TESTING

Several tests were performed to determine open loop system gains. To validate and correct the mathematical model, an experiment was devised to check the strain gage coefficients. A known displacement was applied to the clamping block, (figure 3.2); the strain was measured. Applying the same amount of displacement to the mathematical model yielded a strain 30% smaller. The sensors equations associated with the strain gage were increased to give the correct d.c. value. With the strain equation yielding the experimental value, a constant voltage was applied to the piezoelectrics and a strain was measured. The mathematical model predicted 20% less strain than the measured value. The control matrix was then scaled to yield the correct value.

6.2 SYSTEM IDENTIFICATION TESTING

There were several experimental and analytical techniques used to extract system parameters, (figure 6.1). Impulse response functions of the accelerometer generated by

6.2 SYSTEM IDENTIFICATION TESTING

There were several experimental and analytical techniques used to extract system parameters, (figure 6.1). Impulse response functions of the accelerometer generated by hammer tests proved to be the most reliable means of extracting the natural frequencies of the system, but could be used only at zero airspeed because the model could not be directly accessed while in the tunnel. Additionally, the amount of disturbance introduced to the flow by the presence of the accelerometer and its lead wire drastically altered the aerodynamic behavior. A second technique, employed to obtain a more dramatic response from the pitch mode was to pluck the spring tine and record the free decay data. This free decay technique was effective at low airspeeds, where the plucking did not perturb the model enough to induce large oscillation flutter. The third technique was to excite the model by applying random voltage to the piezoelectric actuators. There were several advantages to this method- most importantly, the actuator influence was included in the results. Also, because the amplitude of the input could be carefully controlled, this technique could be used throughout the test envelope without inducing flutter. No access to the model or flow-disrupting gages were required. With this technique, the input is recorded, allowing transfer functions to be calculated.

Two of the three methods involve the calculation of transfer functions. This is accomplished by reading the time histories into Matlab and transforming them , via fast Fourier transforms, into the frequency domain. The autospectrum, Φ_{uu}, of the input and cross-spectrum of the output with the input, Φ_{uy}, are calculated:

$$\Phi_{uu} = \mathrm{FFT}(\mathbf{u}) * \mathrm{FFT}(\mathbf{u}) \qquad (6.1)$$

$$\Phi_{uy} = \mathrm{FFT}(\mathbf{u}) * \mathrm{FFT}(\mathbf{y}) \qquad (6.2)$$

The transfer function is the ratio of the crosspectrum over the autospectrum.

$$\mathbf{R}(s) = \frac{\Phi_{uy}}{\Phi_{uu}} \tag{6.3}$$

6.2.1 Impulse Tests Administered on the Wing Using Hammer Taps

Hammer taps to produce impulse inputs were used at zero airspeed to extract the system natural frequencies for various configurations of the model prior to its being mounted in the wind tunnel.

The first set of impulse tests were designed to extract the uncoupled pitch mode frequency, thus the plunge degree of freedom was constrained. The model was configured with and without the balsa wood extension and with various amounts of mass ballast during these tests. Data was taken for 16 seconds at 64 samples per second. Overlap averaging of several runs was performed to obtain cleaner data. The results of these experiments are given in Table 6.1 and compared with the analytical predictions based on the finite element model. Figure 6.2 which shows frequency domain representations of the accelerometer response for different mass ballasts.

A second set of experiments were performed utilizing the impulsive input which allowed motion in both the plunge and pitch degrees of freedom. Figure 6.3 shows time histories of hammer input, accelerometer response and strain gage output. The power spectral density of the acceleration response, (figure 6.4(a)), indicates that the natural frequencies of the final configuration are 7.9 and 11.1 Hz. Table 6.2 compares the natural frequencies before and after the actuator elements were added to the finite element model to the experimentally-determined values. The structural damping of the plunge mode was also determined from this data by taking the ratio of the frequency width of the peak at the half amplitude and the natural frequency. The damping ratio is half of this value, .017. The power spectrum of the strain response, (figure 6.4(c)), does not define the modes as well,

but also indicates approximately these values for the frequencies. The phase plots are presented in figure 6.4.

6.2.2 Free Decay Tests Administered by Spring Tine Pluck

The rationale in using the free decay test to extract pitch mode data is that, given that there is no actuator for this mode, it can not be excited by random input tests. Additionally, the impulse response testing failed to extract data suitable for determining the pitch mode damping. Because the input signal can not be recorded, no transfer functions between the input and output can be derived using this method. The free decay response to a pluck of the pitch spring tine, however, provides insight into the damping of the pitch mode. Acceleration response of the open loop system was generated by applying 7 impulses during 18 seconds, (figure 6.5). Each response was fully decayed before the next was applied. This data was analyzed using the logarithmic decrement technique.

The logarithmic decrement is defined for a decaying cyclic system by the ratio of peak magnitudes for two cycles, which are n cycles apart.

$$\delta = \frac{1}{n} \ln\left(\frac{x_1}{x_n}\right) \tag{6.4}$$

The relationship of the logarithmic decrement to the damping ratio is

$$\delta = \frac{2\pi\zeta}{\sqrt{1-\zeta^2}} \tag{6.5}$$

which for small values of damping can be approximated

$$\delta = 2\pi\zeta \tag{6.6}$$

giving the formula for damping ratio

$$\zeta = \frac{1}{2\pi n} \ln\left(\frac{x_1}{x_n}\right) \tag{6.7}$$

The structural damping, g, is twice the damping ratio, ζ. For the pitch mode, a damping ratio of .055 was obtained.

Impulse response tests via plucking were also used to examine the potential damping improvements of the control law design. The strain responses to pluck tests of the open and closed loop systems were compared, (figure 6.6). Both were normalized such that the magnitude of the first peak was 1.0 so that they could be compared. Both data sets were obtained at 20 Hz sample rates. From this plot, the structural damping is shown to have been increased by the presence of the controller.

6.2.3 Random Input Tests

The open loop system can not be identified fully with either of the techniques described above because they do not include the influence of the piezoelectric actuator. To obtain system transfer functions, the actuators to be used for control must also be used in the system identification. The random inputs to the piezoelectric plates satisfy this criteria. The input signal was random white noise with a Gaussian distribution and a zero mean value. The amplitude of the signal, limited to 3.2 by the operational amplifier, was adjusted to be as large as possible at different velocities tested. The larger the signal was, the better the data which was obtained in terms of coherence. Large excitations near the flutter velocity, however, drive the model unstable before the actual open loop flutter condition is reached.

Random excitations were used to examine open loop behavior as the wind tunnel velocity was increased. Figure 6.7 shows the magnitude of the strain versus frequency at eight subcritical airspeeds. The plots are dominated by the plunge mode. The sequence of pictures shows that as airspeed is initially increased, the peak magnitude is decreases and the width remains fairly constant. Thus, the half magnitude point falls lower on the curve,

that is, at a wider point on the peak. Qualitatively this indicates that the damping in this mode increases. The fifth picture shows that the damping is decreasing. The response gets progressively less damped as the flutter speed is approached.

6.3 OPEN LOOP FLUTTER TESTING

The risks associated with flutter testing are minimized in this experiment due to the unique design of the test article. Because the mount system is located exterior to the tunnel and the model is small, it is possible to stop flutter by manually taking hold of the flexible springs or the clamping block.

During open loop flutter testing it was discovered that the presence of the lead wires powering the piezoelectric plates increased the damping of the system. Originally, there were four sets of piezoelectric actuators. Removing the wires from three of them removed a significant amount of damping in the plunge degree of freedom and lowered the flutter velocity by four percent.

The flutter tests were conducted by increasing the velocity and allowing the model to sit at the tunnel condition for several minutes. The turbulence within the tunnel was relied upon to be sufficient to perturb the model. Flutter was encountered at 580 inches per second; the frequency of the oscillation was 9.4 Hz. A time history of the strain gage during a run in which flutter was encountered, (figure 6.8), shows the divergent oscillations which begin growing at 4.5 seconds and continue to grown until the maximum possible amplitude is reached at 9.0 seconds. At this amplitude, safety stops of the tunnel inhibit the models motion so that it won't be destroyed. The frequency domain representation of this data, (figure 6.9), indicates the flutter frequency of 9.4 Hz.

6.4 CLOSED LOOP FLUTTER TESTING

The majority of the closed loop flutter testing was conducted by activating the control law at zero airspeed. Proceeding in the same manner as the open loop flutter testing, the speed was increased until flutter was encountered. A comparison of open and closed loop strain shows the decrease in magnitude of the response to wind tunnel turbulence, (figure 6.10). These data were obtained just below the open loop flutter speed, at approximately 570 inches per second. The same data is seen on an expanded time scale in figure 6.11. Due to limitations in the controller programming the controller update rate and data sampling must be consistent. The closed loop data was therefore obtained using a 20 Hz sample rate. The open loop data appears smoother due to a higher sampling rate.

Increasing airspeed required more control energy to be exerted, table 6.3. The data obtained at 710 inches per second is actually above the flutter speed. The control energy bears this out. The system responses do not change significantly as velocity increases until the controller proves insufficient to inhibit flutter, (figure 6.12). The results of the flutter experiments and analyses are summarized in figure 6.13. An increase of 20% in flutter velocity was achieved through active feedback. The closed loop flutter velocity was 697 inches per second at approximately 9.7 Hz.

The model was under almost complete control of the experimenter. The low risk associated with fluttering the model allowed several unorthodox tests to be performed. For the first of these tests, the tunnel velocity was set just above the open loop flutter speed with the model degrees of freedom constrained. With the controller out of the loop the model was released. Just after the onset of flutter, the control system was turned on. The already-large oscillations, begun as unaugmented flutter, were too large to be damped out by the control law. Throughout the analysis of the system, on which the controller design was

based, small perturbations and linear relationships were assumed. The second additional test was performed primarily as a demonstration. With the control system operating, the wind tunnel speed was raised to a point between the open and closed loop flutter speeds. The control law was turned off and divergent oscillations immediately began. This test indicates that the unstable mode does not restabilize, at least within the velocity range covered by the closed loop controller.

CHAPTER 7 CONCLUSIONS & RECOMMENDATIONS

This research effort has resulted in the first experimental demonstration of flutter suppression employing piezoelectric actuators. A wind tunnel model was conceived, designed, fabricated, installed and tested. Structural and aerodynamic models were created; the aeroservoelastic equations of motion were derived and analyses performed. A digital contorl law was designed based on a discretized model and was implemented. Open and closed loop flutter tests were conducted, with excellement correlation achieved by analytical predictions.

A two degree of freedom wind tunnel model consisting of a rigid wing attached to a flexible mount system was designed based on preliminary flutter analyses. The rigid wing, with a primary section made of Aluminum was connected to a cantilevered spring tine to control the pitching degree of freedom and the entire assembly was then connected to a set of spring tines to control the plunging motion. The configuration and dimensions of the model were designed such that it would flutter well within the operating envelope of the tunnel, could be safely tested within the available test section, and would have surfaces suitable for mounting the piezoelectric plates in a bimorph configuration.

Analytical modeling of the wind tunnel model resulted in aeroservoelastic equations of motion. The equations were derived from Lagrange's energy method and utilized modal analysis of a discretized structural model. The natural frequencies were predicted to be 7.8 Hz for the plunge mode and 10.9 Hz for the pitch mode. Generalized aerodynamic forces were generated via the Doublet-Lattice method and approximated with rational functions. Expressions for the generalized forces associated with the control inputs were derived

based on classic laminated plate theory and calculated using finite differencing techniques applied to the discretized structural model results.

Aeroelastic analysis of the open loop system gave a flutter prediction of 560 inches per second. Utilizing the implicit dynamics of the control law computer, a gain feedback control system was designed using strain as the feedback signal. Optimizing the gain for the largest stable velocity range and accounting for saturation of the electronic hardware involved, a value of 33 resulted. The flutter speed for the closed loop system was predicted to be 648 inches per second, a 15.7% increase.

Experimental results from several system identification tests determined the natural frequency of the plunge mode to be 7.9 Hz and that of the pitch mode to be 11.1 Hz. The structural dampings associated with these modes were also determined. The open loop flutter speed was measured at 580 inches per second. The analytical prediction was conservative by 3.5%. Closed loop flutter testing was performed and a flutter speed of 697 inches per second was obtained. This represents a 20% improvement from the open loop case. The analytical prediction of closed loop flutter speed was conservative by 7.6%.

It is recommended that further research be performed in the area of controlling the aeroelastic responses of a vehicle utilizing piezoelectric actuators. A more realistic and complex model needs to be designed which incorporates strain-actuating elements within the airfoil design. The concept has been proven to work, however, it has not yet been shown to be workable in terms of real aircraft. Experiments on a larger scale are now called for.

Flutter suppression is not the only aeroelastic application which may call for secondary actuators made of adaptive materials. Load alleviation which is currently performed by aerodynamic control surfaces may prove to be an ideal application for localized strain actuation. By actuating adaptive material elements, local strains could be produced which would try to counter the loads induced within the structure during maneuvering. This has the potential of extending the service life of aircraft which traditionally undergo high g-loading and also expanding operational limits.

The concept of an adaptive material mission-adaptive wing is worthy of investigation. The hydraulic problems encountered on previous attempts to create a wing which can be shape-optimized for various flight conditions would be eliminated, and perhaps replaced with electrical problems.

The applications for which adaptive material will be suitable in the future depend heavily on the researchers in the materials area. Ceramics, which were used in this investigation, are very fragile. Polymers are currently not capable of generating the strain levels required for actuating realistic structures. For piezoelectrics to move from the research arena into production, a more resilient substance than ceramics or a means to protect the ceramics need to be developed.

References

[1.1] Sandford, M.C., Abel, I., and Gray, D.L., *Development and Demonstration of a Flutter Suppression System Using Active Controls*, NASA TR R-450, December, 1975.

[1.2] Newsom, J.R., and Abel, I., *Active Control of Aeroelastic Response*, NASA TM-83179, July, 1981.

[1.3] Newsom, J.R., and Pototzky, A.S., *Analysis and Flight Data for a Drone Aircraft with Active Flutter Suppression*, Journal of Aircraft, Vol 19, Number 11, November 1982.

[1.4] Waszak, M.R., and Srinathkumar, S., *Active Flutter Suppression: Control System Design and Experimental Validation*, AIAA Paper No. 91-2629, August 1991.

[1.5] Hwang, W.C., *Demonstration of Active Wing / Store Flutter Suppression Systems*, AFFD; TR-78-65, June 1980.

[1.6] Ehlers, S.M., *Aeroelastic Behavior of an Adaptive Lifting Surface*, PhD Dissertation, Purdue University, 1991.

[1.7] Anderson, E.H., and Crawley, E.F., *Piezoceramic Actuation of One- and Two-Dimensional Structures*, Space Systems Laboratory, Massachusetts Institute of Technology, Cambridge, MA.

[1.8] Scott, R.C., *Control of Flutter Using Adaptive Materials*, M.S. Thesis, Purdue University, May 1990.

[1.9] Spangler, R.L., *Piezoelectric Actuators for Helicopter Rotor Control*, M.S. Thesis, Massachusetts Institute of Technology, February, 1989.

[1.10] Barrett, R., *Intelligent Rotor Blade Actuation through Directionally Attached Piezoelectric Crystals*, 1990.

[1.11] Preumont, A., Dufour, J-P., and Malekian, C., *Active Damping by a Local Force Feedback with Piezoelectric Actuators*, Proceedings of the AIAA/ASME/ASCE/AHS/ASC 32nd Structure, Structural Dynamics, and Materials Conference, Part III pp 1879-1887 Baltimore MD, April 1991.

[1.12] Lefebvre, S., *Active Control of Interior Noise Using Piezoelectric Actuators in a Large Scale Composite Fuselage Model*, M.S. Thesis, Virginia Polytechnic Institute & State University, June 1991.

[1.13] Gibbs, G.P., and Fuller, C.R., *Experiments on Active Control of Vibrational Power Flow Using Piezoceramic Actuators and Sensors*, Proceedings of the AIAA/ASME/ASCE/AHS/ASC 31st Structure, Structural Dynamics, and Materials Conference, Part III pp 2331-2339, Long Beach, CA, April 1990.

[1.14] deLuis, J., and Crawley, E.F., *Experimental Results of Active Control on a Prototype Intelligent Structure*, Proceedings of the AIAA/ASME/ASCE/AHS/ASC 31st Structure, Structural Dynamics, and Materials Conference, Part III pp 2340-2350, Long Beach, CA, April 1990.

[1.15] Weisshaar, T.A., and Ehlers, S.M., *Adaptive Static and Dynamic Aeroelastic Design*, Proceedings of the 1991 International Forum on Aeroelasticity and Structural Dynamics, Workshop on Smart Material Systems and Structures, Aachen Deutschland, June 1991.

[1.16] Ehlers, S.M., and Weisshaar, T.A., *Static Aeroelastic Behavior of an Adaptive Laminated Piezoelectric Composite Wing*, Proceedings of the AIAA/ASME/ASCE/AHS/ASC 31st Structure, Structural Dynamics, and Materials Conference, Part III pp 2340-2350, Long Beach, CA, April 1990.

[1.17] Lazarus, K.B., Crawley, E.F., and Lin, C.Y., *Fundamental Mechanisms of Aeroelastic Control with Control Surface and Strain Actuation*, Proceedings of the AIAA/ASME/ASCE/AHS/ASC 32nd Structure, Structural Dynamics, and Materials Conference, Part III pp 1817-1831, Baltimore MD, April 1991.

[2.1] Mason, W.P., *Piezoelectricity, Its History and Applications*, Journal of the Acoustical Society of America, Volume 70, Number 6,pp 1561-1566, December 1981.

[2.2] Product Information Catalog, PiezoSystems Solid State Motion Technologies, May 1990.

[3.1] Dunn, H.J., *Experimental Results of Active Control on a Large Structure to Suppress Vibration*, Proceedings AIAA GNC Conference, New Orleans, LA, 1991.

[4.1] Chia, C-Y., *Nonlinear Analysis of Plates*, McGraw-Hill International Book Company, 1980.

[4.2] Yates, C.E., Course Notes for Aeroelasticity II, George Washington University, 1990.

[4.3] Tiffany, S.H., and Adams, W.M.,Jr, *Nonlinear Programming Extensions to Rational Function Approximation Methods for Unsteady Aerodynamic Forces*, NASA Technical Paper 2776, July, 1988.

[4.4] Mukhopadhyay, V., Newsom, J.R., and Abel, I., *A Method for Obtaining Reduced-Order Control Laws for High-Order Systems Using Optimization Techniques*, NASA Technical Paper 1876, 1981.

[4.5] Kohn, M.C., *Practical Numerical Methods: Algorithms and Programs*, McGraw-Hill Publishing Company, 1987.

[4.6] Franklin, G.F., Powell, J.D., and Emani-Naeini, A., *Feedback Control of Dynamic Systems*, Addison-Wesley Publishing Company, June 1986.

[4.7] Zienkiewicz, O.C., *The Finite Element Method*, 3rd edition, McGraw-Hill Book Company Limited, 1977.

[4.8] *MSC / NASTRAN User's Manual Version 65*, The MacNeal Schwendler Corporation, November, 1985.

[4.9] Roark, R.J., and Young, W.C., *Formulas for Stress and Strain*, 5th edition, McGraw-Hill International Book Company, 1975.

[4.10] Rodden, W.P., Giesing, J.P., and Kalman, T.P., *New Developments and Applications of the Subsonic Doublet-Lattice Method for Nonplanar Configurations*, AGARD Symposium on Unsteady Aerodynamics for Aeroelastic Analyses of Interfering Surfaces, Paper Number 4, November, 1970.

[4.11] Zeiler, T.A., *Aeroelastic Vehicle Analysis User's Manual*, (to be published).

[4.12] Hoadley, S.T., and Silva W.A., *User's Manual for the Interaction of Structures, Aerodynamics, and Controls Code*, version 4.1, (to be published).

[4.13] Longman, R.w., Juang, J-N., and Phan, M., *Input and Output Matrices in Modal Identification.*

[4.14] MatrixX Release Notes, 7.0, Integrated Systems, Incorporated, October, 1988.

[4.15] Matlab User's Manual, The MathWorks Incorporated, April 1989.

[4.16] Kuo, B.C., *Digital Control Systems*, Holt, Rinehart and Winston, Inc, 1980.

[5.1] Weisshaar, T.A., Course Notes from Aeroelasticity, Purdue University, 1988.

[5.2] Adams, W.H., Jr., Tiffany, S.H., Newsom, J.R., and Peele, E.L., *STABCAR - A Program for Finding the Characteristic Roots of Systems Having Transcendental Stability Matrices*, NASA TP 2165, June 1984.

[5.3] Phillips, C.L. and Nagle, H.T., Jr. *Digital Control System Analysis and Design*, Prentice-Hall Incorporated, 1984.

Tables

	MASS (lbm)	CENTER OF GRAVITY DISTANCE AFT OF THE PIVOT POINT (inches)
Primary Wing Structure (includes pivot mechanism)	.072	0.0
Balsa Extension (includes adhesives)	.011	1.875
Aluminum Mass Ballast	.007	3.0
Total	.09	

Table 3.1 Measured Mass and Center of Gravity Locations for Wing Components

	MASS (lbm)	WIDTH (inches)	DIST (inches)	I_{cg} (lbm-in^2)	I_{pivot} (lbm-in^2)
Primary Wing	.072	2.0	0.0	.022	.022
Wing Extension	.011	3.25	1.875	.0097	.0487
Mass Ballast	.007	.5	3.0	.00014	.06314

Table 3.2 Inertia Calculations for Wing Components

	MASS (lbm)	CENTER OF GRAVITY DISTANCE AFT OF THE PIVOT POINT (inches)
Primary Wing Structure (includes pivot mechanism)	.072	0.0
Balsa Extension (includes adhesives)	.011	1.875
Aluminum Mass Ballast	.007	3.0
Total	.09	

Table 3.1 Measured Mass and Center of Gravity Locations for Wing Components

	MASS (lbm)	WIDTH (inches)	DIST (inches)	I_{cg} (lbm-in^2)	I_{pivot} (lbm-in^2)
Primary Wing	.072	2.0	0.0	.022	.022
Wing Extension	.011	3.25	1.875	.0097	.0487
Mass Ballast	.007	.5	3.0	.00014	.06314

Table 3.2 Inertia Calculations for Wing Components

```
//
//eom.mat
//
// Procedure file used to generate open loop equations of
motion
//
// Gamma is the finite difference program output matrix
which
//       calculates the piezoelectric structural influence
//
//    Cstrain is the second derivatives of each of the
modeshapes
//       with respect to lengthwise coordinate
//
// Physical parameters
chord=4.5
rho=.11468e-6
d31=-6.35e-9
qbar=.5*rho*v**2
//
// Structural stiffness, damping and mass
//
omega=[7.8;10.89]
freq=2*pi*omega
dsi=[.017  .055]
ms=[eye(2)]
ks=diag(freq.**2)*ms
ds=diag(dsi)*diag(freq)
//
// Aerodynamic stiffness, damping and mass
//
ma=qbar*(chord/2/v)**2 *a2
da=qbar * chord/2/v * a1
ka=qbar*a0
//
// Combining aerodynamic and structural matrices
//
m=ms+ma
minv=inv(m)
d=ds+da
k=ks+ka
//
// Assembling the state space matrices
//
a=[0*ones(2,2) eye(2,2); -1*minv*k -1*minv*d]
//ba=[0;0;-1*qbar*minv*a0c]
bs=-1*d31*minv*gamma
b=1.2*[0;0;bs]
zbar=.008
c=-1.3*zbar*cstrain
s=[a b;c 0*ones(2,1)]
```

Table 4.1 Procedure File for Assembling the Equations of Motion

	PLUNGE MODE FREQUENCY (Hz)	PITCH MODE FREQUENCY (Hz)
without Piezoelectric Plates		
Beam Theory	7.2	6.7 (cantilever) 13.4 (guided)
Finite Element Model	6.6	9.2 (cantilever)
Finite Element Model	6.8	10.6 (combined)
with Piezoelectric Plates		
Finite Element Model	7.8	10.9

Table 5.1 Analytical Predictions of Natural Frequencies with and without Piezoelectric Actuators

DESCR	ANALYSIS PITCH FREQUENCY (Hz)	ANALYSIS PLUNGE FREQUENCY (Hz)
primary wing	25.78	8.96
w/ wing ext only	13.29	8.38
.005 lbm ballast	11.39	7.99
.007	10.86	7.79
.009	10.65	7.61
.011	10.41	7.40

Table 5.2 Influence of Mass Ballast on Analytical Predictions of Natural Frequencies

PIEZO PLACEMENT Distance from Root to Edge of Piezo (in)	PLUNGE MODE FREQUENCY (Hz)	PITCH MODE FREQUENCY (Hz)	MODEL DEFLECTION (inches x 10^5)
no piezo present	7.02	12.6	0
.25	7.77	12.7	-9.21
1.25	7.26	12.6	-5.69
2.25	7.02	12.5	-1.54
3.25	7.02	12.5	2.59
4.25	7.3	12.6	6.77
5.25	7.75	12.6	9.47

Table 5.3 Results of Study to Determine Actuator Placement

	ANALYSIS	EXPERIMENT (uncoupled)
primary wing	25.78	
w/ wing ext only	13.29	12.8
.005 lbm ballast	11.39	10.4
.007	10.86	9.4
.009	10.65	no data
.011	10.41	8.25

Table 6.1 Influence of Mass Ballast on the Pitch Freuqncy

	PLUNGE MODE FREQUENCY (Hz)	PITCH MODE FREQUENCY (Hz)
without Piezoelectric Plates		
Finite Element Model	6.8	10.6 (combined)
Ground Vibration Test	6.9	12.3
with Piezoelectric Plates		
Finite Element Model	7.8	10.9
System Identification	7.9	11.1

Table 6.2 Natural Frequencies with and without Piezoelectric Actuators- Comparison of Analytical and Experimental Results

Velocity (inches / second)	Control Energy
580	122.8
590	172.1
630	196.9
670	228.0
710	4888.3 (flutter encountered)

Table 6.3 Control Energy Required to Suppress Flutter for Increasing Velocity

Figures

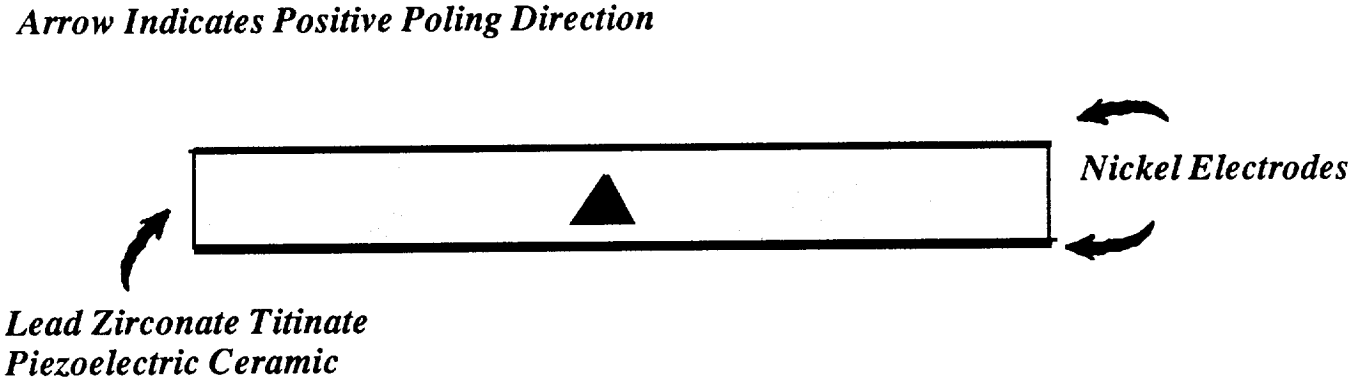

Figure 2.1 Electrode Placement on Piezoelectric Plate

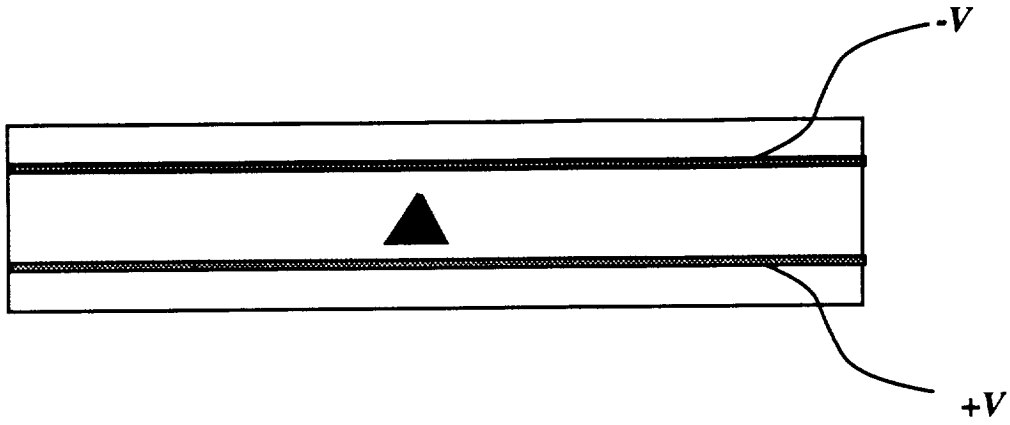

Figure 2.2 Thickening Effect (d33 effect)

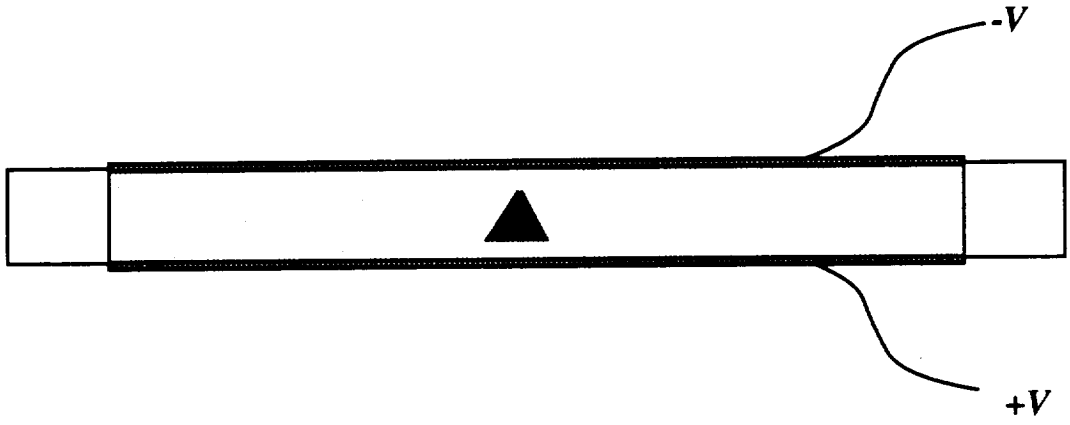

Figure 2.3 Lengthening Effect (d31, d32 effect)

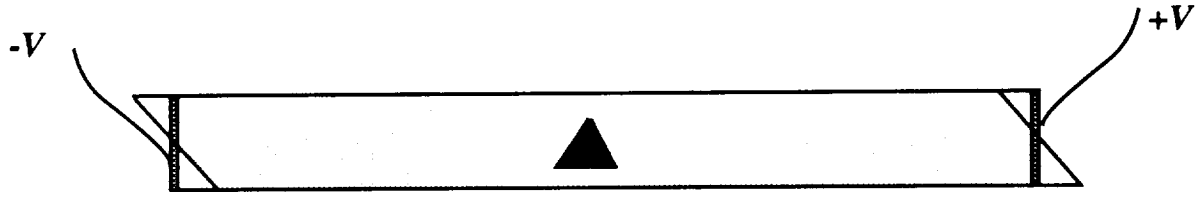

Figure 2.4 Shearing Effect (d15 effect)

Utilizes the d31 effect

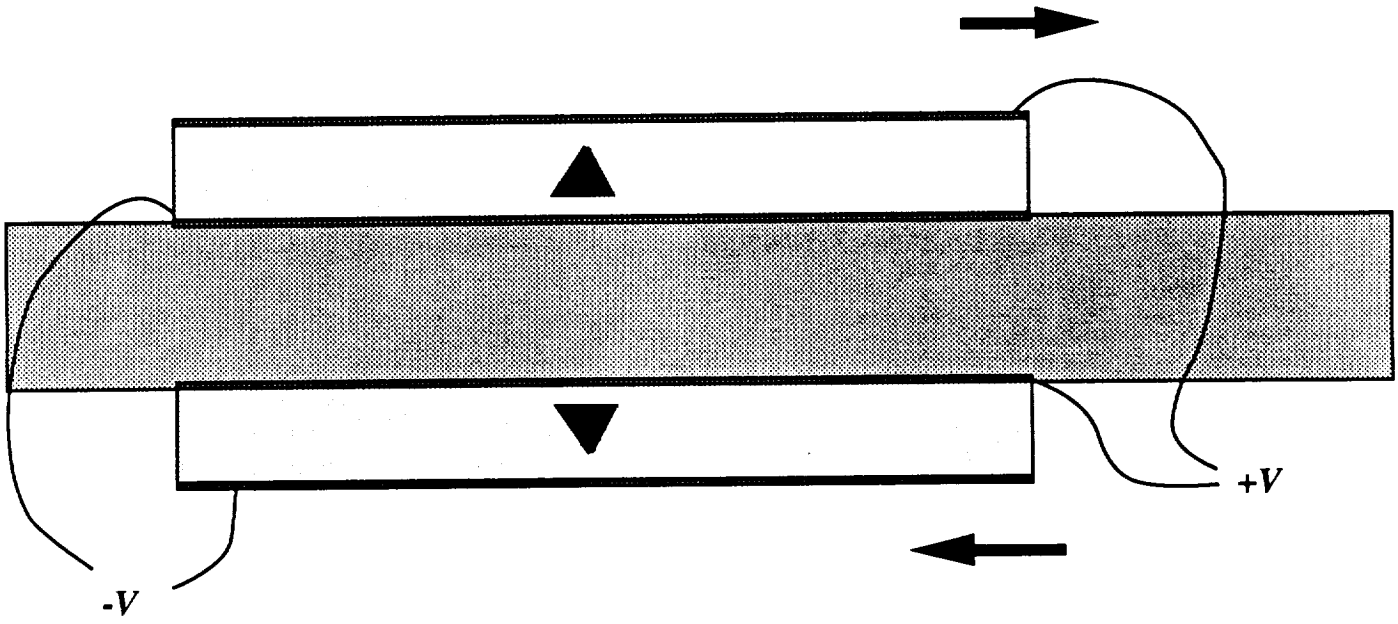

for the Voltage Polarity Shown:

Top Layer Expands in In-Plane Directions

Bottom Layer Contracts in In-Plane Directions

Results in Right End Bending Downward

Figure 2.5 Bimorph or Bender Configuration of Piezoelectric Plate Elements

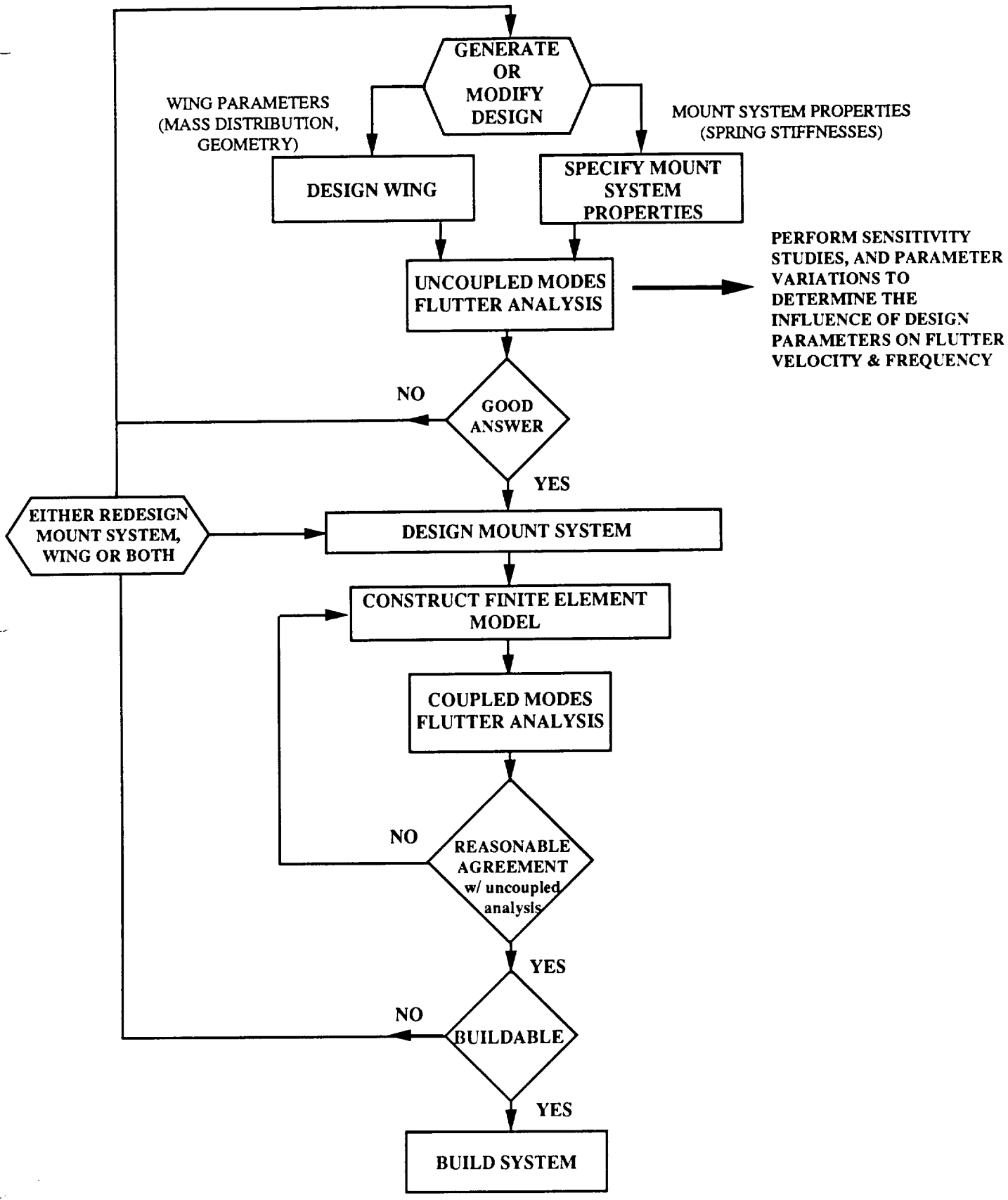

Figure 2.6 Flowchart of Aeroelastic Model Design Procedure

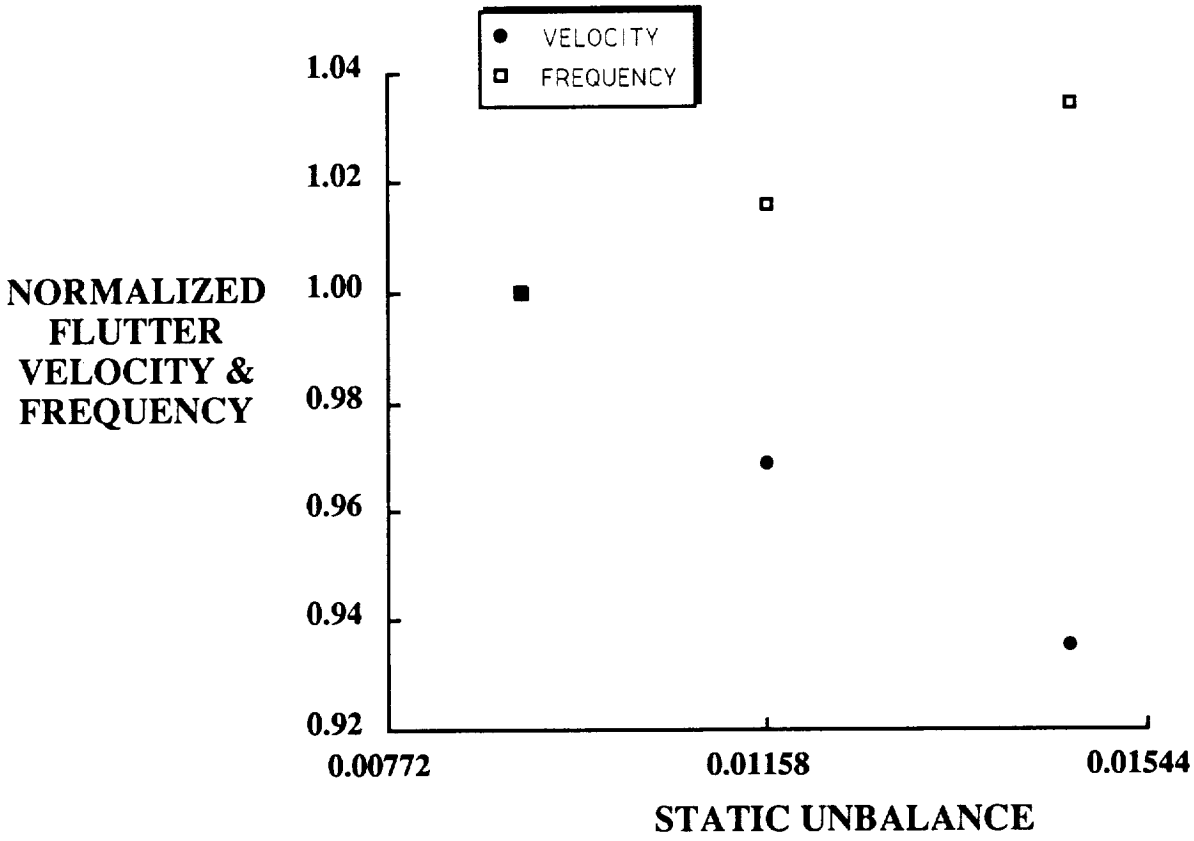

Figure 2.7 Influence of Static Unbalance on the Flutter Velocity and Frequency

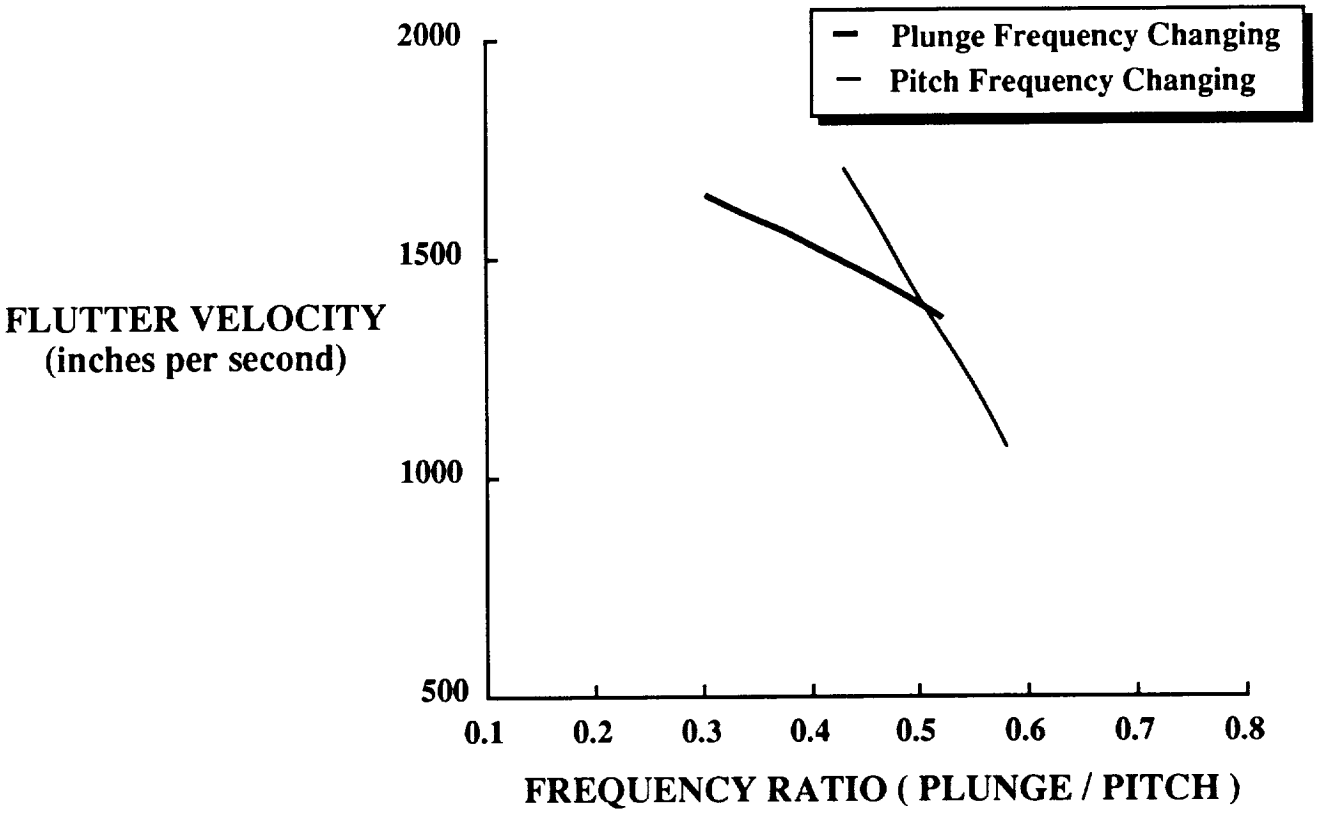

Figure 2.8 Influence of Frequency Ratio on the Flutter Velocity

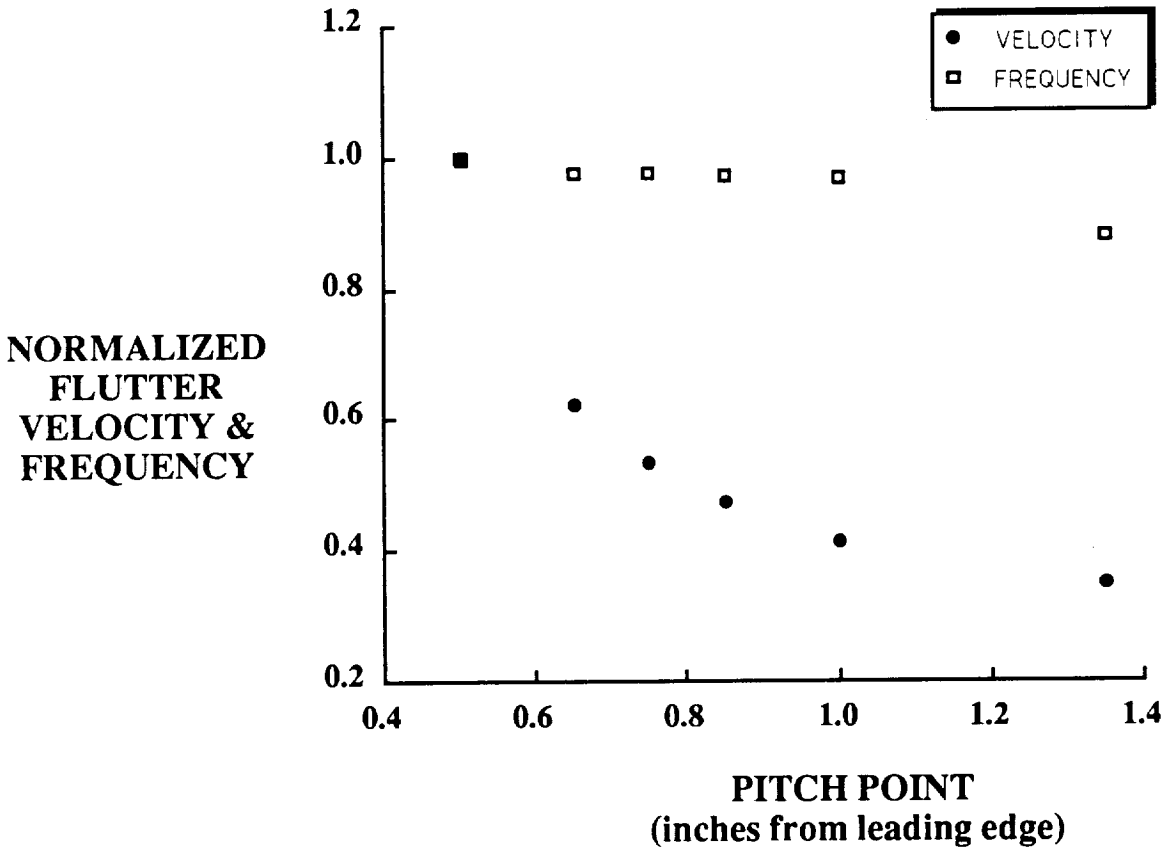

Figure 2.9 Influence of Pitch Pivot Location on the Flutter Velocity and Frequency

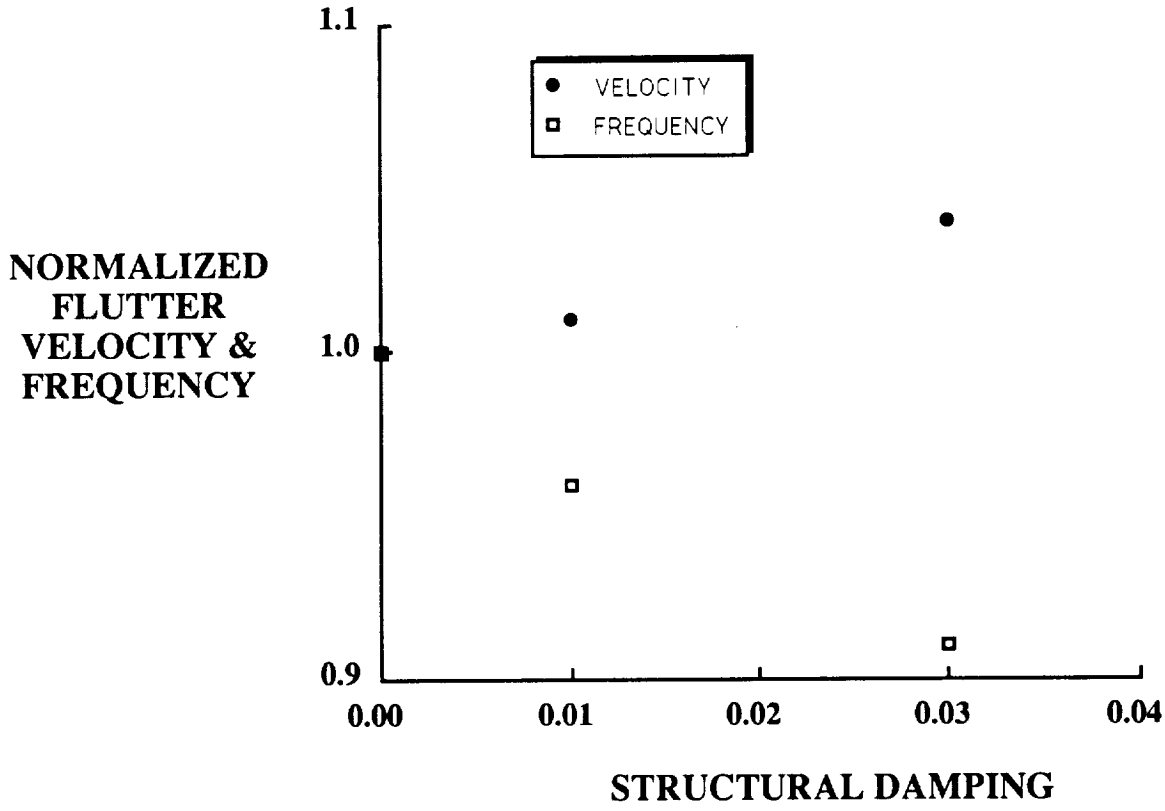

Figure 2.10 Influence of Structural Damping on the Flutter Velocity and Frequency

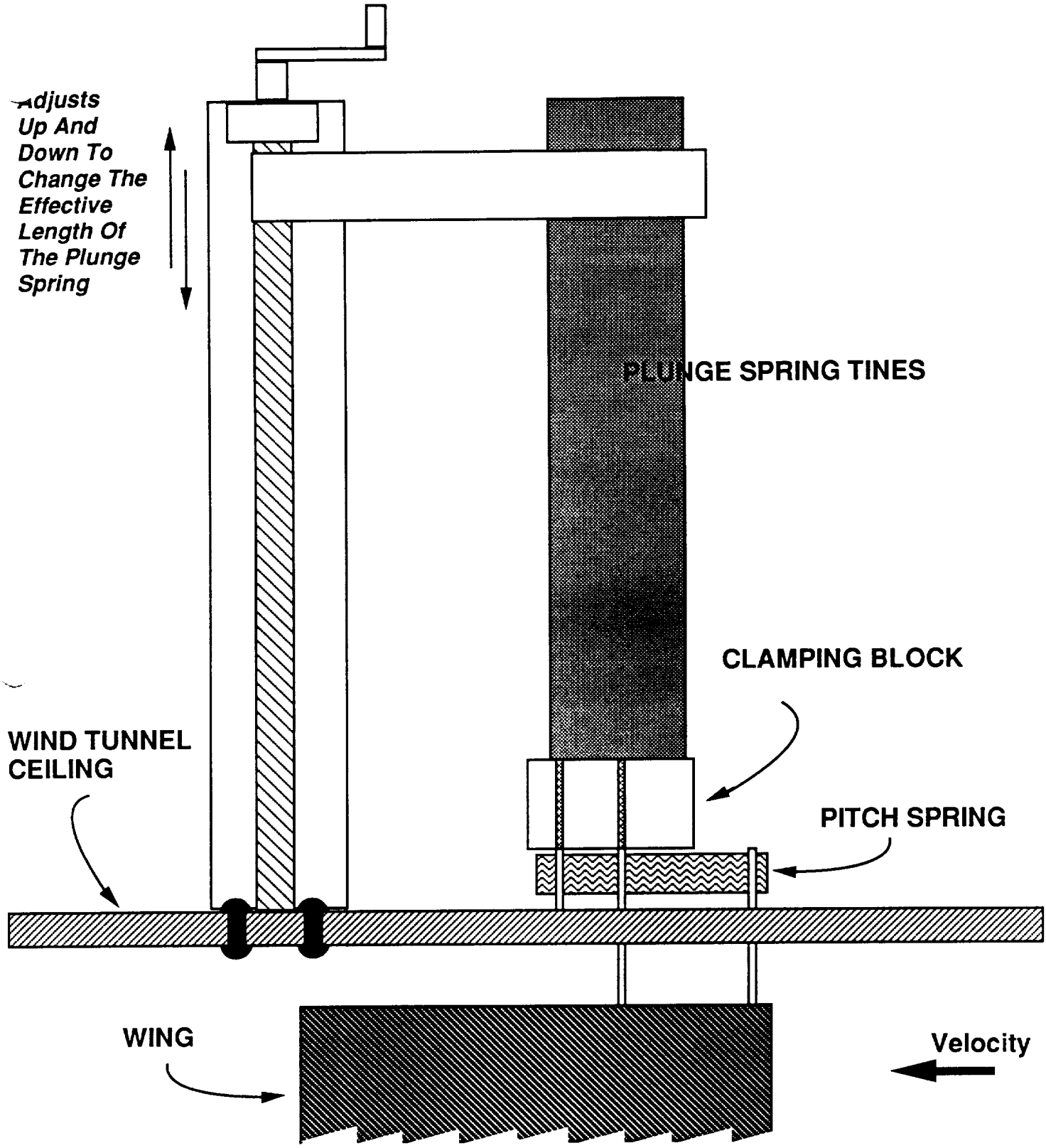

Figure 2.11 Wind Tunnel Mount System (not to scale)

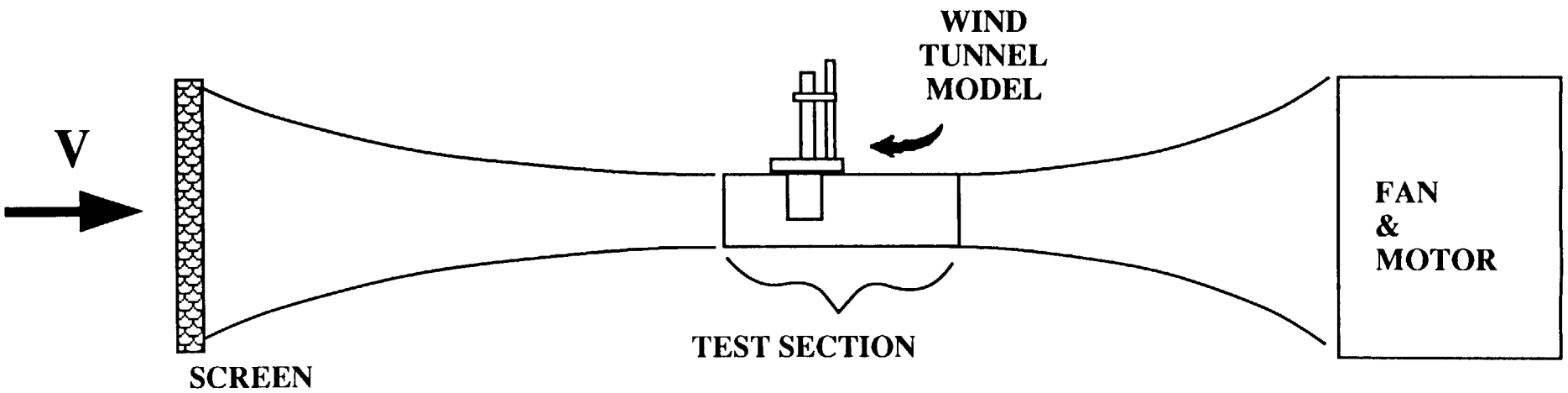

TEST SECTION: 6 INCHES BY 6 INCHES

CEILING MOUNTING FOR MODELS

LIMITS: VELOCITY -- 1500 in/s (85 mph)

DYNAMIC PRESSURE -- 0.13 psi

Figure 3.1 Schematic of Flutter Research and Experiment Device (FRED) Wind Tunnel

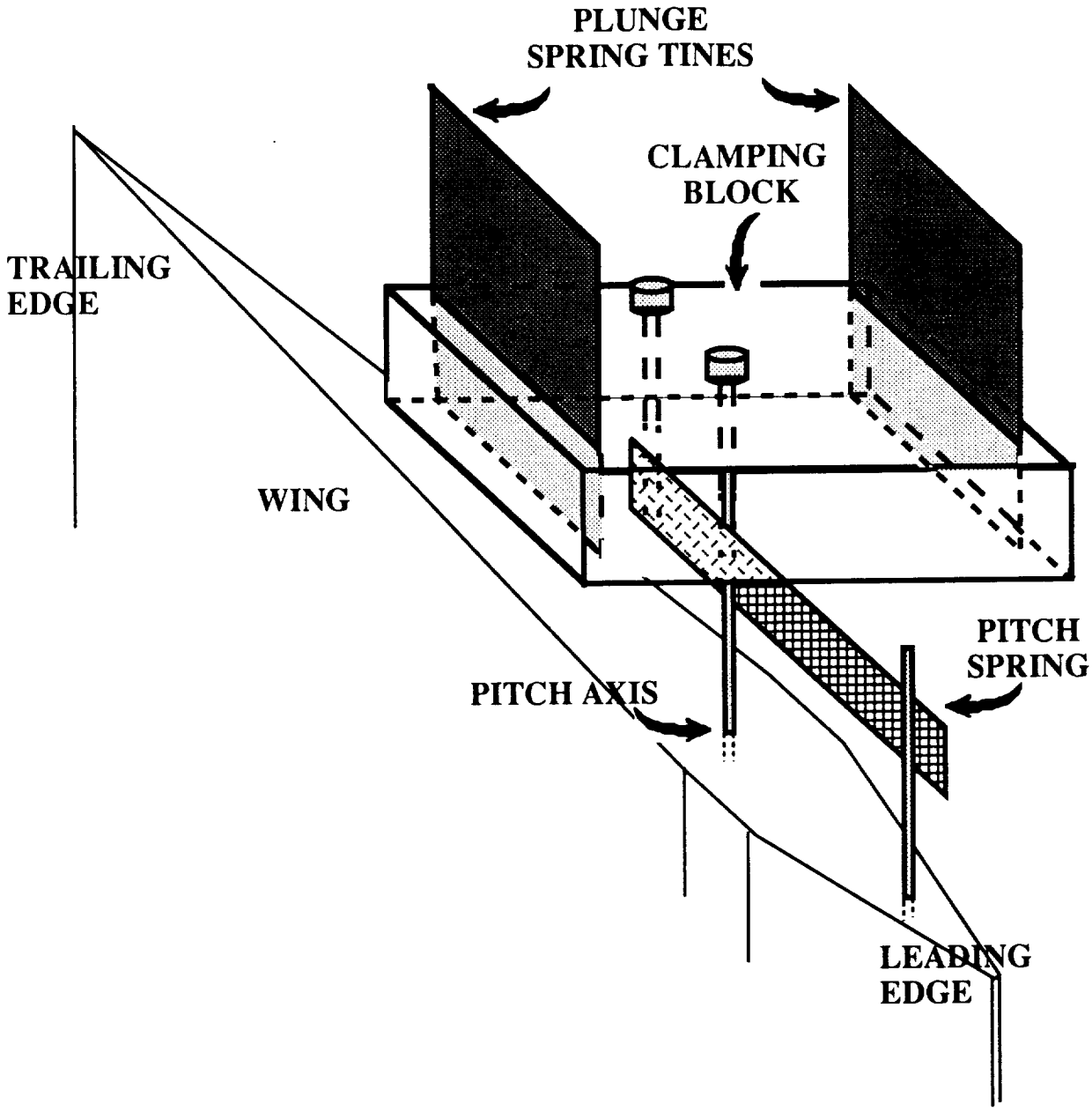

Figure 3.2 Mount System Closeup Interconnection Mechanism for the Plunge and Pitch Degrees of Freedom

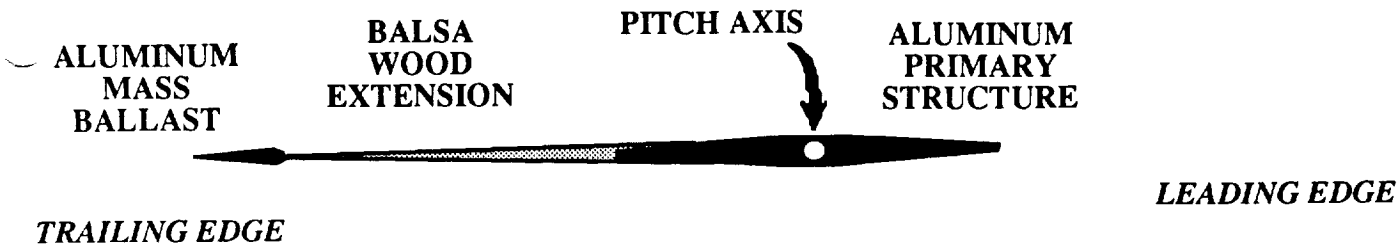

a) Cross-sectional View

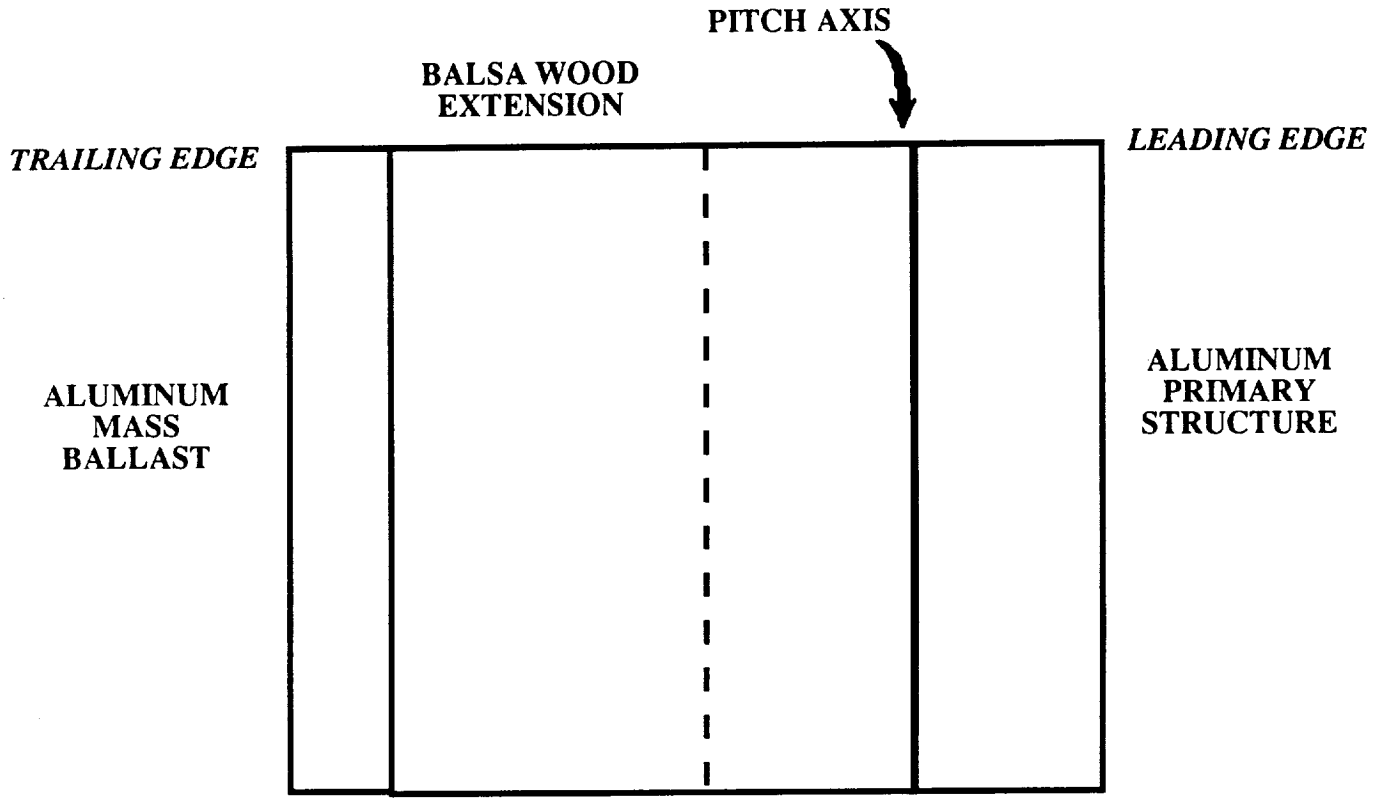

b) Planform View

Figure 3.3 Schematic of Wing

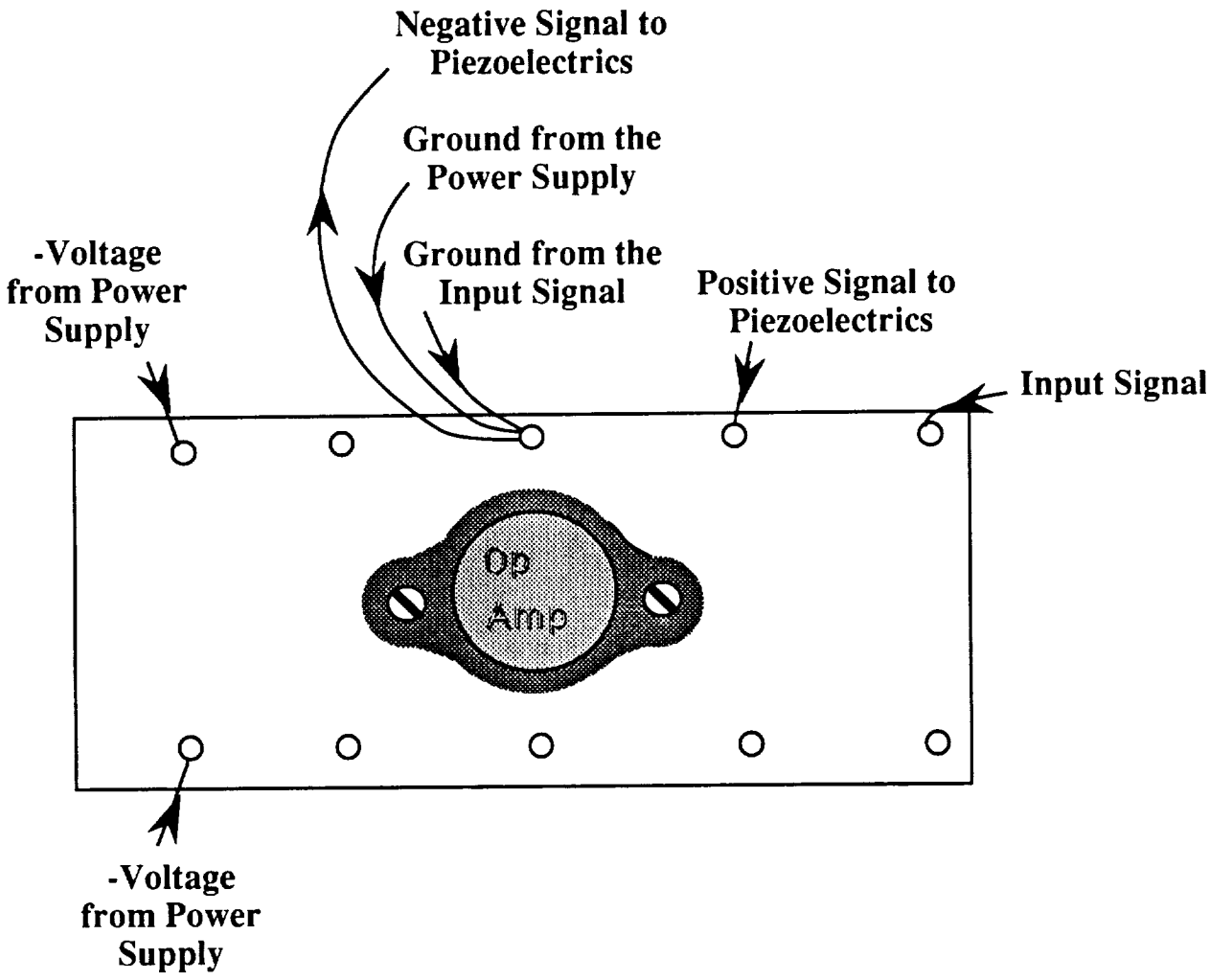

Figure 3.4 Operational Amplifier Connections

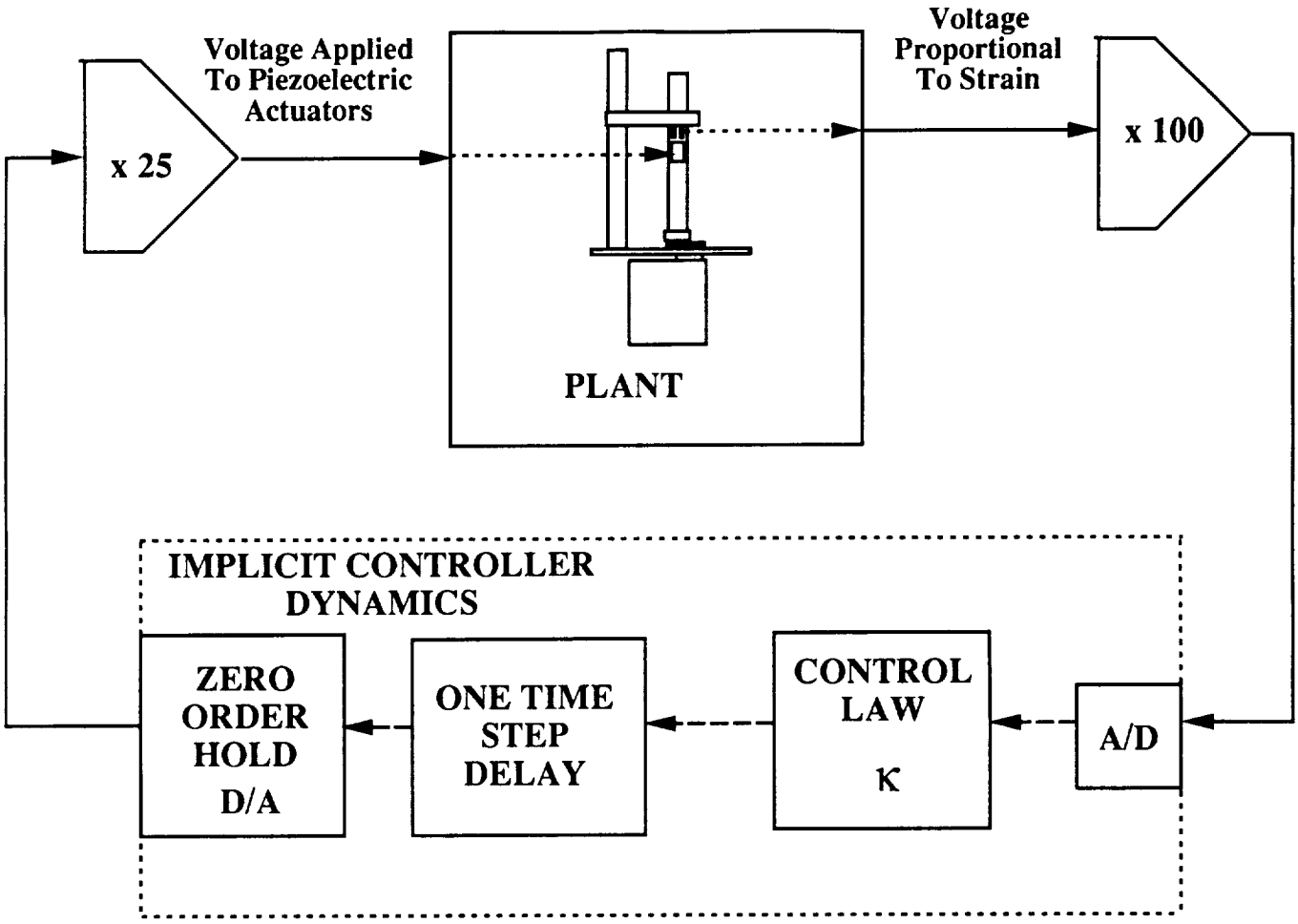

Figure 3.5 Block Diagram of Closed Loop System With Active Feedback

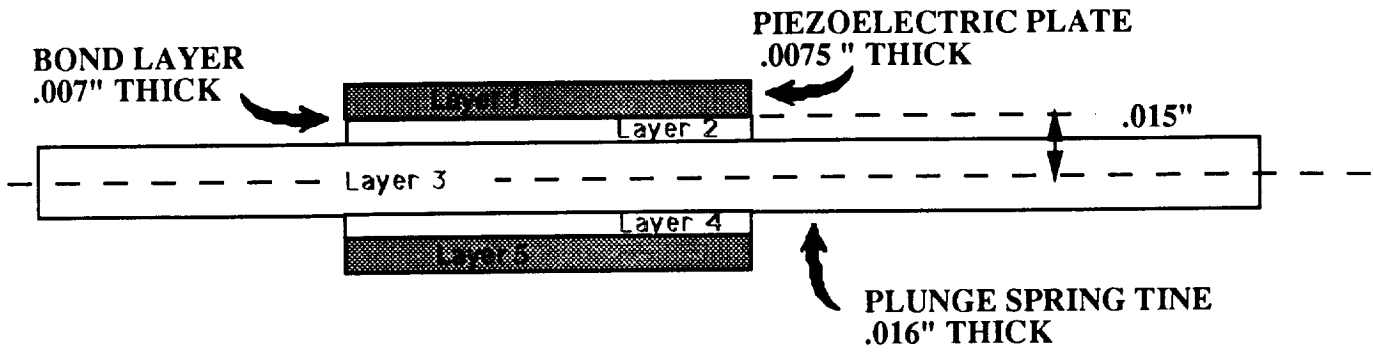

Figure 4.1 Actuator Attachment

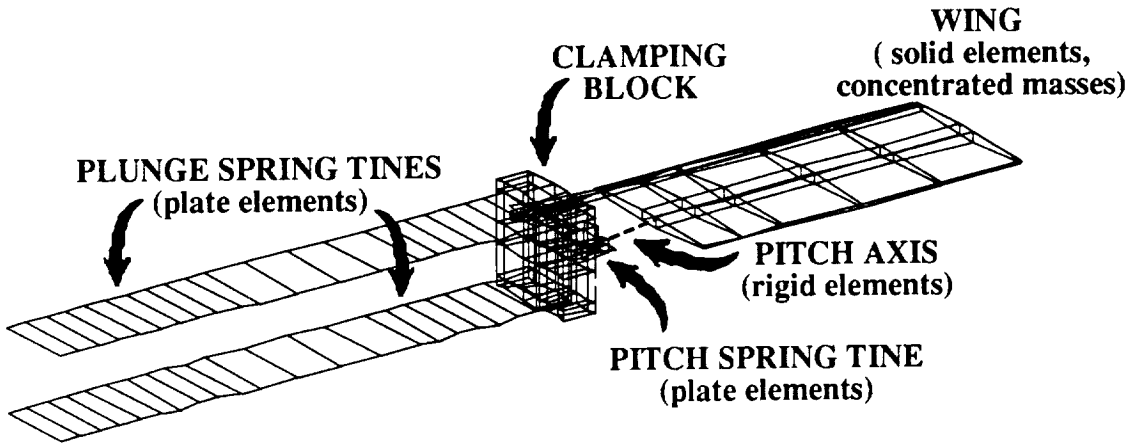

Figure 4.2 Finite Element Model

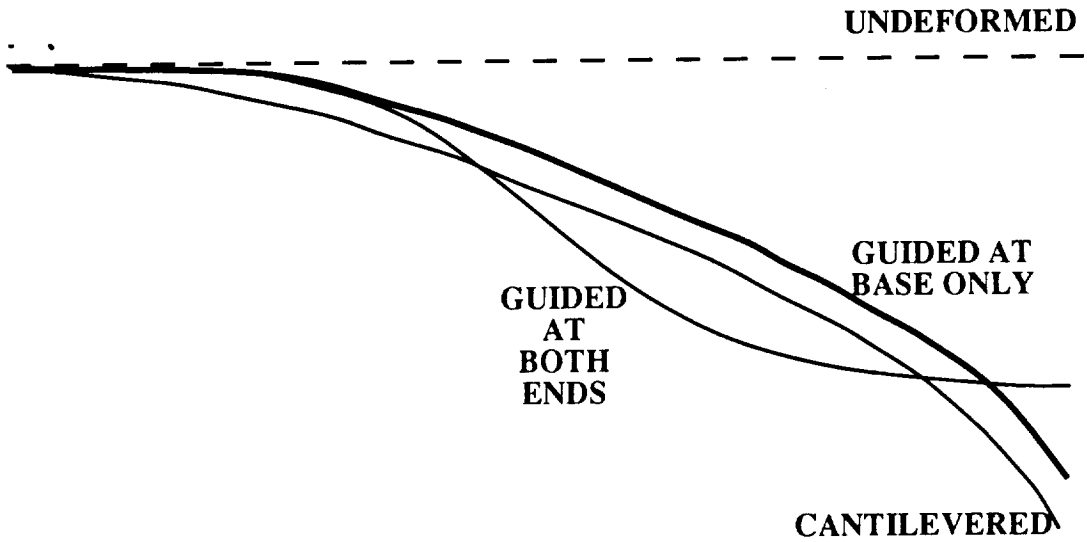

Figure 4.3 Sketch of Boundary Condition Influences on Deformation

1 INTERPOLATED TABULAR DATA

2 S-PLANE APPROXIMATION

Lift due to Plunge

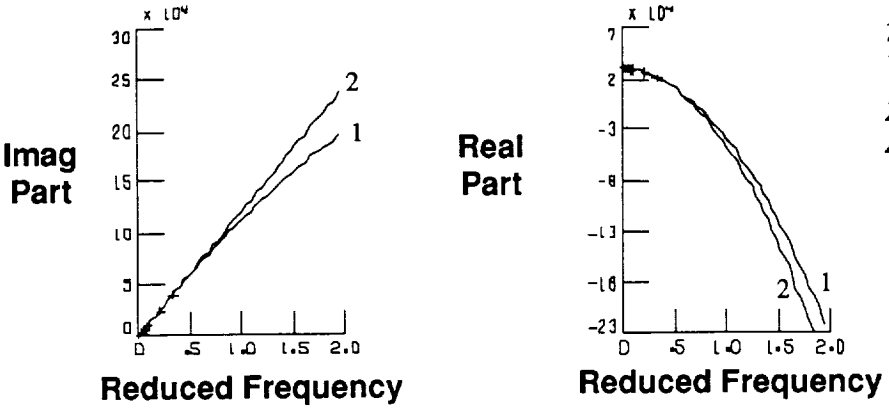

Moment due to Plunge

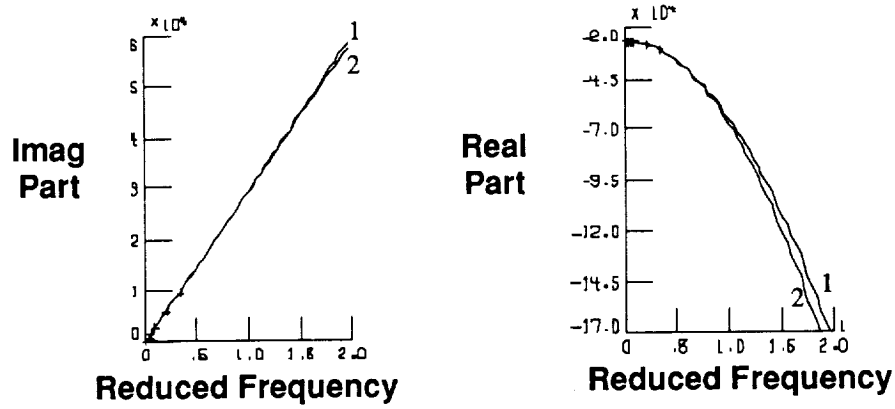

Lift due to Pitch

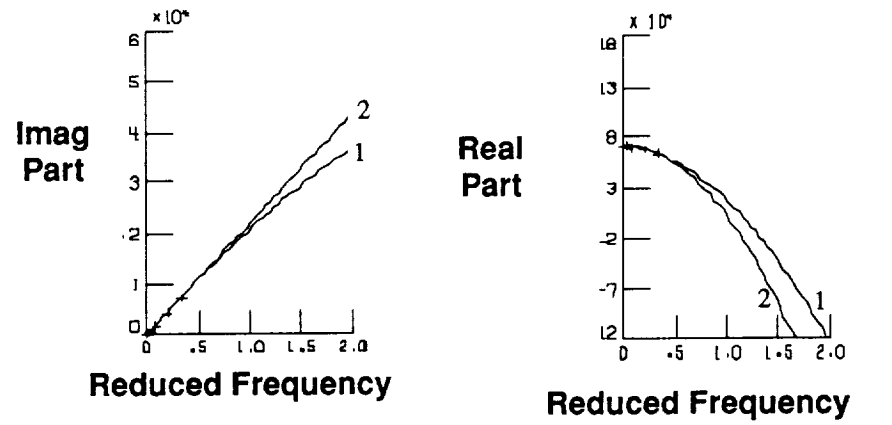

Moment due to Pitch

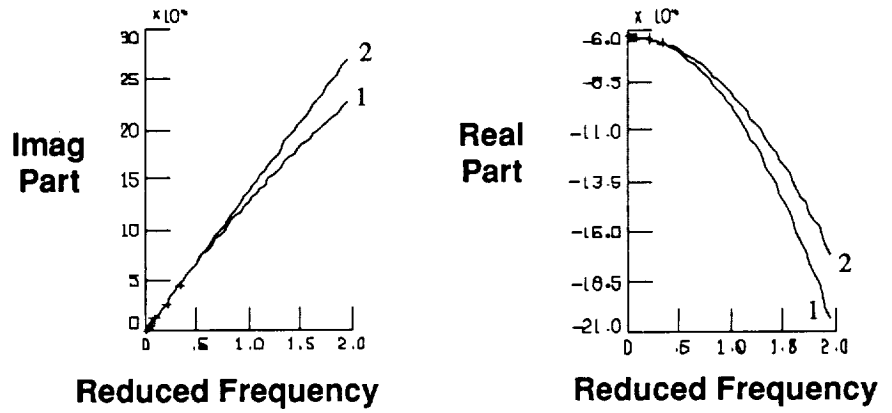

Figure 4.4 Rational Function Approximations to the Generalized Aerodynamic Forces

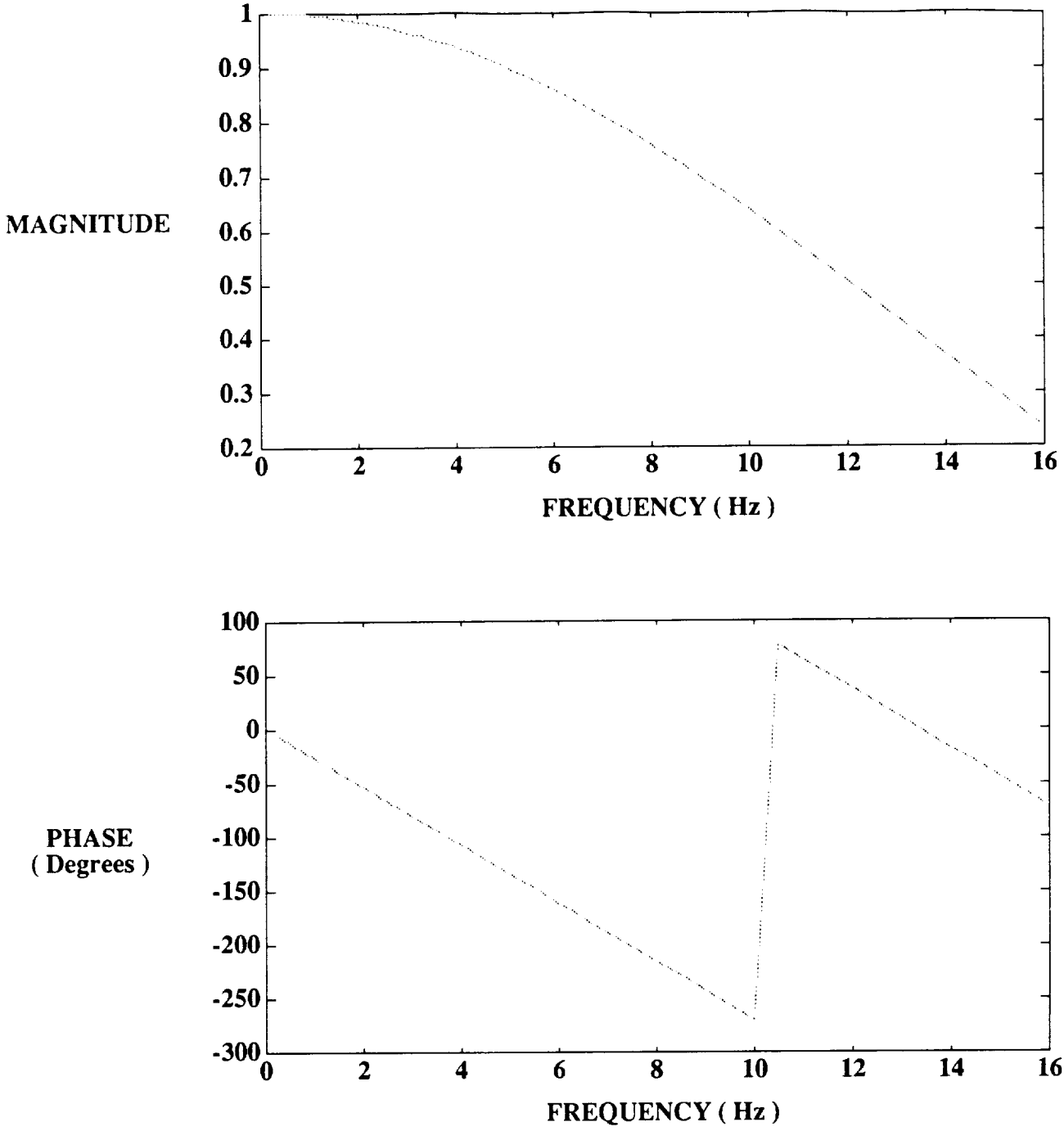

Figure 4.5 Frequency Response Plot of Implicit Controller Dynamics for 20 Hz Sample Rate (Time Delay and Zero Order Hold)

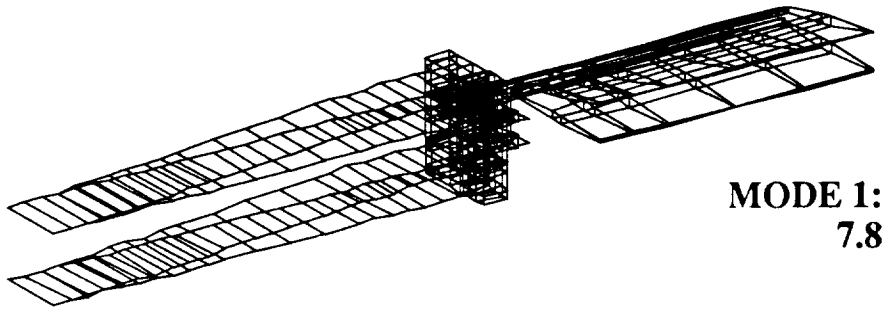

MODE 1: PLUNGE
7.8 Hz

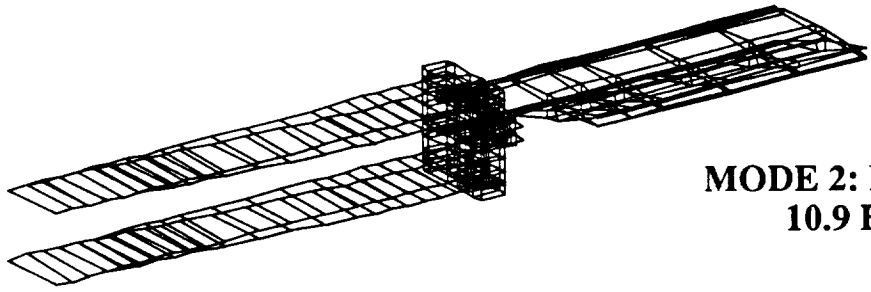

MODE 2: PITCH
10.9 Hz

Figure 5.1 Finite Element Analysis Vibration Mode Shapes

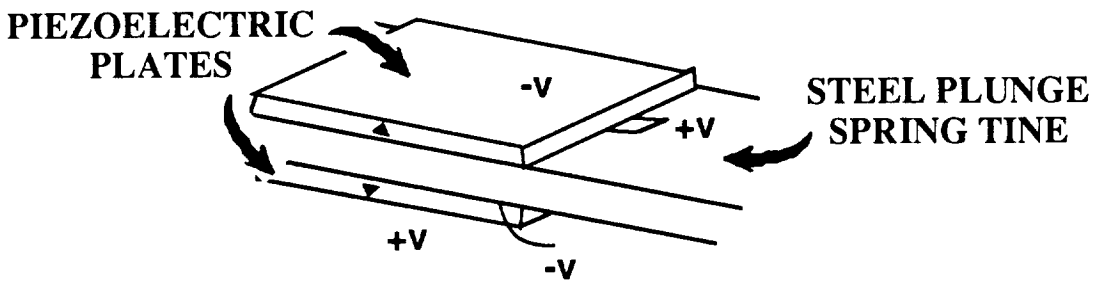

5.2 Piezoelectric Actuator Attachment to Plunge Spring Tine

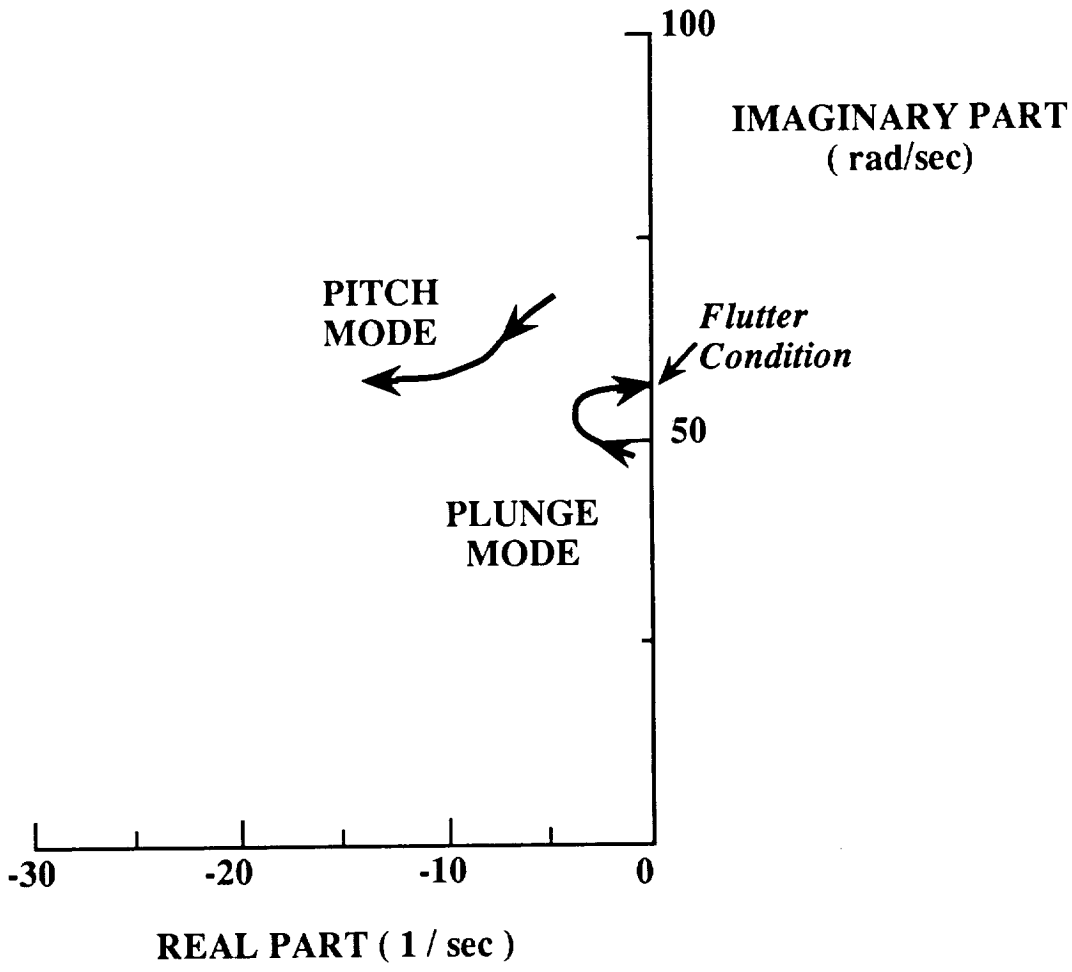

Figure 5.3 Root Locus- Eigenvalue Locations as Velocity is Varied

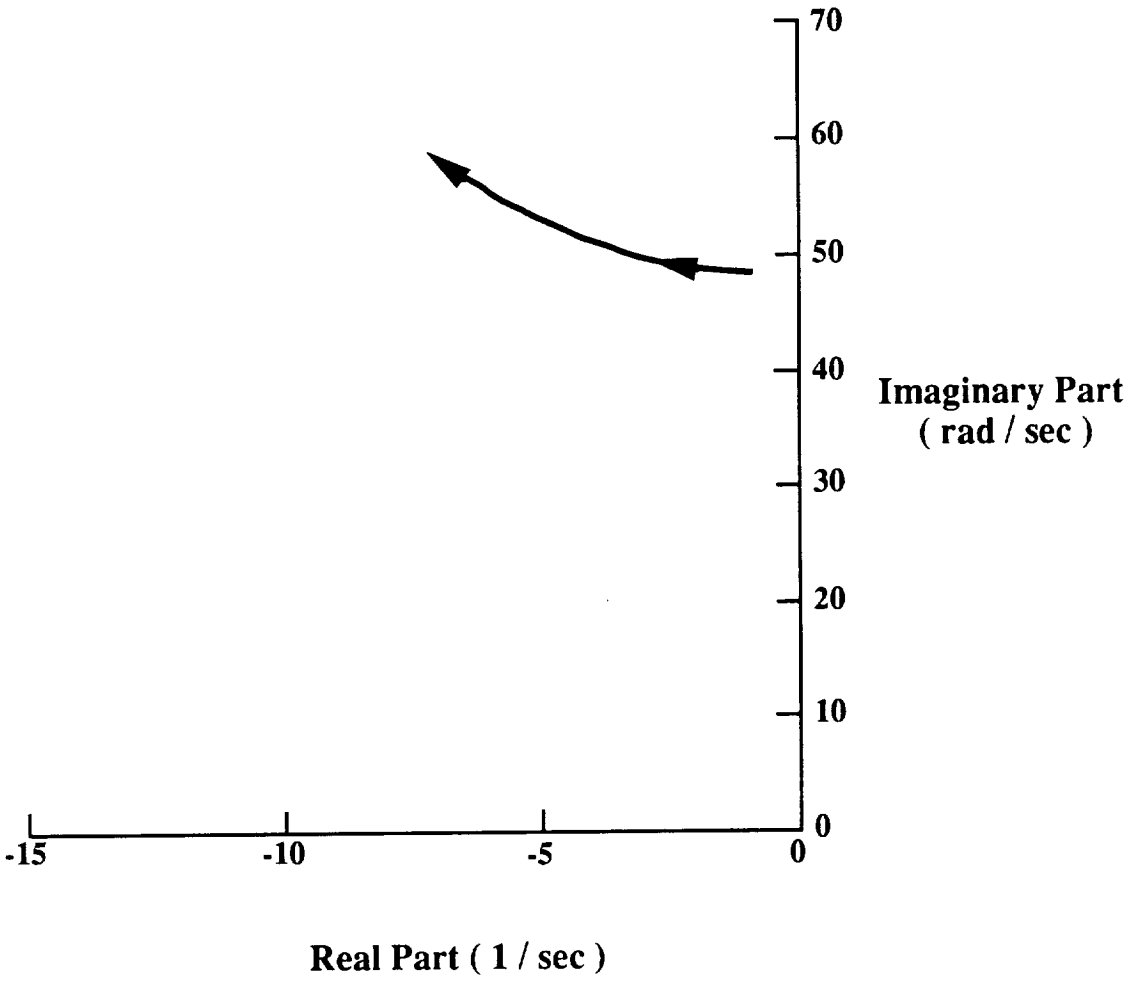

Figure 5.4 Velocity Root Locus Analysis of Plunge Mode Only

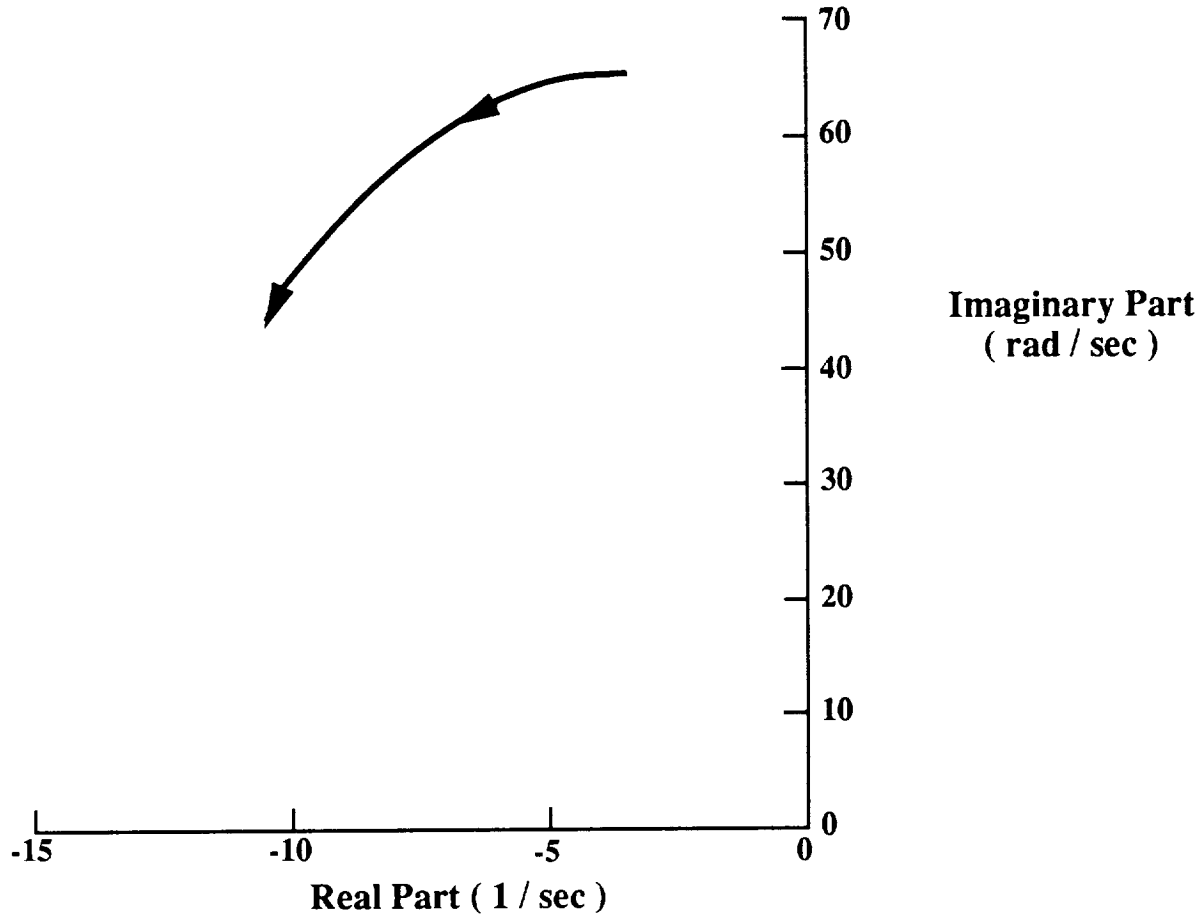

Figure 5.5 Velocity Root Locus Analysis of Pitch Mode Only

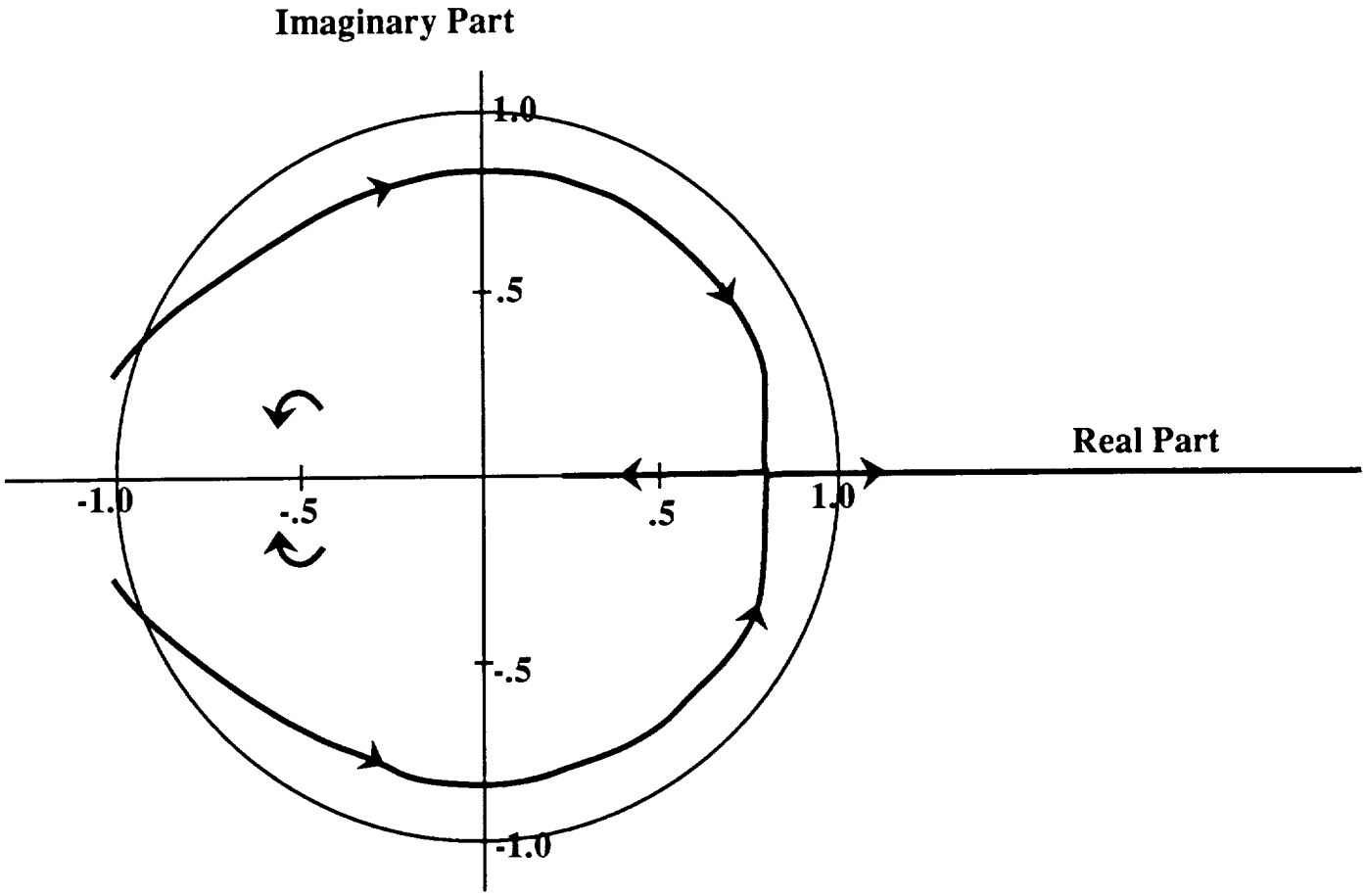

Figure 5.7 Gain Root Locus of the Discrete System at Open Loop Flutter, 580 inches per sec with Gains from 0 to 120

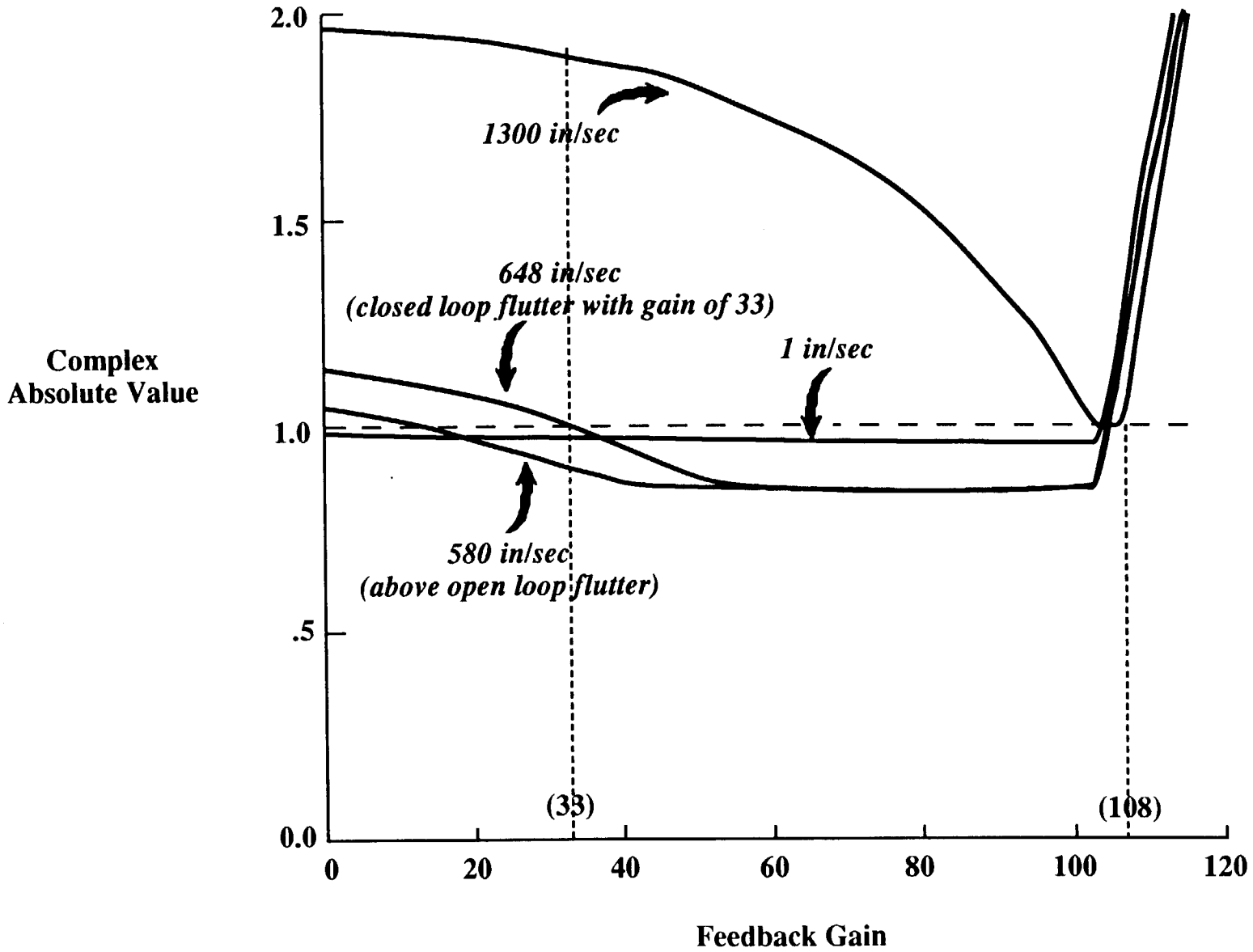

Figure 5.8 Maximum Complex Absolute Value as a Function of Feedback Gain for Various Airspeeds

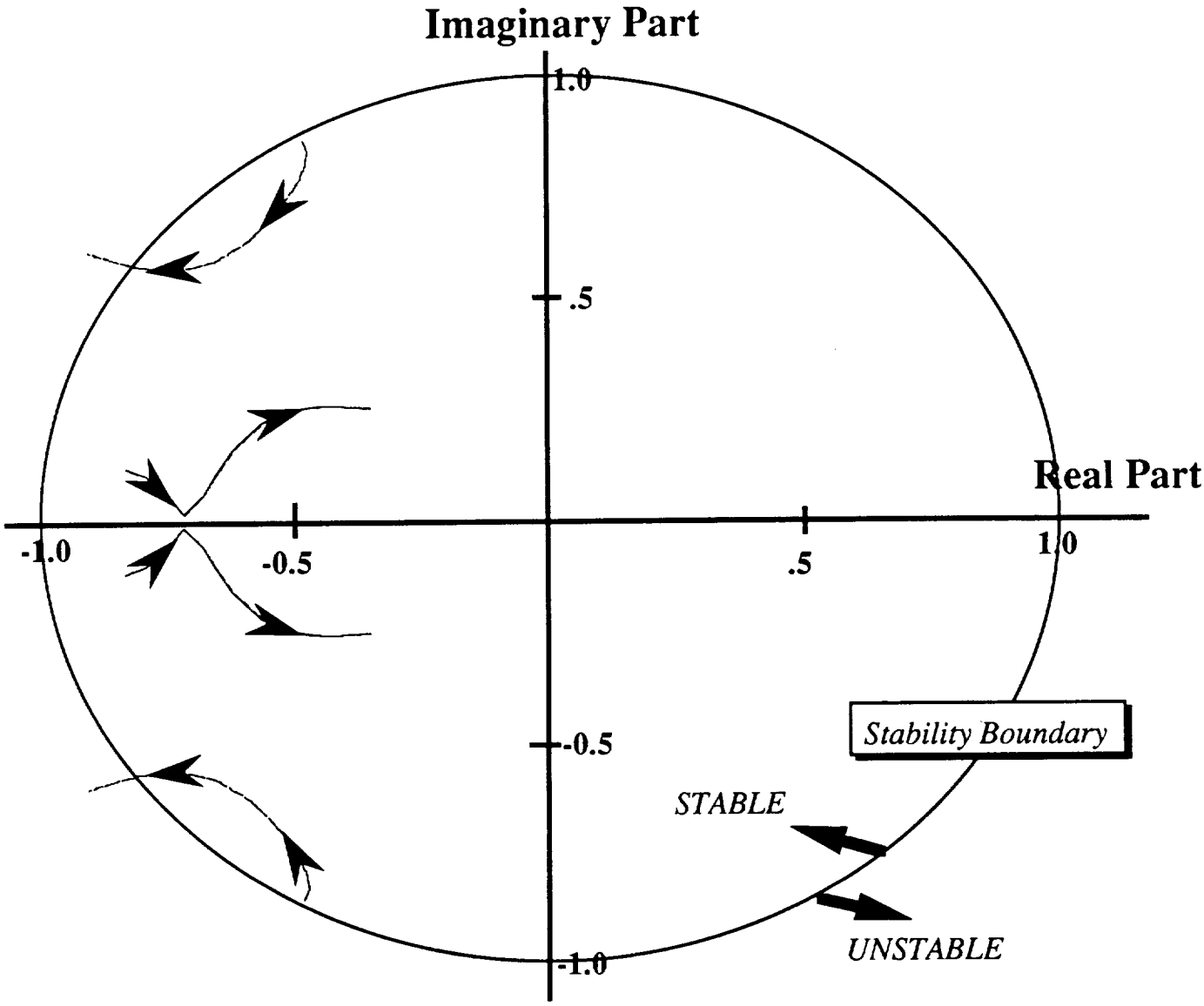

Figure 5.9 Discrete System Root Locus for Varying Velocity of the Closed Loop System with Feedback Gain of 33

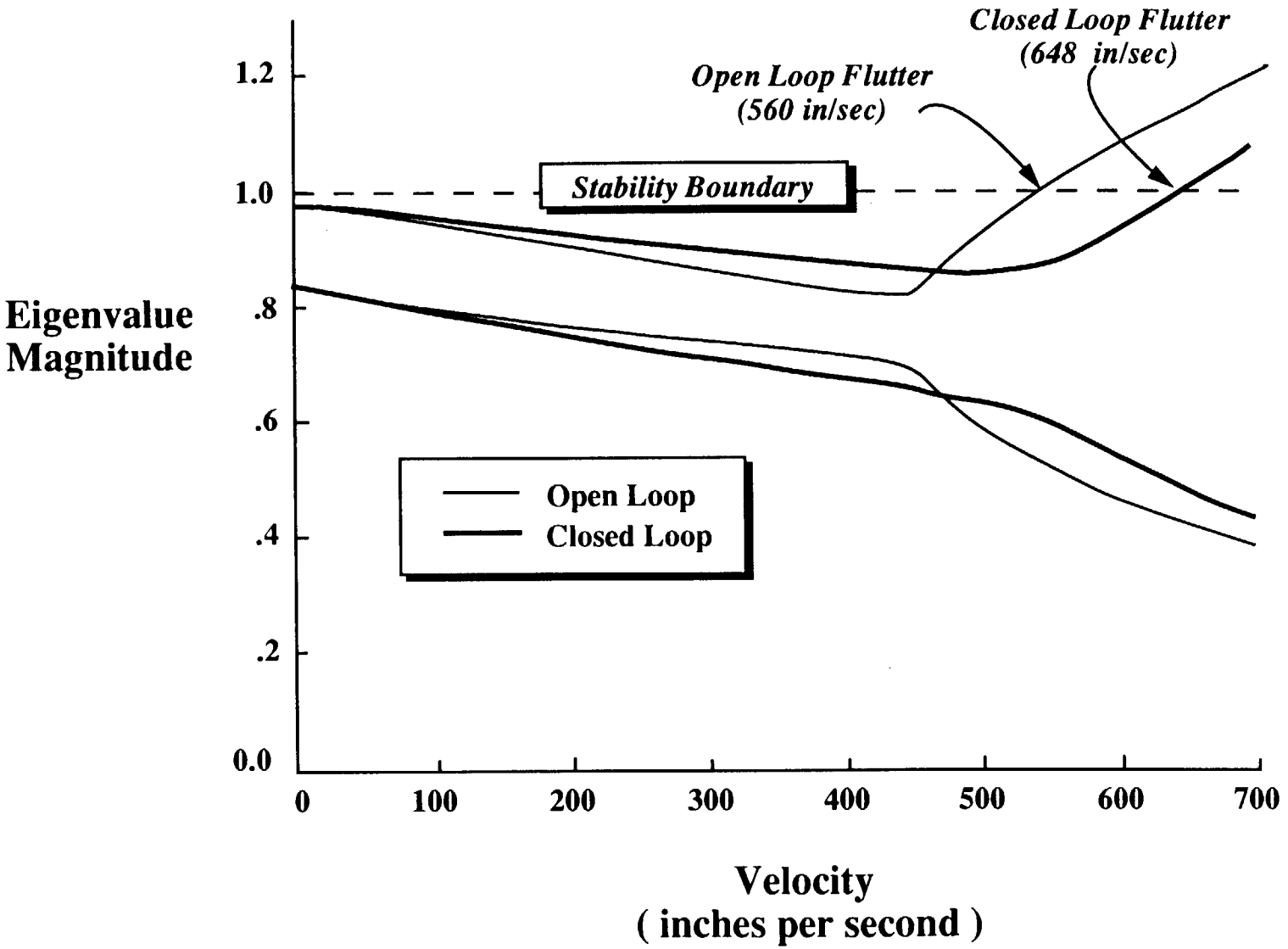

Figure 5.10 Open and Closed Loop Eigenvalue Magnitudes Versus Velocity with a 20 Hz Sample Rate, (Feedback Gain is 33)

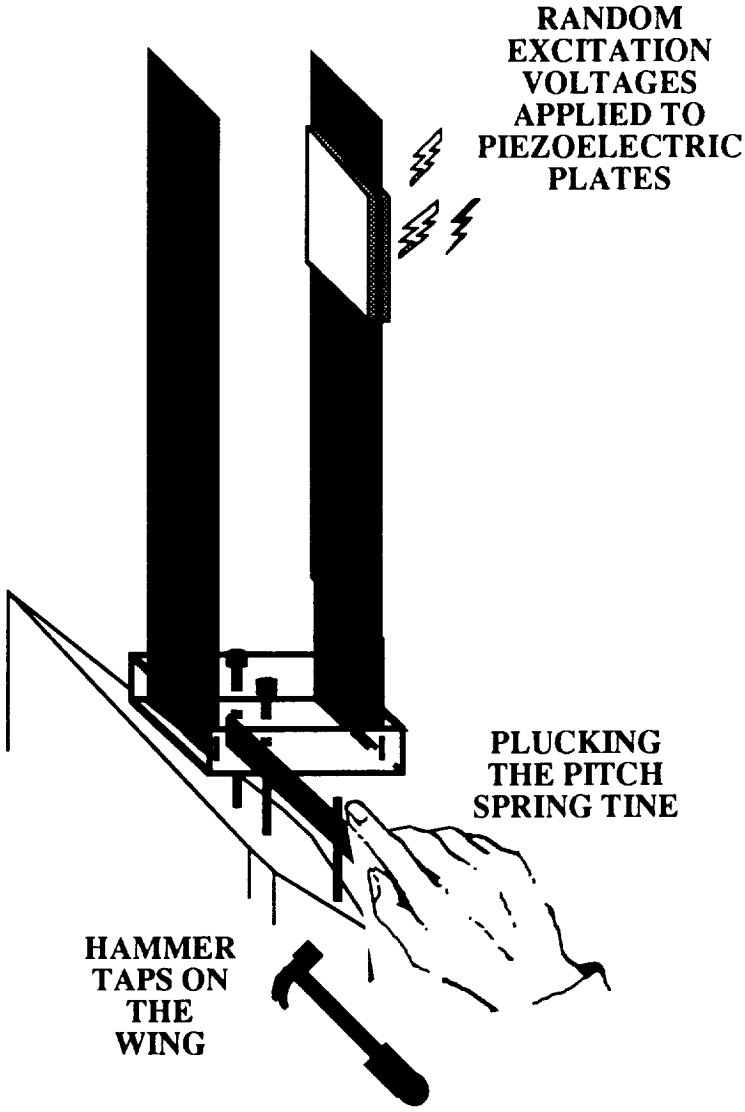

Figure 6.1 Experimental Sytstem Identification Techniques

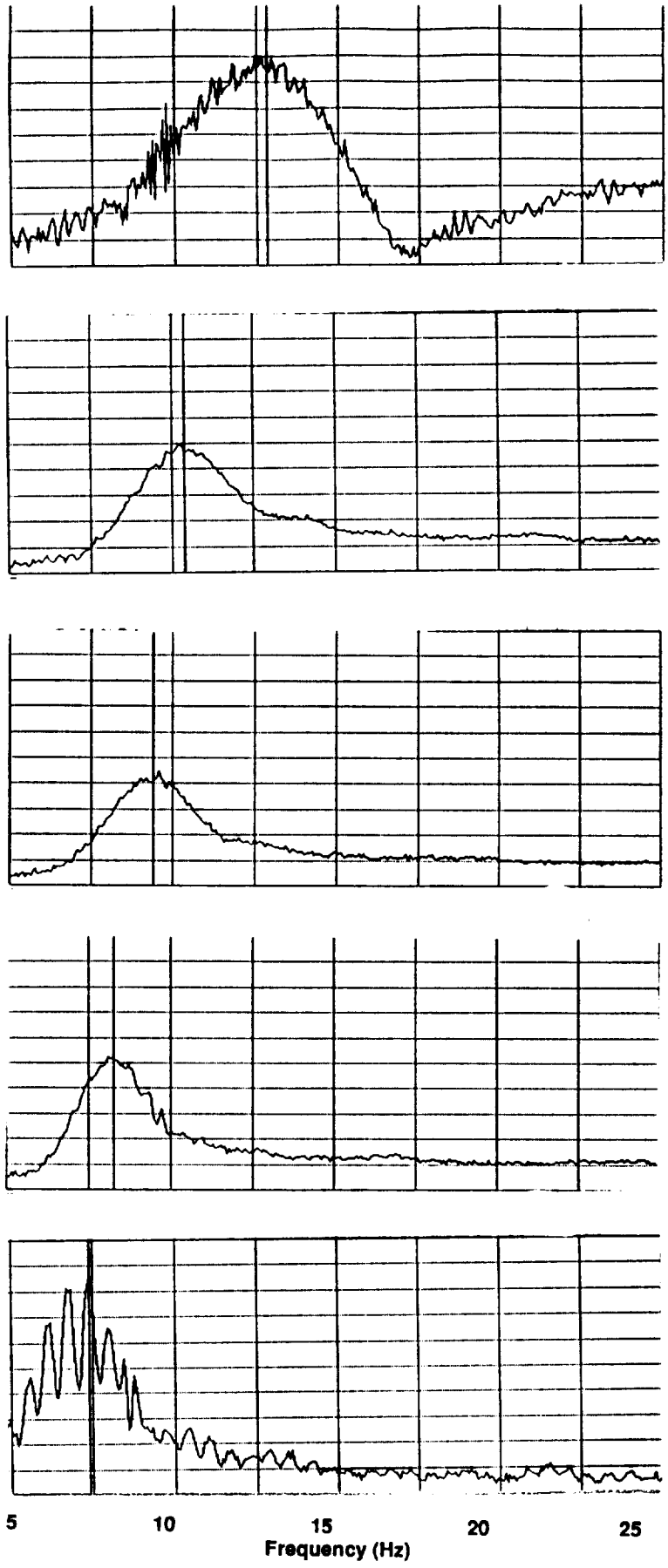

Only Balsa Wood Wing Extension

12.8 Hz

.005 lbm Ballast

10.4 Hz

.007 lbm Ballast

9.4 Hz

.011 lbm Ballast

8.25 Hz

.017 lbm Ballast

7.4 Hz

Figure 6.2 Frequency Response of Acceleration due to Hammer Taps Applied to the Open Loop System for Various Mass Ballasts

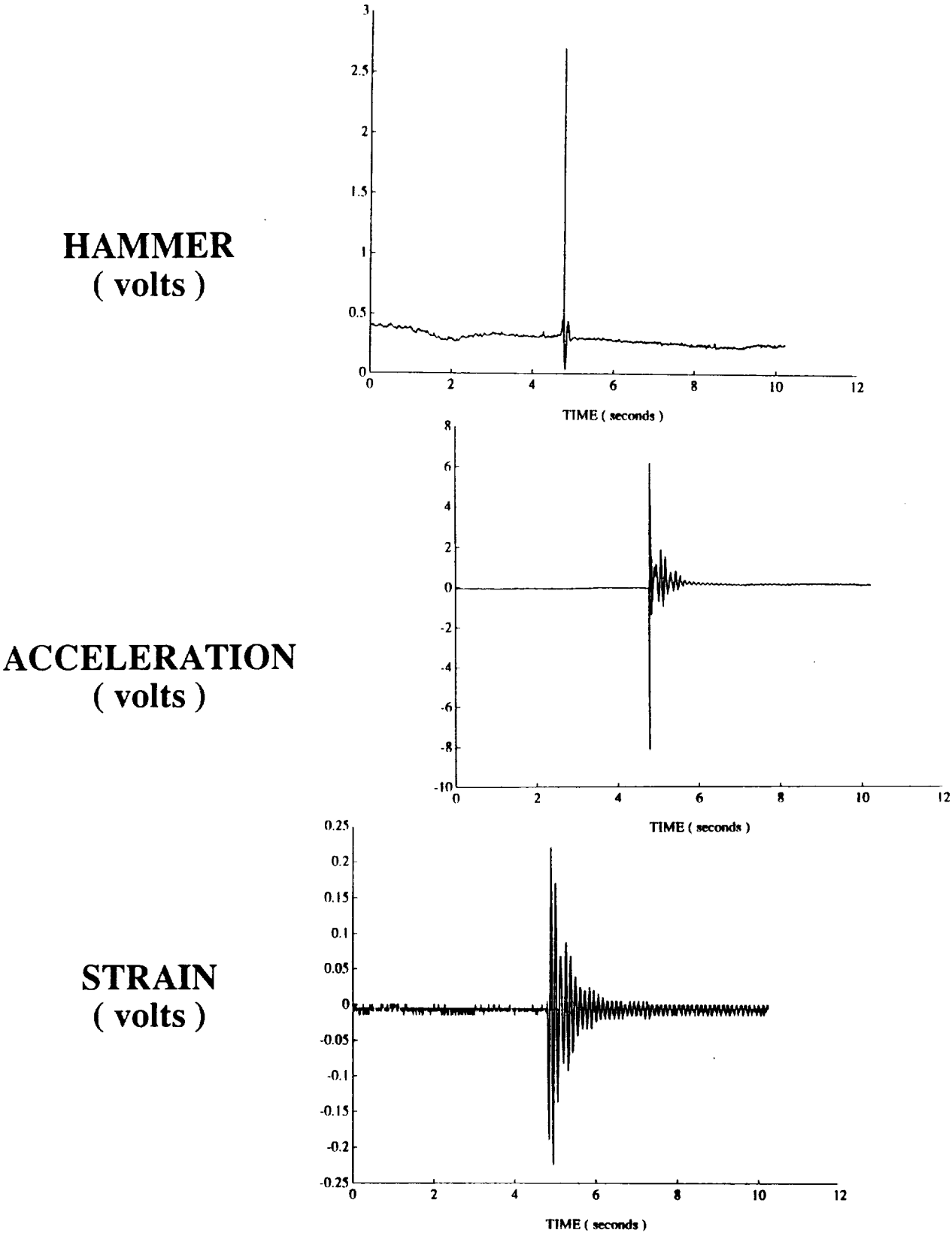

Figure 6.3 Time Histories from Hammer Tap System Identification Test

a) Hammer Input
b) Acceleration Response
c) Strain Response

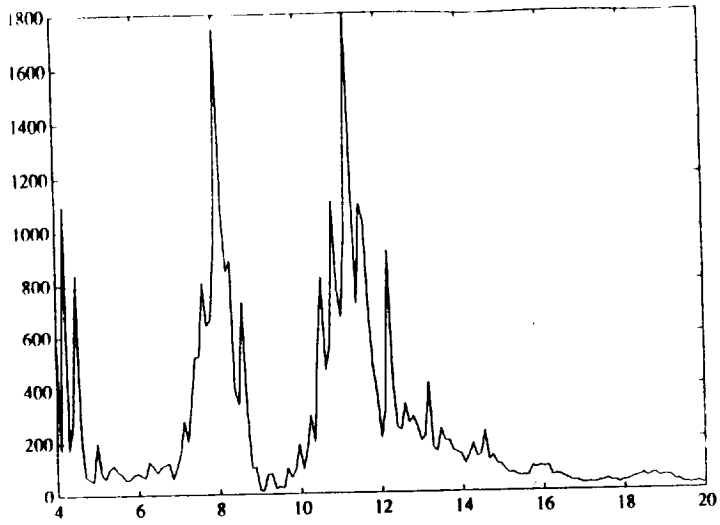

a) PSD of Acceleration due to Hammer

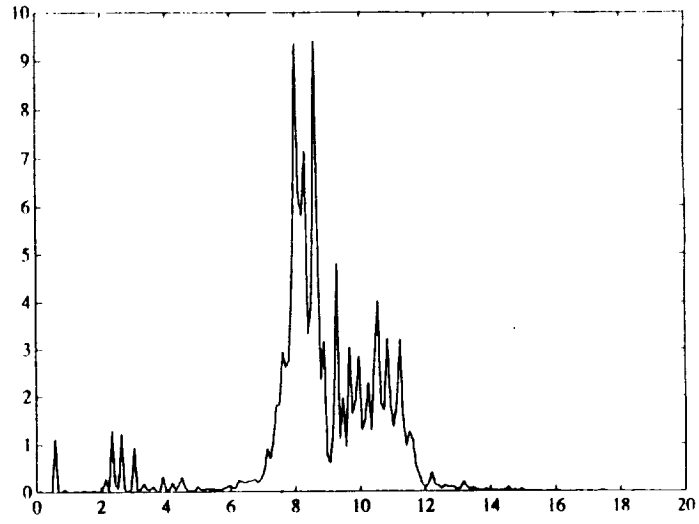

c) PSD of Strain due to Hammer

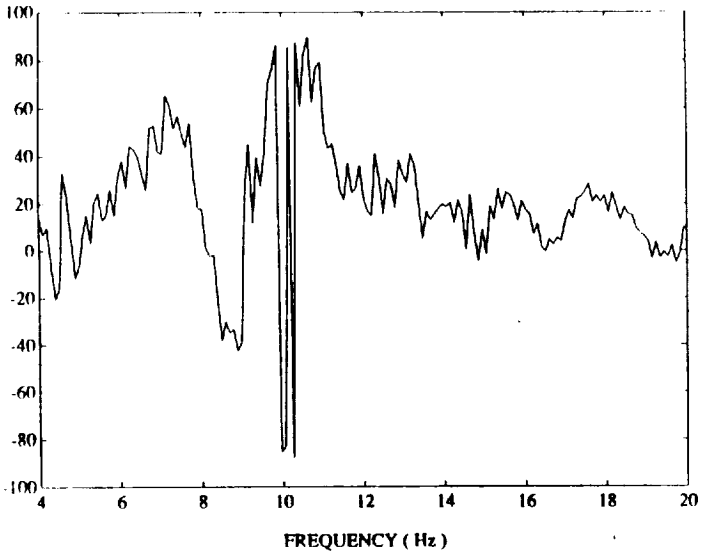

b) Phase of Acceleration due to Hammer

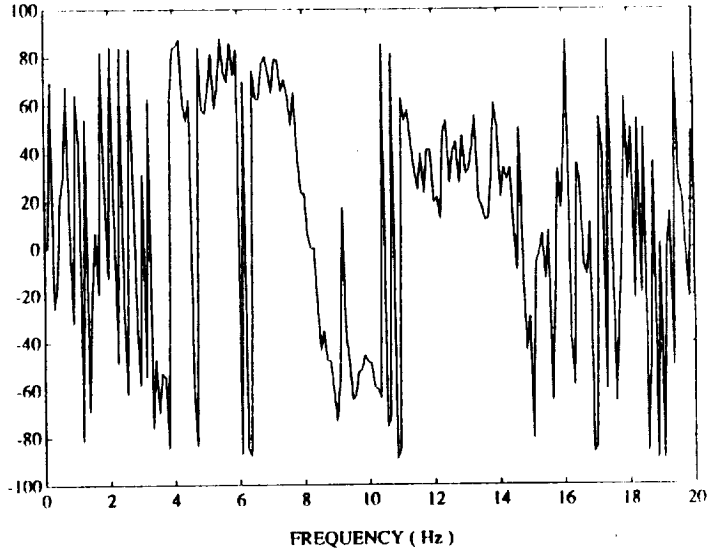

d) Phase of Strain due to Hammer

Figure 6.4 Frequency Domain Analysis of Hammer Test Transfer Functions

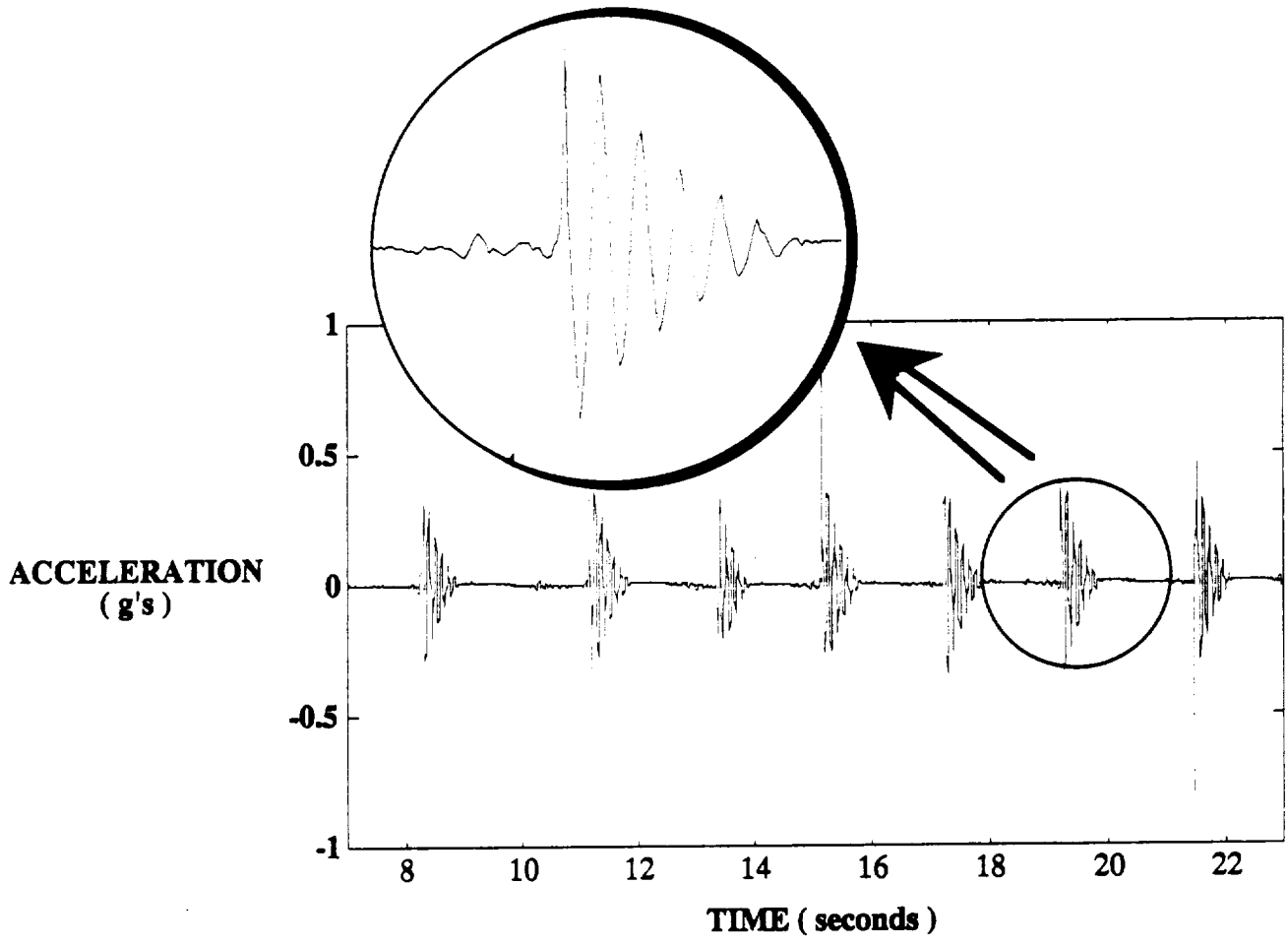

Figure 6.5 Time History of Acceleration Response to Plucks at Zero Airspeed

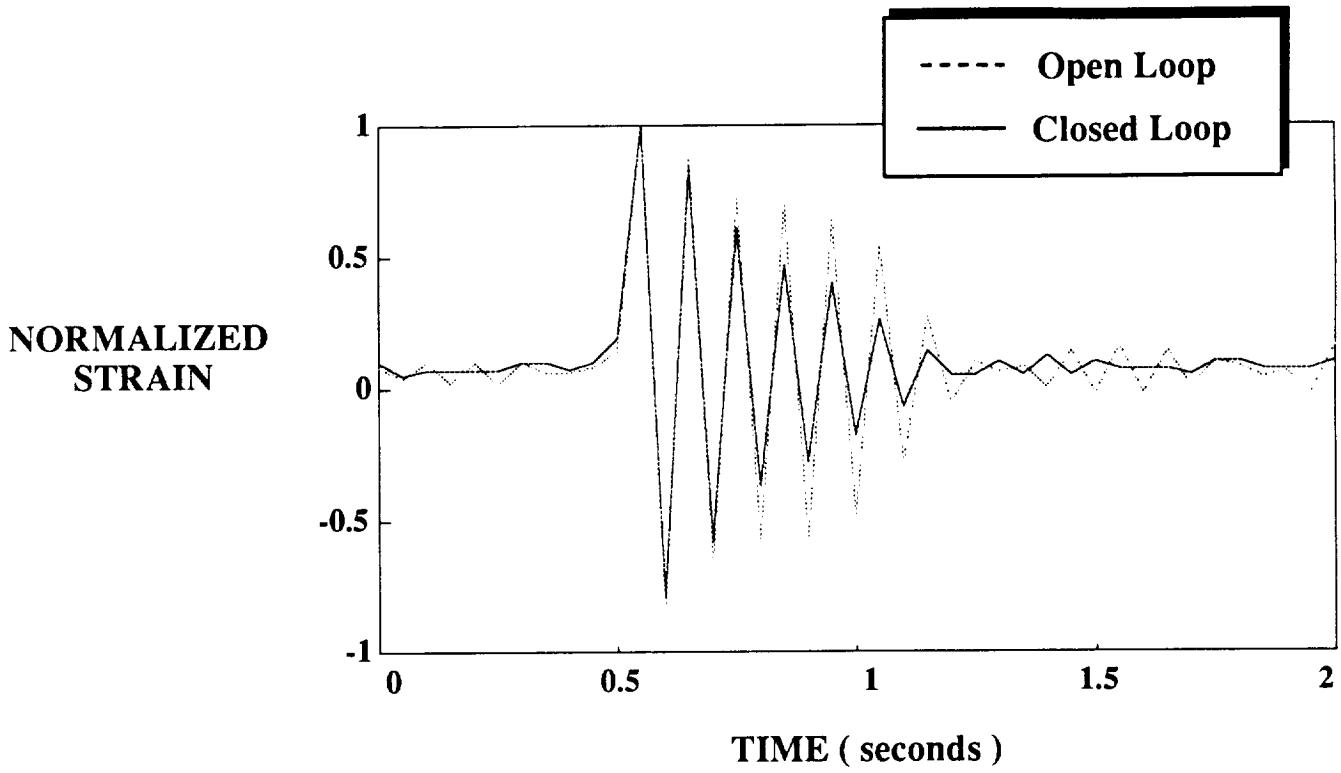

Figure 6.6 Open and Closed Loop Strain Response to Pluck Test at Zero Airspeed

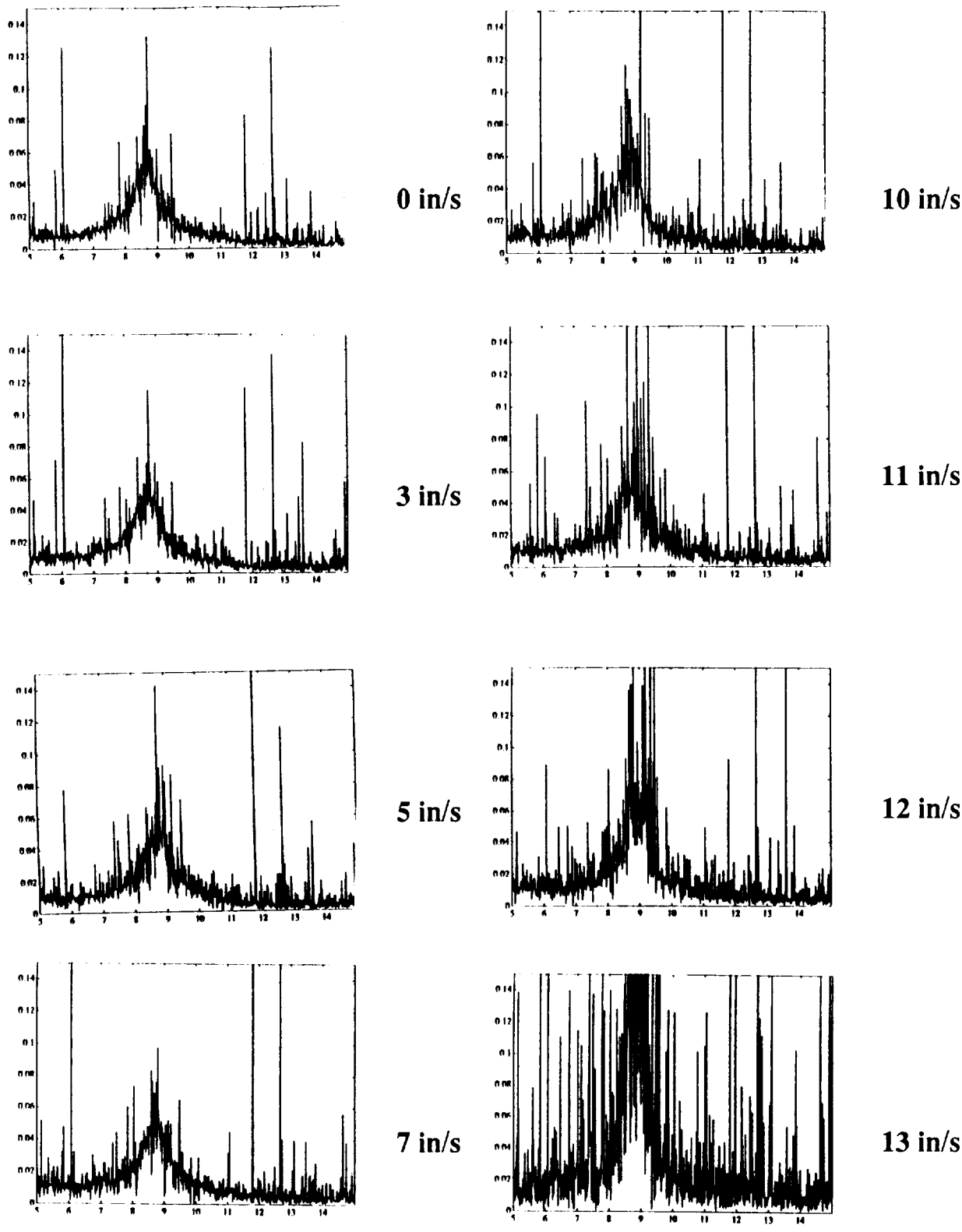

Figure 6.7 Open Loop Strain Magnitude due to Random Excitations Applied through the Piezoelectric Actuators at Various Airspeeds

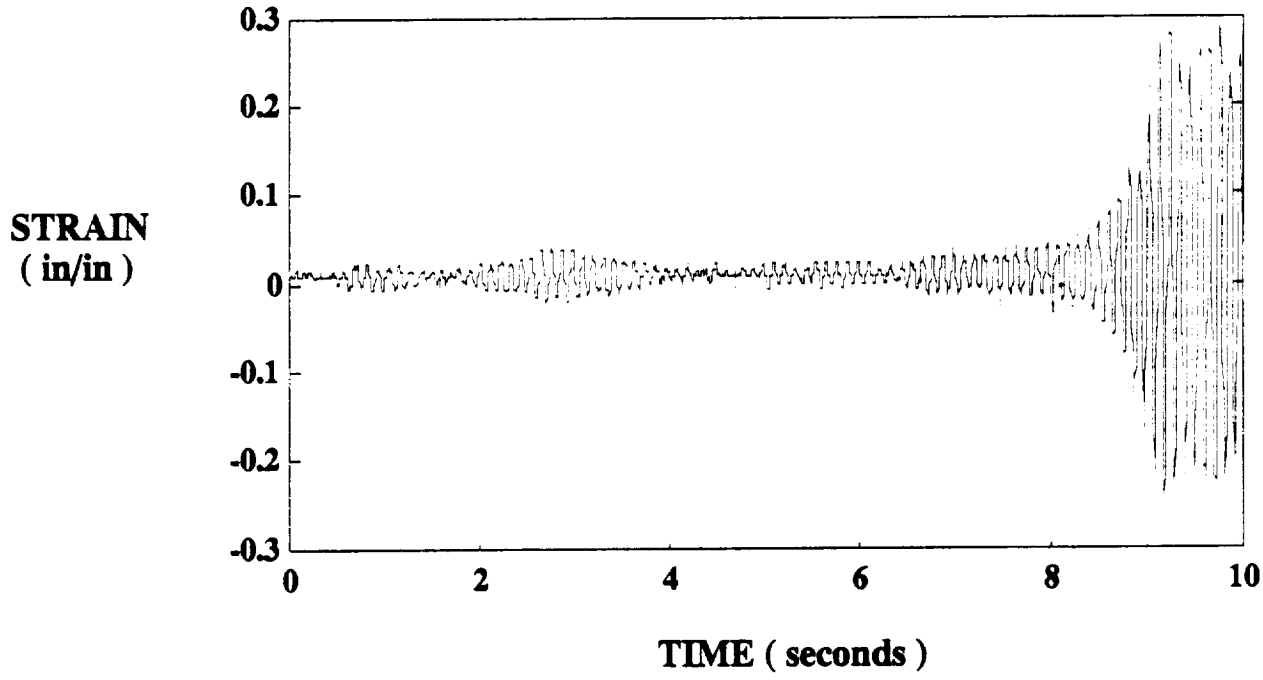

Figure 6.8 Open Loop Flutter Point, 580 inches per second

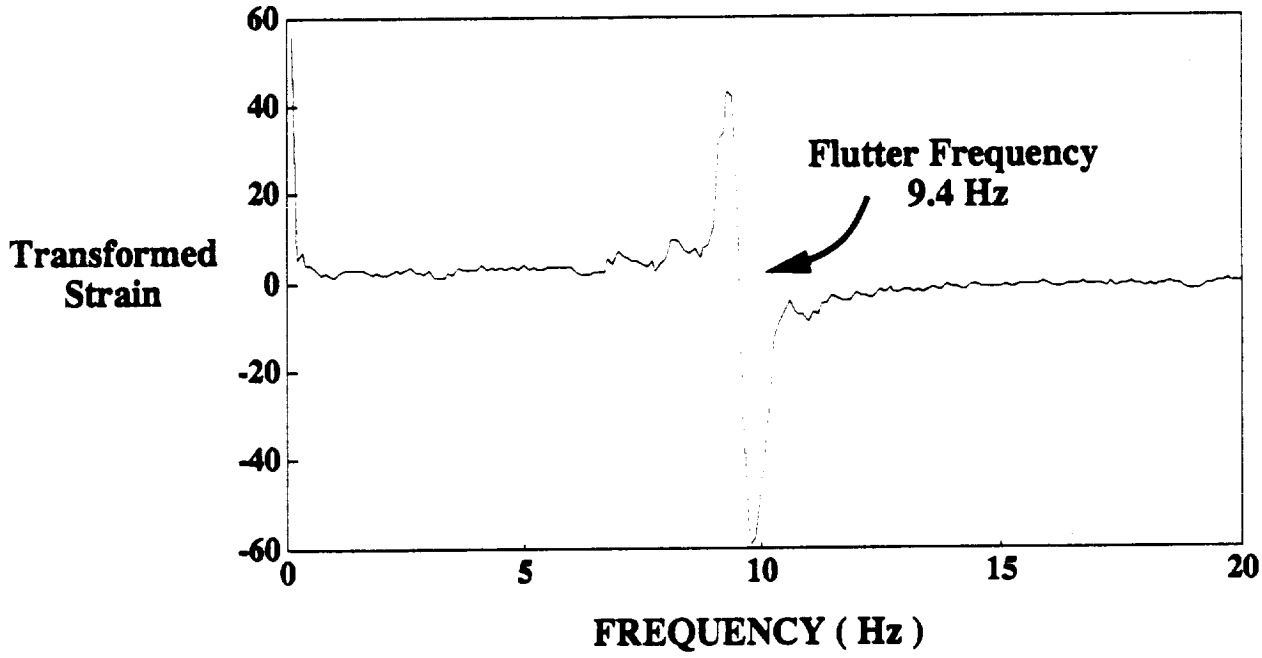

Figure 6.9 Frequency Domain Analysis at Open Loop Flutter Point, 580 inches per second

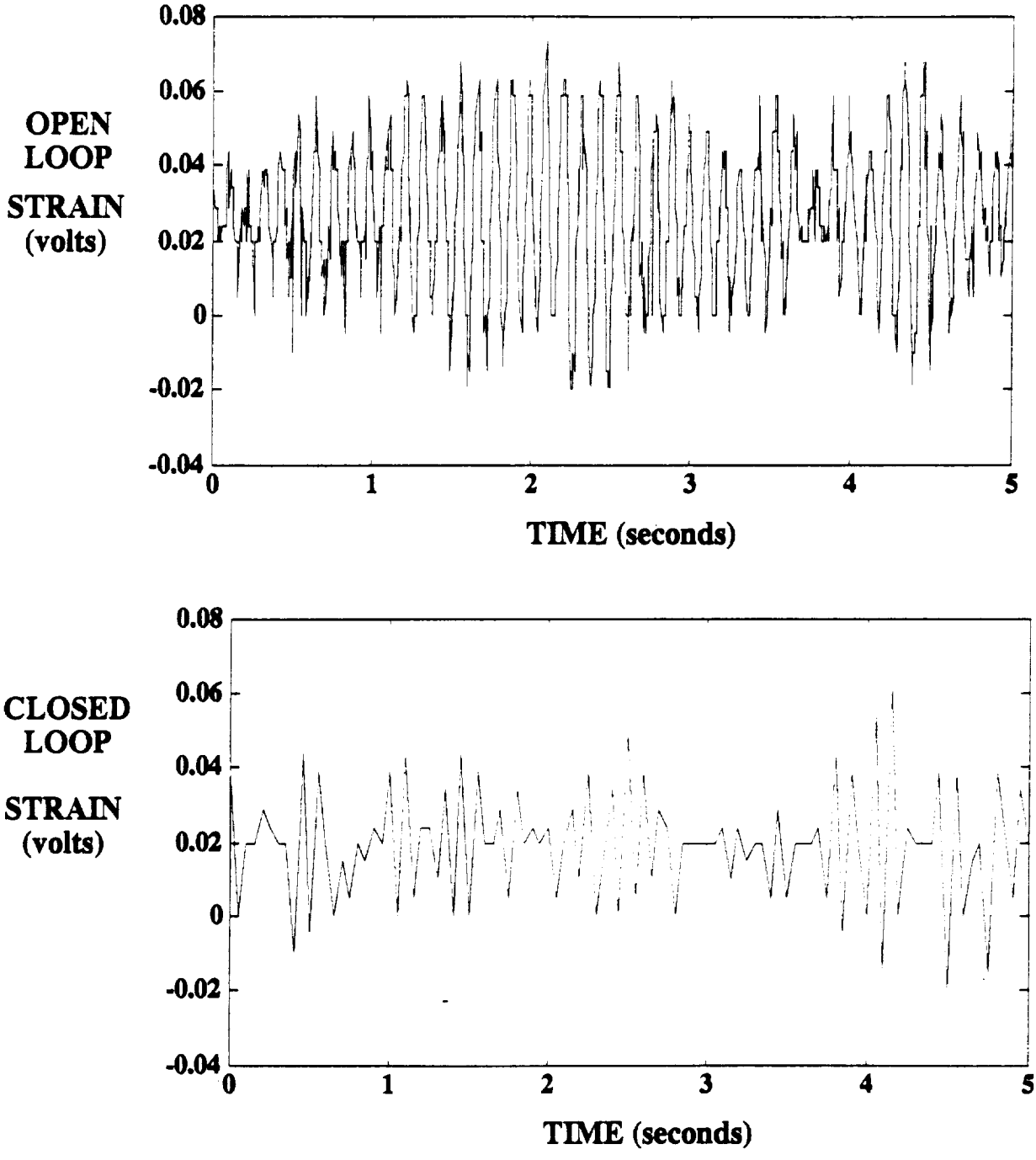

Figure 6.10 Experimental Open and Closed Loop Strain Response to Wind Tunnel Turbulence Just Below Flutter Velocity (575 inches per second)

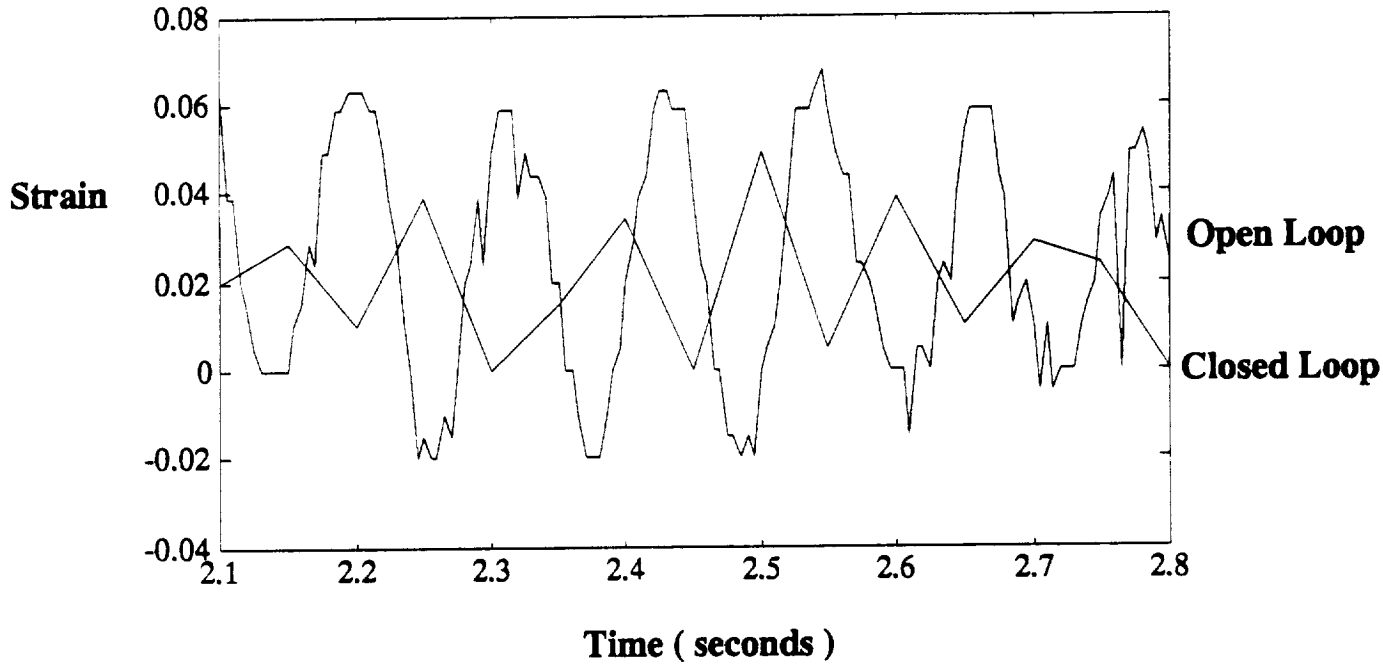

Figure 6.11 Experimental Open Loop and Closed Loop Strain Response Just Below Open Loop Flutter (575 inches per second)

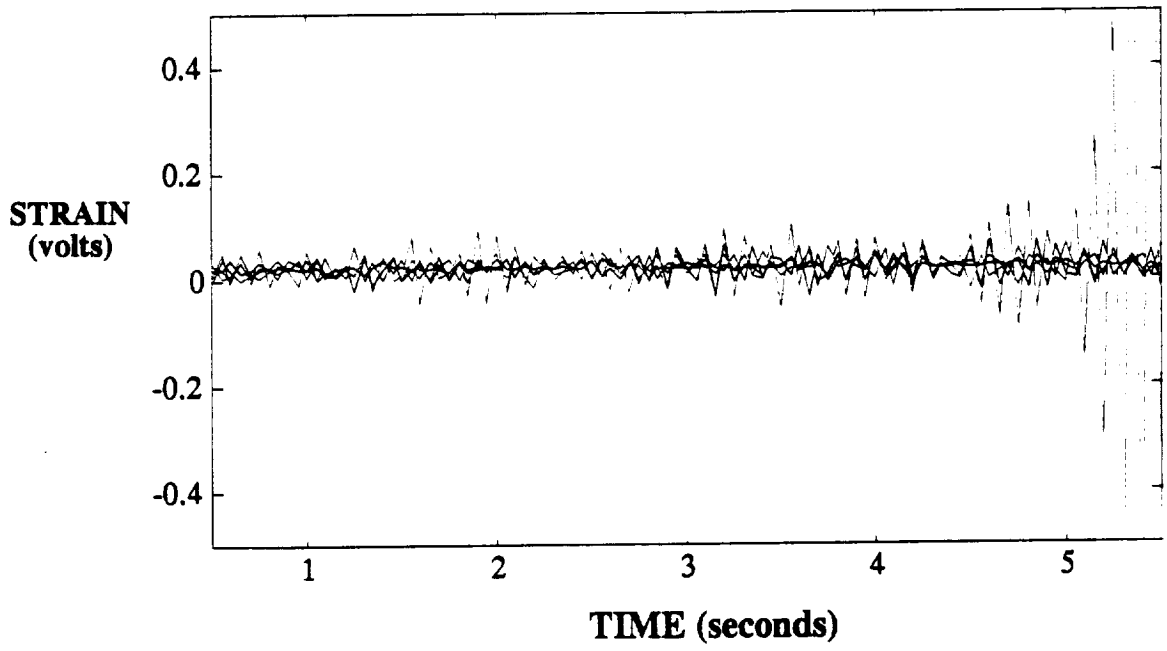

Figure 6.12 Experimental Time Histories of Closed Loop System for Increasing Velocities

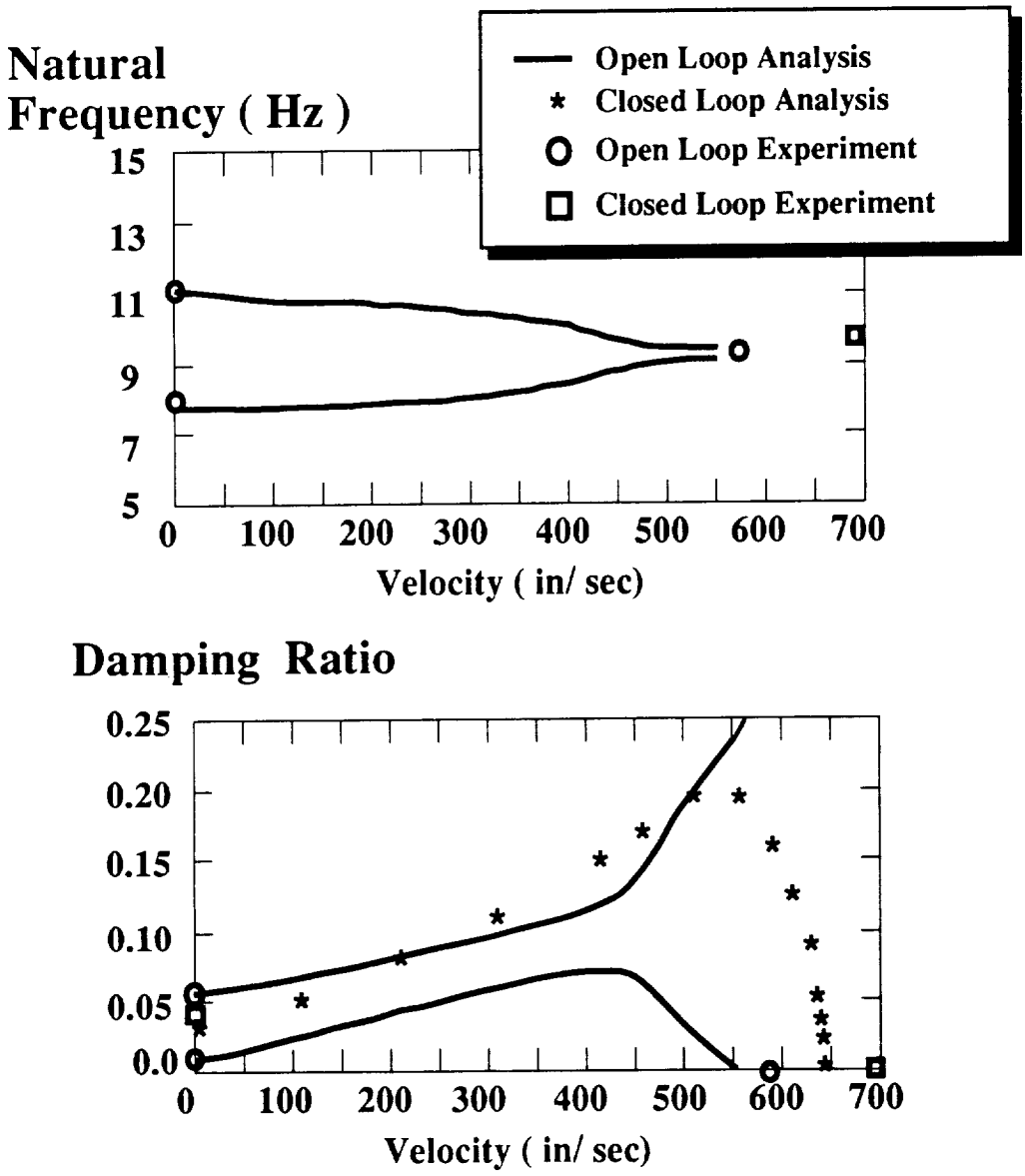

Figure 6.13 Analytical and Experimental Flutter Results